An Optical Study of Nanofluidics in Mesoporous Silicon

Vom Promotionsausschuss der
Technischen Universität Hamburg

zur Erlangung des akademischen Grades

Doktor der Naturwissenschaften (Dr. rer. nat.)

genehmigte Dissertation (Monografie)

von

Guido Dittrich

aus

Hamburg

2025

Gutachter:
Prof. Dr. rer. nat. Patrick Huber
Prof. Dr. rer. nat. Alexander Petrov

Tag der mündlichen Prüfung: 22.05.2025

Diese Arbeit widme ich dir, meiner wundervollen Frau Nasia. Du lässt mich stets nach dem Höchsten streben, hast mich in allem unterstützt und mir beigestanden. Ich bin unendlich dankbar, dich an meiner Seite zu haben.

ORCID: https://orcid.org/0000-0003-1003-7299
DOI: https://doi.org/10.15480/882.16131

Abstract

This thesis introduces an advanced method for investigating capillary imbibition and vapor sorption phenomena in mesoporous silicon (PSi). Central to this method is a PSi chip-like reflective sensor (CLRS) paired with a white-light spectrometer. The integration of in-situ thin film with 1-D photonic crystal reflection spectroscopy achieves high precision in monitoring both overall and local filling dynamics. This interferometric technique provides sub-nanometer precision with time resolution down to microseconds. The anisotropic pore array of PSi is optically evaluated for porosity and thickness using *Fourier* analysis of reflection spectra and the *Maxwell Garnett* effective medium approximation. Results show excellent agreement with scanning electron microscopy, gravimetry, and nitrogen sorption isotherms.

For capillary imbibition at the given pore size of approximately 7 nm, local undulations become significant, alongside the molecular dimensions of the infiltrating liquid. A *constriction model* incorporating an immobile layer at the pore wall consistently describes the dynamics of liquid transport. The combination of local and global dynamics allows fluid front shape reconstruction, resolving precursor films of polymeric melts. During vapor sorption, drying, and water imbibition experiments, the CLRS surface is beforehand chemically oxidized, and an optical microcavity is positioned at various distances from the free surface. Desorption and drying reveal a percolation mechanism that empties the pores indicating interconnections between them. The latter seems less influential in capillary flow.

Additionally, a rapid and non-destructive technique for examining the pore trace of PSi membranes is introduced. This involves imbibing with a volatile liquid from both pore extremities and measuring dynamics via thin film spectroscopy. The analytical solution of the *inverse problem of capillary filling*, concerning filling fractions, yields the pore radius profile. It is generally applicable for methods measuring volume or volumetric filling fractions instead of imbibition front positions and is here applied for the first time to a mesoporous material in studying common PSi synthesis routes. Enhanced permeability is achieved through a post-synthesis treatment that dissolves constrictions.

Contents

1 Introduction

Porous materials present a wide range of design possibilities for tailored material properties. Notable attributes such as lightweight, thermal insulation, and strength are frequently encountered in daily life. However, as *Feynman* famously highlighted in his 1959 lecture, "there's plenty of room at the bottom."[1] The field of nanoporous materials has ascended alongside nanotechnology, providing exceptionally high specific surface areas, often in the realm of hundreds of m^2/g, effective macroscopic properties, and confinement effects. The substantial wall interaction of fluids, capillary action, and distinct optical properties at this scale constitute integral parts of the present thesis. The term *nanoporous* encompasses pore sizes from 1 to 100 nm but is frequently applied to dimensions exceeding several 100 nm as well. Conventionally, a more precise categorization defines *microporous* as $0.2 - 2$ nm, *mesoporous* as $2 - 50$ nm, and *macroporous* as $50 - 1000$ nm.[2] The primary focus of this work is on mesoporous silicon (PSi), synthesized through a top-down etching process starting from commercial silicon wafers. The resulting structure features anisotropic pores aligned with the etching direction.

Mesoporous silicon is highly versatile, yielding a vast spectrum of applications. Examples include biosensors[3], microfluidic devices with smartphone connectivity[3], and solar photovoltaics[4]. Recent research unveiled a unique electrochemo-mechanical behavior of PSi in aqueous electrolytes.[5, 6] When combined with polypyrolle within the pore spaces, the electrochemo-mechanical coupling becomes even more promising for applications like artificial muscles.[5, 7] Additionally, PSi exhibits substantial transparency across the visible to infrared spectrum, can be luminescent and is biodegradable.[8–11] A crucial factor in its versatility is its well-adjustable porosity, scaling largely linear to pore size and controllable through the applied current density.[11] The thickness of a layer with a given porosity is variable on a scale similar to pore size, demonstrated by applications like spectral barcodes for multitarget detection.[11]

Significant research has focused on liquid transport phenomena within nanopores in the rapidly developing field of *nanofluidics*.[12] This is critical for applications such as drug delivery systems[13], nanofluidic transistors[12], and the formation of nanotubes[14]. Directly observing liquid transport inside nanopores poses considerable technical challenges due to dimensions below the resolution limit of visible light. Luna et al. demonstrate a strategy for investigating polymer transport by freezing polymer melts after varying infiltration periods and evaluating penetration depth ex-situ using scanning electron microscopy and x-ray tomography.[15, 16]

Similar challenges of direct observation exist in rock and concrete sciences and oil recovery[17], prompting adaptation of indirect measurement techniques for dynamics in nanopores. Techniques like gravimetric capillary rise measurements[18], x-ray diffraction[19], and neutron imaging[20] are employed. Moreover, recent advances include sensitive deformation measurements during imbibition.[21] In transparent mesoporous monoliths, liquids become visible to the naked eye due to the change in effective refractive index contrast.[20–22] Additionally, the broadening of the liquid front can be observed as an advancing light scattering layer proceeding in front of the homogeneously filled region.[22]

A versatile approach used in this thesis for the investigation of fluid transport in mesoporous silicon involves interference spectroscopy on thin films ranging from 3 to 100 µm. PSi layers exhibiting an interference pattern within a specific spectral range will be referred to as *Fabry Pérot* layers.[23–25] The interference fringes shift with changes in effective optical thickness (EOT), when the fluid occupying the pore space is replaced by another with a varying refractive index. This principle has been employed in the study of sorption isotherms[26, 27] and liquid capillary rise[28].

In nature, related interference phenomena cause dynamic structural color changes. As found in *Tmesisternus Isabellae*, a longhorn beetle, structural color dynamically shifts with humidity, transitioning from green in dryness to red upon saturation. This color originates from a 1-D photonic crystal structure of nanometer-layered material within the scales, composed of an alternating stack of melanoprotein and porous layers filled with air.[29, 30] Saturation induces swelling, altering layer spacing and effectively changing the refractive index by replacing air with water, cumulatively enhancing the optical path length within the material. This thesis extends such structured design to PSi. A 1-D photonic crystal microcavity, at a compact thickness of $\sim 3\,\mu m$ when designed for visible spectrum use, is utilized to probe polymer imbibition.[31] For polymeric fluids, simulations of nanopores predict thin molecular film progression along pore walls ahead of the bulk liquid front.[32] This precursor film's dynamics can be resolved using techniques like x-ray scattering[19] and 1-D photonic crystal spectroscopy[31]. This thesis further develops the latter by combining interference and resonance measurements on *Fabry Pérot* layers with a microcavity.[33] This advancement allows simultaneous collection of overall and localized filling dynamics using a chip-like device. The first major study within this thesis investigates liquid dynamics of oligostyrenes with varying polymerization degrees, aiming to derive a cohesive fluid dynamics model. Recent simulations of such short-chain molecules suggest notably slow dynamics within nanopores, even under low confinement degrees.[34] In the second study of this thesis, it is built on the fluid dynamic model of the first one, while in the third the optofluidic device is optimized for water sorption experiments, testing the microcavity's sensing capability at differing heights across *Fabry Pérot* layers, and examining sorption mechanisms. Additionally, water imbibition with microsecond temporal resolution is demonstrated. The thesis follows the chronological progression of these studies as they built sequentially.

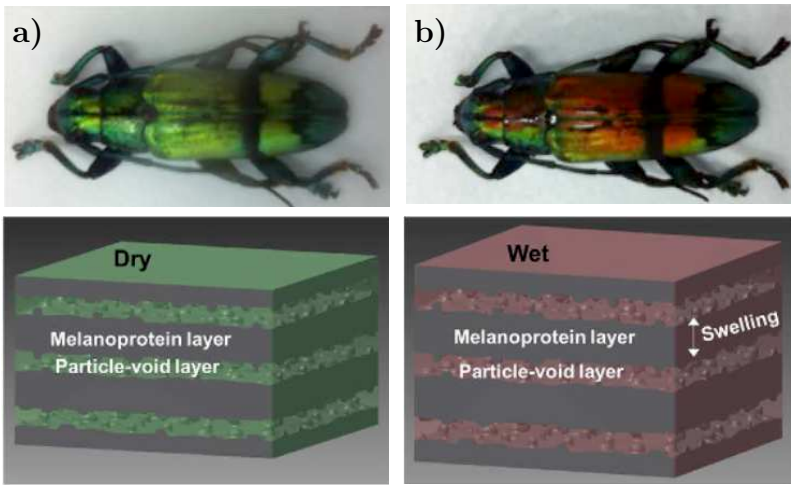

Figure 1.1: Longhorn beetle in dry (a) and wet state (b) alongside material illustration beneath. (Images of beetles by *Seo et al.* are under a Creative Commons license [30], and material illustration is licensed for Open Access by *Optica Publishing Group* [29].)

Capillary rise in a uniform diameter tube under laminar flow conditions is classically described by the *Lucas-Washburn* equation.[35] This equation's proportional relation of imbibition length to the square root of time holds in numerous porous media contexts, evident in independent pore arrays where each follows this behavior individually. More intricate porous structures often exhibit similar square root of time dynamics, albeit requiring an adjusted proportionality constant. A comprehensive model framework for liquid transport in porous media is provided by *Darcy*.[36] Essentially, bulk transport of a *Newtonian* fluid is defined by scaffold geometry, driving pressure, and flow rate. On the nanoscale, however, factors such as wall interaction and confinement significantly influence transport.[12, 37] Setting aside these nanoscale interactions, capillary transport in a tube remains a classical engineering inquiry into flow dynamics, defined by pore size and capillary pressure implications. Pore size variability may exist axially, prompting directional imbibition dynamics.[38] Such variation introduces the *inverse problem of capillary filling*, questioning pore size variation from known capillary pressure and transport dynamics.[39, 40] Measuring axial pore size gradients in mesoporous materials presents challenges due to required resolution, at the nanometer scale, while gradients become significant at micrometer length of the pores. PSi, notable for diverse synthesis routes[10, 11, 41], requires advanced techniques for such measurements. Techniques like scanning or transmission electron microscopy face limitations here. Advanced efforts using high-resolution x-ray diffraction[42] and elastic guided waves[43] provide partial insights at considerable effort. This thesis's second study employs destruction-free capillary infiltration experiments to resolve PSi pore structures, solving the *inverse problem of capillary filling*.

2 Fundamentals

2.1 Mesoporous Silicon

The starting material for synthesis of mesoprous silicon are commercial monocrystalline silicon wafers. Silicon exhibits a diamond crystal structure, characterized by a face-centered cubic lattice with a di-atomic basis positioned at (0,0,0) and $(\frac{1}{4},\frac{1}{4},\frac{1}{4})$ with respect to the lattice constant $a = 0.543\,\text{nm}$ (Fig. 2.1).[44] Each silicon atom has a covalent bond to four neighboring ones in a tetrahedral configuration. This results in a stiff material, with an elastic modulus between 130 and 188 GPa depending on the crystallographic direction.[45] Its bulk modulus is 97.8 GPa.[45] The mechanical properties are not further analyzed here, as the deformations encountered in this study are minimal.

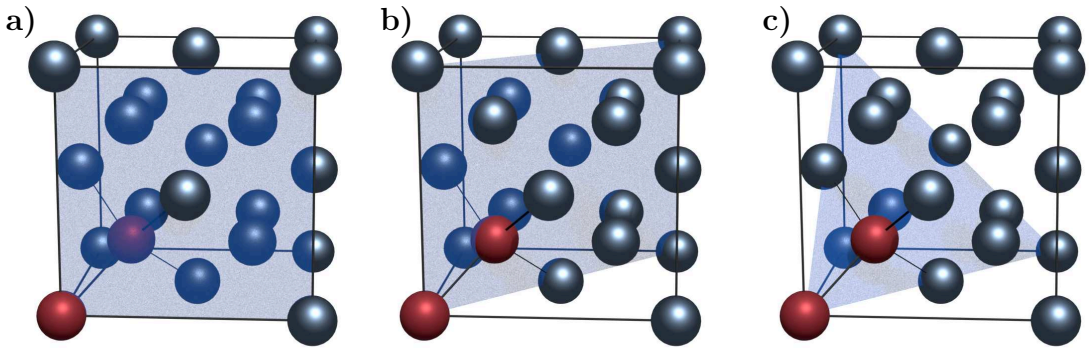

Figure 2.1: Diamond crystal structure of silicon. The two atomic base is highlighted in red. The crystallographic planes with *Miller* indices (100), (110) and (111) are shaded blue in panels a), b) and c), respectively. Each atom in this structure has four equivalent next neighbors, due to the covalent bond with sp^3 hybridization. This is depicted by connections emanating from the inner red atom.[46, 47]

In its pure form, silicon is a semiconductor with an indirect band gap, as apparent from the band structure in Fig. 2.2 a), which shows the allowed energies for electrons. This band structure is a result of the overlap of molecular orbitals and the periodic potential by the regularly arranged atomic trunks of the crystal. The link between structure and allowed energies is specified best by means of the reciprocal

lattice. Fig. 2.2 b) displays the first *Brillouin* zone. At its borders, indicated by characteristic points, electron waves are stationary due to *Bragg* reflection and the allowed electron states are split into different bands repelling each other. As a result an energy gap E_g emerges, separating occupied and unoccupied states, i.e. valence and conduction band at 0 K. The highest energy level at this temperature is defined as the *Fermi* energy E_F. Conducting electric currents necessitates accessible energy states. Since the valence band is completely filled and separated by the band gap, silicon acts as an insulator at absolute zero. Nevertheless, thermal excitation or light exposure can supply the energy needed to overcome the E_g of 1.17 eV, promoting electron transition into the conduction band.[48] The band gap is termed indirect because the valence band maximum resides at the Γ-point while the conduction band minimum is near the X-point. At higher energy contributions, such as through light excitation, the near-parallel alignment of the lowest occupied and unoccupied bands presents additional states for electron transitions, which correlates with increased absorption.[48] Electrons transitioning from the valence to the conduction band encounter unoccupied nearby energy states, facilitating conductivity. At the same time the free energy state left behind in the valence band contributes to the mobility of charge carriers in that band. Thus it is termed an electron hole. Hole and electron are attracted to each other and form an electron-hole pair, but they can be separated by application of an external electric field. Despite this, the density of mobile charge carriers remains low compared to metals at room temperature.
The conductivity of silicon can be tuned by substitution with elements differing from its own valence of four, which is called doping. Introducing an element with a valence greater than silicon's, such as phosphorus that seeks five covalent bonds, results in n-doping. This adds extra unbound electrons, creating additional energy states near the conduction band for excitation. In this work, only p-doped wafers are utilized, achieved through boron atoms having a lower valence of three. Boron provides hole states close to the valence band. Conductivity then hinges on the doping level, which relates to the number of additional foreign atoms.[45, 47–49]

In this thesis, only wafers sliced along the (100) crystal plane are employed. These wafers are polished on one side, which acts as the active surface during the etching process, while the opposite side remains rough due to the sawing from a silicon ingot. An electrical contact is established at this backside using tightly clamped aluminum foil. Silicon can be dissolved in alkaline environments, however, the etching method applied here requires a reactive agent for controlled dissolution. Hydrofluoric acid (HF) offers an acidic environment that retains silicon but can also dissolve it when bonds are weakened through stretching, hole conduction, or chemical reactions. Due to its strong reactivity and high diffusivity, HF is contained within a poly-tetra-fluor-ethylene (PTFE) batch reactor. Fig. 2.3 illustrates the cross-section of a typical etching cell. Given the vapor pressure of the later introduced reaction solution the cell should be closed by a lid, which has to allow the release of pressure, since hydrogen gas is produced during some chemical reactions.

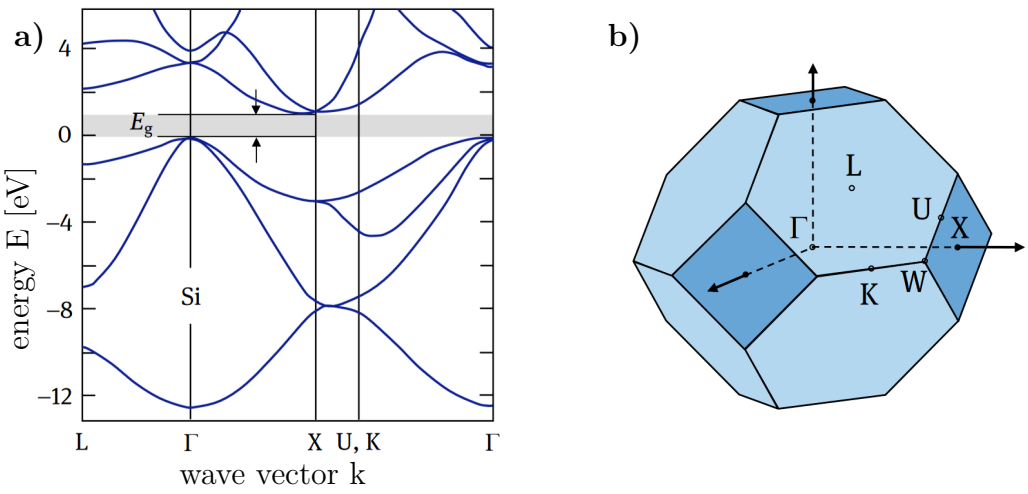

Figure 2.2: a) bandstructure of silicon b) 1. *Brillouin* zone of its structure.(Creative Commons license CC-BY 4.0)[46]

A large platinum plate serves as counter electrode, which is perforated to reduce the accumulation of bubbles.[11]

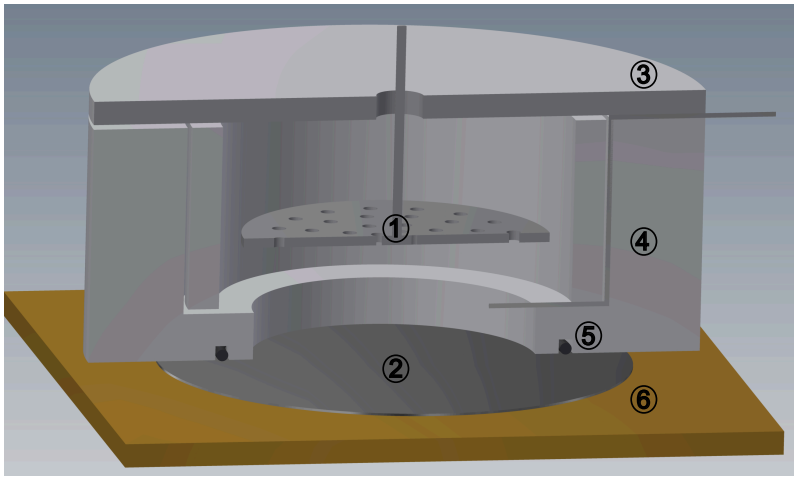

Figure 2.3: Electrochemical cell for the synthesis of mesoporous silicon. (1) platinum counter electrode, (2) silicon wafer, (3) PTFE top, (4) PTFE reactor wall, (5) sealing ring, (6) copper plate. (illustration by Julian Häntsch)[50]

The mechanism for mesoporous silicon formation encompasses its chemical reactions, conductivity, and structure. These aspects are examined here for p-doped silicon in HF solutions. The reaction solution for synthesis comprises HF as the reactive agent, water as both solvent and side reactant, and ethanol to lower surface tension. Under ambient conditions, silicon naturally develops a thin oxide layer. This silicon dioxide is directly susceptible to aqueous HF, allowing the native oxide

layer to be stripped upon contact with the reaction solution. The exact mechanism of the reaction is still under discussion, but Eq. 2.1 gives an adequate description of the process. The presence of water enables the dissociation of HF into the dimer $(HF)_2$ and bifluoride HF_2^-, which are the reactive species. Near surfaces, F^--ions are also present, but they are considered to be inactive. Once the oxide layer dissolves, the surface of the wafer becomes terminated with hydrogen.[9, 11]

$$SiO_2 + 6HF \longrightarrow SiF_6^{2-} + 2H^+ + 2H_2O \tag{2.1}$$

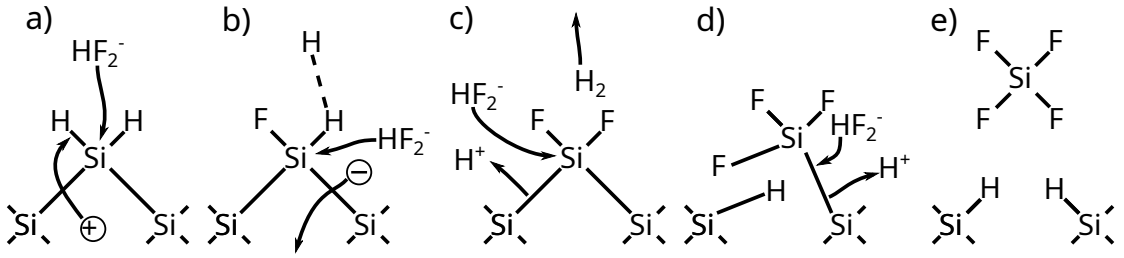

Figure 2.4: Divalent dissolution of silicon, leading to the formation of mesopores.(licensed reuse)[10]

The hydrogen-terminated surface of silicon exhibits substantial inertness when immersed in HF solution, attributed to the uniform electron density distribution at the hydrogenated silicon atoms. Termination by more electronegative species, such as fluorine or oxygen, induces polarization in the silicon atoms, weakening the Si-Si back bonds and making the polarized silicon susceptible to nucleophilic attack. Therefore, these surface species, along with the attached silicon atom, are swiftly removed upon formation. While fluorine and oxide substitutions facilitate silicon dissolution, hydrogen termination ensures stability.
For the formation of anisotropic pores in the etching direction bifluorides (HF_2^-) are the important species. Their nucleophilic attack is enabled through an anodic potential delivering valence band holes to the electroactive surface (Fig. 2.4 a). This hole supply determines the rate of the dissolution process. Once a $Si-F$ bond has substituted a hydrogen termination, a second nucleophilic attack by a bifluoride occurs much faster (Fig. 2.4 b). This reaction entails electron injection. The displaced hydrogen atoms combine to form hydrogen gas, released alongside HF species from the bifluorides. As previously mentioned, the fluorine substitutions enable further nucleophilic attacks by bifluorides on the silicon surface atom's backside (Fig. 2.4 c). A third fluorine atom is attached breaking a $Si-Si$ bond and leaving behind a hydrogen termination at the silicon atom attached to the bulk material (Fig. 2.4 d). The fourth nucleophilic attack leads to the release of silicon tetrafluoride into the solution, while again leaving a hydrogen atom at the new silicon surface behind (Fig. 2.4 e). The tetrafluoride rapidly reacts to

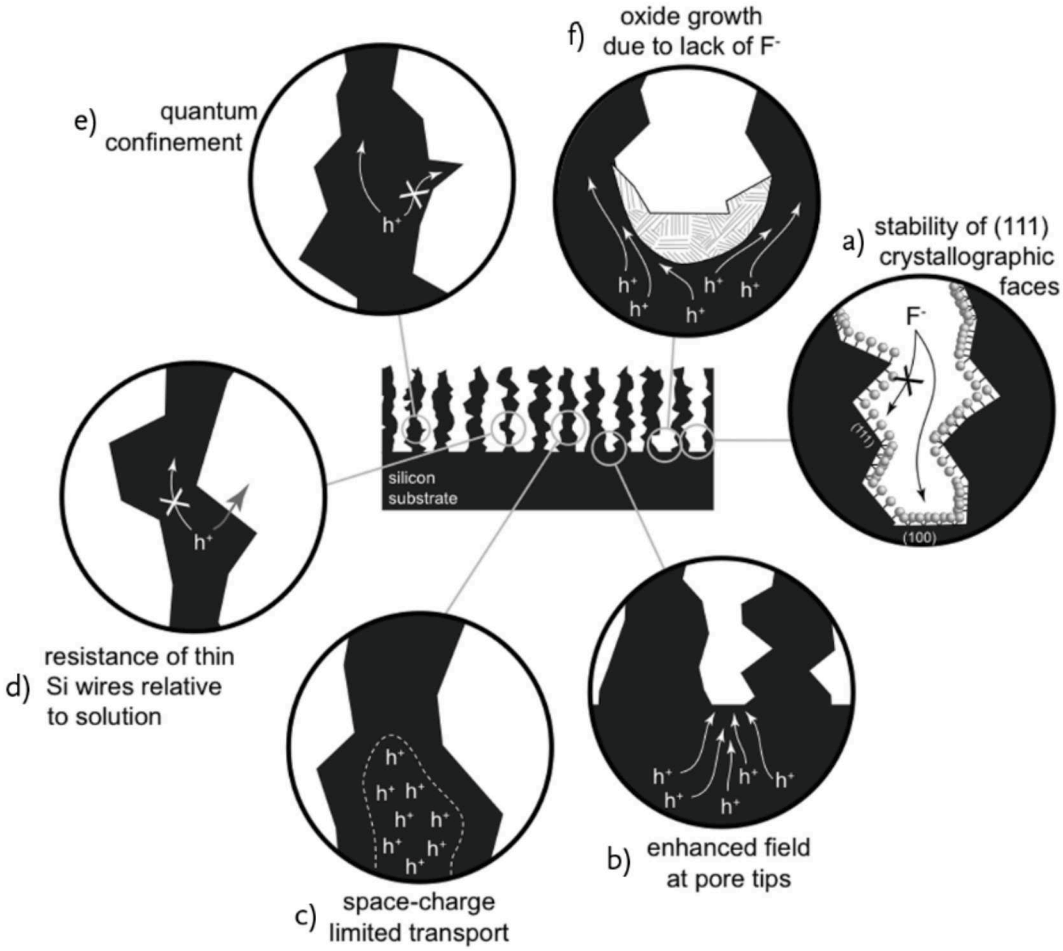

Figure 2.5: Mechanisms effecting porous silicon formation.(licensed reuse)[11]

siliconhexafluoride anions, which is soluble in the solution.This mechanism involves the transfer of two electric charges and is thus referred to as divalent dissolution.[10, 11]

Thus far, this explanation pertains solely to dissolution in the (100) crystal plane, leaving the mechanism of anisotropic pore formation unresolved. Under anodic potential application, etching initiates at minor surface defect sites on the silicon. This onset is largely random or remains inadequately understood. Once initial cavities emerge, the electric field intensifies at these tips (Fig. 2.5 b), attracting valence band holes and establishing a preferential dissolution direction. Pore walls, thinning to mere nanometers, render it more favorable and probable for holes to be transported to the solution (Fig. 2.5 d) rather than traversing longer paths. For diminutive pore walls and extremities e.g. dendritic extensions, quantum confinement induces a band gap increase (Fig. 2.5 e). Even though the material is highly doped, charge carriers have to overcome an additional energy barrier.[8] Another limiting factor for hole conduction within pore walls is the space charge region (Fig. 2.5 c), briefly formed upon electrolyte contact. For heavily p-doped silicon, as discussed throughout this

thesis, it is minimal.
Overall, pore surface crystal terraces primarily exhibit the (111) crystallographic plane. Etching at (111) surfaces occurs solely at kink sites (Fig. 2.5 a).[51] This creates a preference for attack sites when valence band holes become limited.[9–11, 52]
Selective dissolution is optimally controlled by current density, which is typically defined as the current applied over the wafer area susceptible to etching. Once etching commences, identifying the precise electro-active surface proves challenging due to the aforementioned changes in local conductivity. Hence, the projected area serves as the standard. Within a specific range, average pore size and porosity may be linearly manipulated by the applied current density. This control allows for the production of layered structures with varying porosity, a crucial design aspect for material property optimization. The limit for the smallest thickness of these layers is their average pore size.[11]

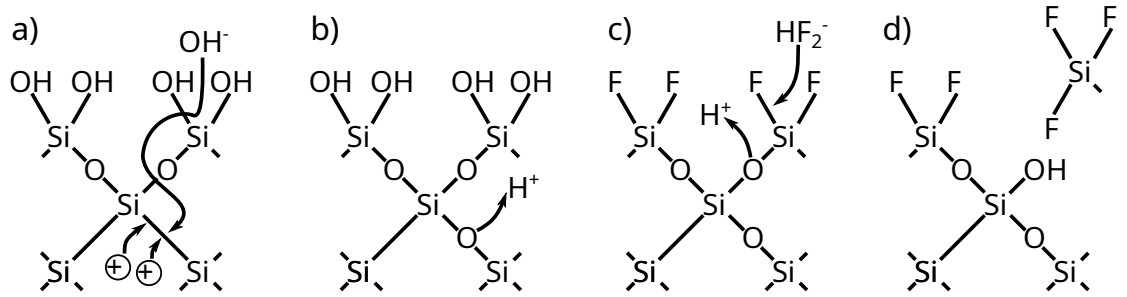

Figure 2.6: Tetravalent dissolution of silicon, used for electro-polishing and membrane detachment.(licensed reuse)[10]

The reaction solution composed of aqueous HF and ethanol can undergo an alternative reaction mechanism when specific conditions are met. At low concentrations of dissociated HF species within the reaction zone, particularly at the pore tips, this mechanism becomes significant. This can be either achieved by a generally low HF concentration or by an over-proportion of available valence band holes i.e. application of higher current densities. Then, the tetravalent dissolution takes over. Here, the first atomic silicon layer is already oxidized and terminated by OH-groups. The electric field, which is strongest at pore tips, attracts holes in the wafer and hydroxyl groups from the solution. These diffuse through the previously oxidized layer. Under exchange of two holes an $Si - Si$ bond is substituted by a $Si - O - Si$ bridge (Fig. 2.6 a), releasing a proton (Fig. 2.6 b). The oxidized layer prevents hole conduction in that region, which therefore are taking the next easiest path to the reaction solution, growing the oxide formation laterally (Fig. 2.5 f). In the meantime the HF concentration can recover by diffusive transport. Bifluorides can directly substitute the OH groups at the surface by fluorine (Fig. 2.6 c). Subsequently, the oxidized back bond is attacked. Under the formation of OH groups at the remaining oxidized silicon surface, a silicon tetrafluoride is released into the solution (Fig. 2.6 d), where it rapidly reacts to silicon hexafluoride anions. This non-selective process

effectively smoothens any uneven surfaces and is thus employed industrially for wafer polishing. Additionally, it is used to detach a porous layer from the bulk silicon wafer to create a freestanding membrane. This can be achieved with the previously used etching solution, albeit requiring high current densities that may exceed the capacity of some potentiostats. Alternatively, using a solution with a lower HF concentration and a small current density can result in a more uniform lift-off, although it carries a risk of incomplete membrane detachment.[9–11, 52] An unintentional tetravalent dissolution might occur during prolonged etching. Therefore, the HF concentration should be calculated carefully to remain within five percent of the initial concentration. Deviations can result in pore widening and eventual detachment of the porous layer. For homogeneous etching, the currents should be applied in pulses, with an application time depending on the current density used and a wait time at zero current. This prevents a diffusion limitation for HF species to the direct reaction zone.[11]

It is crucial to recognize that the described synthesis is highly dependent on the silicon raw material's characteristics. The synthesis demands a well distributed doping. For highly p-doped wafers it is often necessary to introduce a preliminary electropolishing step, because of a segregation of dopands close to the surface. If this region is not removed prior to the etching, a porous layer with smaller pore size is produced in the beginning.[11]

2.2 Optical Properties

The optical properties of materials can exhibit a wide range of behavior. The focus here is on maintaining constant and effective properties in thin films ranging from 100 nm up to 100 µm. Within this limited thickness, light is assumed to be coherent. For the purposes of this investigation, materials are examined at a wavelength region of low absorption, thus primarily considering the real part of the refractive index. The primary phenomena addressed in this context are reflection, refraction, and scattering. All measurements are conducted in normal incidence and reflection. The interference that follows from the wave character of light and the optical thickness (OT) of layers is on the one side manipulated by designed structures e.g. photonic crystals and on the other side analyzed to monitor physical properties.

In the simplest case the thin film interference of a free standing porous silicon membrane (Fig. 2.7) is considered. Such medium is often referred to as Fabry-Perót layer. An electromagentic wave in the visible to near infrared spectrum hits the thin film at normal incidence. At the air-membrane interface, a portion of the wave is directly reflected back to the source and detector, indicated by process (1). The intensity of this reflection is contingent upon the refractive index contrast ϱ (Eq. 2.2), where n_{air} is the refractive index of the initially transmitting medium, here air, and $n_{\mathrm{m+air}}$ the medium continuing after the interface, the membrane filled by air. The reflectance is $R = \varrho^2$. Only a minor portion is scattered because of surface

roughness and the rest is transmitted into the sample. This allows to approximate the transmitted intensity T by the expression $R+T=1$. In the membrane the inter-pore distance and pore size are much smaller than the wavelength of the incident light, therefore it behaves like a homogeneous layer from the point of view of the transmitted wave. This is the prerequisite for effective medium models that are introduced later. At the bottom the membrane is either again surrounded by air or by a fluid and reflection as well as transmission occur at the interface (3). The now reflected portion travels back to the initial interface where also transmission and reflection occur. The back into the membrane reflected portion is not treated further in this work. The transmitted portion interferes with directly reflected light at the upper interface. Depending on the the effective optical thickness (EOT) e_{ot} (Eq. 2.3) of the path the transmitted portion takes for each wavelength, which is twice the physical thickness d of the membrane multiplied by the effective refractive index n_{eff}, a cosine shaped interference pattern is obtained for a wavenumber $\tilde{v} = 1/\lambda$ versus intensity plot (Eq. 2.4, where ϱ_i is the incident and ϱ_t the transmitted refractive index contrast). Here, δ_{eff} is the effective phase relation (Eq. 2.5). [11, 48, 53]

$$\varrho = \frac{n_{\mathrm{m+air}} - n_{\mathrm{air}}}{n_{\mathrm{m+air}} + n_{\mathrm{air}}} \tag{2.2}$$

$$e_{\mathrm{ot}} = 2dn_{\mathrm{eff}} \tag{2.3}$$

$$R = \varrho_i + \varrho_t + 2\varrho_i\varrho_t \cos\left(2\delta_{\mathrm{eff}}\right) \tag{2.4}$$

$$\delta_{\mathrm{eff}} = 2\pi n_{\mathrm{eff}} d\tilde{v} \tag{2.5}$$

Measurement of the reflection at normal incidence can be employed for dynamic spectroscopy during the liquid infiltration of porous thin films. Multiple studies demonstrate its utility in characterizing membranes non-destructively and examining fluid properties within nanopores.[28, 33, 54–56] During fluid imbibition from one side of the membrane, illustrated in blue in Fig. 2.7 , additional interfaces emerge. The imbibition front within the porous medium minimally contributes to the reflected intensity (2). Its interface increasingly roughens during the infiltration, because of the pore size distribution. Such interface roughness induces scattering. Furthermore, the refractive index contrast of porous silicon with air and porous silicon with water is relatively small, compared to the interfaces of air to porous silicon or porous silicon to bulk silicon. At last, the surface of a bulk liquid is seldom smooth without extensive effort. The surface is normally curved or perturbed by surface waves, which leads to reflections deviating from the normal incidence path

(4).
For independent pores of axis symmetric geometry aligned with the propagation direction of an electromagnetic wave, the mean position L of the fluid front during imbibition can be measured by the change of the EOT. It represents a mean position as fluid front broadening, due to pore size distribution, is accounted for. Applying Eq. 2.3 for partial filling of air and liquid, $e_{\mathrm{ot}} = n_{\mathrm{m+air}}(d - L) + n_{\mathrm{m+liq}}L$ is obtained.[54] By normalizing the EOT to the empty and entirely filled state (Eq. 2.6), the front position is directly obtained by $L = \Delta e_{\mathrm{ot}}(t)d$. In reality pores are not perfectly uniform. Their actual geometry is one of the main topics of this thesis. Still, Eq. 2.6 is of great importance as the normalized OT is equal to the filling fraction of the pores i.e. $\Delta e_{\mathrm{ot}}(t) = V/V_0$, where V is the current volume filled and V_0 the total volume available.
The EOT can be obtained by *Fast-Fourier-Transformation* of measured interference spectra, which will be introduced in the next section. Alternatively, direct analysis of spectral extrema is feasible. It is evident from the cosine therm in Eq. 2.4 that a phase shift between beams (1) and (3) in Fig.2.7 by a multiple of $\lambda/4$ leads to the minima and maxima in the spectrum. Consequently, extrema shifts correlate proportionally with changes in EOT (Eq. 2.7).

$$\Delta e_{\mathrm{ot}}(t) = \frac{e_{\mathrm{ot}}(t) - e_{\mathrm{ot}}(t_0)}{e_{\mathrm{ot}}(t_{\mathrm{end}}) - e_{\mathrm{ot}}(t_0)} \tag{2.6}$$

$$\Delta \lambda_{\mathrm{ext}}(t) = \frac{\lambda_{\mathrm{ext}}(t) - \lambda_{\mathrm{ext}}(t_0)}{\lambda_{\mathrm{ext}}(t_{\mathrm{end}}) - \lambda_{\mathrm{ext}}(t_0)} \tag{2.7}$$

2.2.1 Reflectometric Interference Fourier Transform Spectroscopy (RIFTS)

Light reflection interferometry is a nondestructive, contactless method to measure the thickness of a material layer by its interference pattern. The reflection is measured at normal incidence. In a plot of wavelength versus intensity an interference pattern appears as an oscillating intensity with decreasing frequency to higher wavelength. Typically a wavelength range is chosen, where the material is mostly transparent and the refractive index is approximately constant. The former is rather an instrumental problem of the intensity loss due to high absorption, the latter becomes relevant in signal processing with a *Fast-Fourier-Transformation* (FFT). For application of FFT at least one full oscillation should be in the chosen spectral range. This results in a lower limit of approximately $3 - 4\,\mu\mathrm{m}$ thickness for the investigated layer.
The *Fourier-Transform* is commonly applied in signal processing, where it describes a time dependent function in the frequency domain. It decomposes a signal into sinusoidal constituents. In a simplified view the *Fourier-Transform* weights the occurrence of a repeating feature in time, giving it the highest magnitude when its

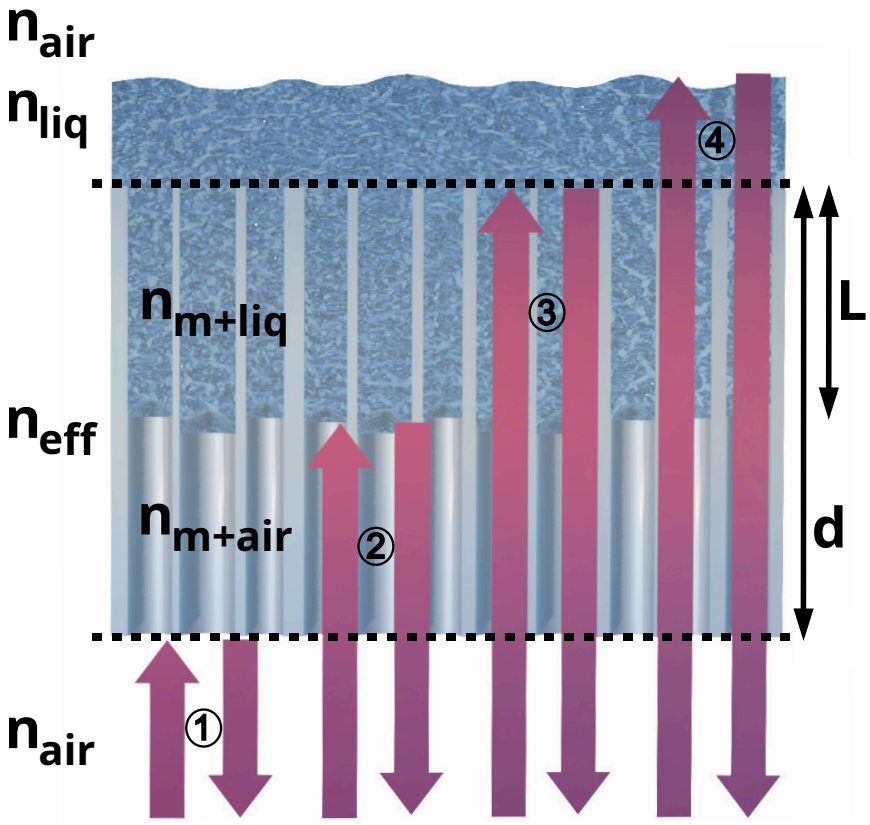

Figure 2.7: Main reflections and transmissions of white light at normal incidence on a mesoporous silicon membrane (gray) during capillary rise of a liquid (blue). The refractive index n_{eff} refers to the effective index over the entire pore length. n_{m+air} and n_{m+liq} are the effective refractive indices of the membrane with air and liquid filled pores, respectively.

frequency is matched. For the analysis of interference patterns of material layers, time is substituted by the wavenumber. This inverse of the wavelength renders the interference pattern periodic with a constant frequency. The frequency of these fringes is double the optical thickness e_{ot} through the material i.e. $2dn$, where n is the refractive index and d is the physical thickness.
Although the *Fourier-Transform* is theoretically able to deliver an exact result, apart from the uncertainty principle, in reality its precision is reduced. The FFT-algorithm is based on the discrete Fourier-Transform and the grating spectrometer, which is used throughout this work and measures discrete points in the spectrum. These two discretizations lead to the aliasing effect i.e. frequencies in the signal are not correctly transformable back and forth. Another issue is the finite spectrum. The FFT assumes that the data set is a part of a periodical signal. Abstractly viewed, the signal is wrapped around a circle. If the upper and lower border of the measured spectrum connected are forming a discontinuity, it smears out the FFT result. This is called leakage, since one frequency appears to leak into other frequencies. Windowing functions applied to the finite dataset can minimize

leakage. Various windowing functions exist, but the *Hanning* window commonly satisfies requirements for good spectral resolution, as windowing broadens peaks.[57] Further, the FFT requires equidistant points, which is usually not obtained by grating spectrometers. Therefore, data sets are interpolated with a constant step size. Notably, oversampling improves the FFT without corrupting the output. The number of sampling digits should have a power of two. This can also be accomplished by zero padding, which is an extension of the data set by zeros. Extensive zero padding has a similar improvement effect on the FFT's spectral resolution as oversampling. Both lead to higher calculation times.
Practically, the FFT spectrum should not be viewed as a continuous curve. The thickness obtained by RIFTS for a single film is a whole number multiple of the minimally detectable thickness (Eq 2.8). Consequently, the highest modulus in the spectrum is actually closest to the real thickness. Lorentzian or Gaussian fits in theory do not improve the result but on the contrary deviate even more from the real value. The highest resolution achievable by the introduced method is half of the theoretically minimal detectable thickness. Using Eq. 2.3 in combination with Eq. 2.8 and Eq. 2.9 for a wavelength range of $1000 - 1650\,\mathrm{nm}$ a minimum of $2.5\,\mu\mathrm{m}$ and maximum $5.3\,\mathrm{mm}$ are obtained. Consequently, the detection limit is approximately $1.3\,\mu\mathrm{m}$.[58]
The upper limit for the thickness determination by FFT is the *Nyquist* frequency (Eq. 2.9), where N is the number of points measured in the spectral range. Beyond this threshold, aliasing increases. In order to optimize the *Nyquist* frequency the spectral range should be maximized. This finds its limit where either the complex part of the refractive index increases or the real part deviates strongly from its mean value. The less flat the real part of the refractive index in the chosen spectral range, the stronger the error of the FFT, since unequal spacing is induced. An increase of the complex part i.e. stronger absorption, just introduces discontinuities in the data set. These have a negative impact especially if located at the borders of the spectral range. [58]

$$d_{\mathrm{RIFTS,min}} = \frac{1}{2n(k_{\mathrm{min}} - k_{\mathrm{max}})} \tag{2.8}$$

$$d_{\mathrm{RIFTS,max}} = \frac{N-1}{2n(k_{\mathrm{min}} - k_{\mathrm{max}})} \tag{2.9}$$

2.2.2 Effective Medium Approximation

In the previous subsection the FFT analysis of the interference of homogeneous thin films is introduced. This method is applicable to porous membranes as well. In the scenario considered here, both the membrane and the medium filling the pore space can be approximated as an effective medium. This approximation assumes that the pore size and interpore distance are negligible compared to the

probing wavelength, whereas the membrane's thickness must be substantial enough to provide a representative volume size.[59] Under these conditions, and assuming a minimal absorption influence, the real part of the refractive index for such a layer can be described using an effective medium approximation (EMA). In optoelectronics, the complex dielectric permittivity, denoted as $\tilde{\epsilon}$, is frequently used instead of the refractive index. Although the relationship $\epsilon = n^2$ for the real parts is valid, the discussion is held more general by using the complex dielectric permittivity. Three prevalent EMAs are the *Bruggeman-*, *Maxwell Garnett-* and *Looyenga-Landau-Lifshits*-approximation (Eq. 2.10), with the latter belonging to a class of *power-law* models.

$$\tilde{\epsilon}_{\mathrm{eff}}^{1/3} = \Phi\tilde{\epsilon}_{\mathrm{i}}^{1/3} + (1-\Phi)\tilde{\epsilon}_{\mathrm{m}}^{1/3} \tag{2.10}$$

EMA models correlate the fractions of constituents, such as porosity Φ in some systems, and their separate permittivity, $\tilde{\epsilon}_{\mathrm{i}}$ of the inclusion and $\tilde{\epsilon}_{\mathrm{m}}$ of the medium, to an effective permittivity $\tilde{\epsilon}$.[60–63]
Especially the *Bruggeman*-model is broadly applied for spectral ellipsometry on porous thin layers. In their isotropic form the *Bruggeman-* and *Maxwell Garnett-*model, Eq. 2.11 and Eq. 2.12 respectively, model the effective complex permittivity of distributed inclusions possessing isotropic optical properties within a medium.

$$\Phi\frac{\tilde{\epsilon}_{\mathrm{i}} - \tilde{\epsilon}_{\mathrm{eff}}}{\tilde{\epsilon}_{\mathrm{i}} + 2\tilde{\epsilon}_{\mathrm{eff}}} + (1-\Phi)\frac{\tilde{\epsilon}_{\mathrm{m}} - \tilde{\epsilon}_{\mathrm{eff}}}{\tilde{\epsilon}_{\mathrm{m}} + 2\tilde{\epsilon}_{\mathrm{eff}}} = 0 \tag{2.11}$$

$$\frac{\tilde{\epsilon}_{\mathrm{eff}} - \tilde{\epsilon}_{\mathrm{m}}}{\tilde{\epsilon}_{\mathrm{eff}} + 2\tilde{\epsilon}_{\mathrm{m}}} = \Phi\frac{\tilde{\epsilon}_{\mathrm{i}} - \tilde{\epsilon}_{\mathrm{m}}}{\tilde{\epsilon}_{\mathrm{i}} + 2\tilde{\epsilon}_{\mathrm{m}}} \tag{2.12}$$

An exemplified system is a suspension of small particles within a continuous medium. Assuming only isotropic optical properties are known, and the geometry of the inclusions is unknown, the *Bruggeman* approximation is advantageous due to its invariance concerning the permutation of the host medium and inclusions. It posits that the net dipole moment of the system equals zero, implying that any volume fraction induces minimal perturbation to a macroscopic, constant field. The effective complex permittivity, consequently, achieves consonance with the background. While this symmetry initially appears as a suitable general rule, shifting the fractions of inclusions and medium in incremental steps reveals many systems where it is untenable. A straightforward example is a face-centered cubic (FCC) arrangement of spheres where an intermolecular separation is sufficiently large, ensuring that the field perturbation of individual spheres in the medium remains independent. Upon abrupt exchange of host medium and inclusions, this independence is inevitably compromised if the host medium exhibits a higher permittivity.
The *Maxwell Garnett* model has a robust physical foundation, derivable from basic dipole interaction parallelisms in an external field, as elaborated elsewhere.[64] In

its isotropic form, the host medium typically occupies a substantially larger volume fraction than the inclusions. It becomes unsuitable when volume fractions become comparable.[64]

For mesoporous silicon, additional insights into the system's geometry are accessible. The silicon host medium contains nearly cylindrical, parallel-oriented pores. The effective medium approximation for such a system can be determined by the ratio (Eq. 2.13) of the volume averages of the displacement field $\langle D \rangle$ (Eq. 2.14) and electric-field $\langle E \rangle$ (Eq. 2.15).[65]

$$\tilde{\epsilon}_{\text{eff}} = \frac{\langle D \rangle}{\langle E \rangle} \tag{2.13}$$

$$\langle D \rangle = E_{\text{i}} \Phi \tilde{\epsilon}_{\text{i}} + E_{\text{m}} (1 - \Phi) \tilde{\epsilon}_{\text{m}} \tag{2.14}$$

$$\langle E \rangle = E_{\text{i}} \Phi + E_{\text{m}} (1 - \Phi) \tag{2.15}$$

In a constant external electric field and given the before mentioned prerequisites, the internal field response can be expressed by Eq. 2.16. Here, k_{i} and k_{m} are geometry-dependent factors of inclusions and medium, respectively. Considering the symmetry of the system, the expression (Eq. 2.16) has to be adapted for orthogonal and parallel polarization with respect to the main pore axis. In the parallel case the geometry-dependent factors are equal to one, since the internal electric field matches the external one. This results to Eq. 2.17 for both *Maxwell Garnett*- and *Bruggeman*-approximation. The orthogonal solution for the *Maxwell Garnett*-model can be derived by the quasi-static approximation of an infinite wire, which is $E_{\text{m}} \tilde{\epsilon}_{\text{m}} = E_{\text{i},\perp} (\tilde{\epsilon}_{\text{i}} + \tilde{\epsilon}_{\text{m}})/2$. [66] Therefore, the geometry dependent factor for the inclusions is $k_{\text{i}} = 2\tilde{\epsilon}_{\text{m}}/(\tilde{\epsilon}_{\text{i}} + \tilde{\epsilon}_{\text{m}})$ but k_{m} stays one. Eq. 2.18 is from this point on referred to as *orthogonal Maxwell Garnett* equation.[63, 65]
The *orthogonal Bruggeman* equation (Eq. 2.19) can be derived in a similar manner. It again stands out that full symmetry of host medium and inclusion fits only in very special systems. Here, one has to use the wire solutions $k_{\text{i}} = 2\tilde{\epsilon}_{\text{eff},\perp}/(\tilde{\epsilon}_{\text{i}} + \tilde{\epsilon}_{\text{eff},\perp})$ and $k_{\text{m}} = 2\tilde{\epsilon}_{\text{eff},\perp}/(\tilde{\epsilon}_{\text{m}} + \tilde{\epsilon}_{\text{eff},\perp})$ for both parts of the composite in an effective field, which does not match the actual geometry as well as the *orthogonal Maxwell Garnett* model. Experiments and numerical calculations of the band structure of porous silicon confirm this assessment (Fig. 2.8). The *orthogonal Maxwell Garnett* model loses fast in applicability if inclusions are not independent e.g. if pores are highly interconnected. The effective medium considerations of the *Maxwell Garnett* and its comparison to the *Bruggeman* model, as well as the simulations shown in Fig. 2.8 were conducted by *Julia Brandt* of the *Hamburg University of Technology*.[63]

$$\tilde{\epsilon}_{\text{eff}} = \frac{k_{\text{i}} \Phi \tilde{\epsilon}_{\text{i}} + k_{\text{m}} (1 - \Phi) \tilde{\epsilon}_{\text{m}}}{k_{\text{i}} \Phi + k_{\text{m}} (1 - \Phi)} \tag{2.16}$$

$$\tilde{\epsilon}_{\mathrm{eff},||} = \Phi\tilde{\epsilon}_{\mathrm{i}} + (1-\Phi)\tilde{\epsilon}_{\mathrm{m}} \tag{2.17}$$

$$\tilde{\epsilon}_{\mathrm{MG},\perp} = \tilde{\epsilon}_{\mathrm{m}}\frac{(1-\Phi)\tilde{\epsilon}_{\mathrm{m}} + (1+\Phi)\tilde{\epsilon}_{\mathrm{i}}}{(1+\Phi)\tilde{\epsilon}_{\mathrm{m}} + (1-\Phi)\tilde{\epsilon}_{\mathrm{i}}} \tag{2.18}$$

$$\tilde{\epsilon}_{\mathrm{B},\perp} = \frac{\Phi\tilde{\epsilon}_{\mathrm{i}}(\tilde{\epsilon}_{\mathrm{m}} + \tilde{\epsilon}_{\mathrm{eff},\perp}) + (1-\Phi)\tilde{\epsilon}_{\mathrm{m}}(\tilde{\epsilon}_{\mathrm{i}} + \tilde{\epsilon}_{\mathrm{eff},\perp})}{\Phi(\tilde{\epsilon}_{\mathrm{m}} + \tilde{\epsilon}_{\mathrm{eff},\perp}) + (1-\Phi)(\tilde{\epsilon}_{\mathrm{i}} + \tilde{\epsilon}_{\mathrm{eff},\perp})} \tag{2.19}$$

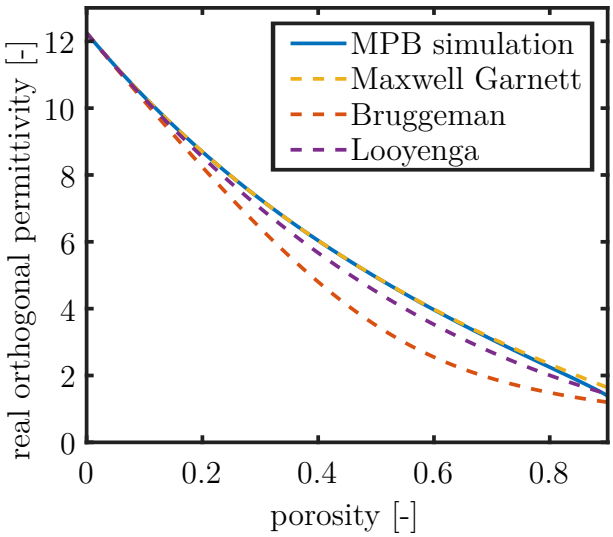

Figure 2.8: Simulations by the eigenmode solver *MIT Photonic Bands* (MPB) [67] of a hexagonal array of tubular pores and calculations by EMAs.(open access license)[63] The simulations were conducted by *Julia Brandt* from the *Hamburg University of Technology*. For *Maxwell Garnett* and *Bruggeman* the orthogonal equations are used. The *Looyenga-Landau-Lifshits* mixing rule does not offer an adaption to the anisotropy. The calculations are conducted with the literature values of $\epsilon_{\mathrm{Si}} = 12.25$ [68] and $\epsilon_{\mathrm{air}} = 1$ [69].

The introduced EMAs provide a means to determine the porosity of a porous thin film when the effective complex permittivity or, in cases of low absorption, the real refractive index is known. It can be measured by the previously introduced RIFTS method using Eq. 2.3 ($e_{\mathrm{ot}} = 2dn_{\mathrm{eff}}$). If the thickness of the porous layer is known, the porosity can be calculated directly. Both Eq. 2.3 and the selected EMA, e.g. *orthogonal Maxwell Garnett*, can be rearranged for the effective refractive index and set equal (Eq. 2.20). The refractive indices of the elements can be taken from literature.
In instances where both thickness and porosity are unknown, a method called

spectral liquid infiltration method (SLIM) [11] can be applied. For this method a membrane is filled by two different substances measuring the respective EOT of the composite. Usually, air and a volatile liquid are chosen. This ensures a nondestructive measurement. Evaluation of the measurement results in two instances of Eq. 2.20 with two unknowns, namely thickness and porosity, which can be resolved either analytically or through numerical approximation.[11]

$$\sqrt{n_{\mathrm{m}}^2 \frac{(1-\Phi)n_{\mathrm{m}}^2 + (1+\Phi)n_{\mathrm{i}}^2}{(1+\Phi)n_{\mathrm{m}}^2 + (1-\Phi)n_{\mathrm{i}}^2}} - \frac{e_{\mathrm{ot}}}{2d} = 0 \tag{2.20}$$

2.2.3 Photonic Crystals (PC)

1-D photonic crystal structures based on mesoporous silicon (PSi) are here engineered to achieve a distinct optical feature through resonance in the visible light spectrum. This is realized by an optical *microcavity*. Its structure comprises alternating layers of differing refractive indices, which can be fabricated tuning the porosity of PSi. The porosity is controlled via the current density, while the thickness is determined by the application duration. Without the need of a fitting EMA, one can etch porous layers for a fixed time, alternating the current density for different samples. The EOT and the spectral appearance of these calibration samples is determined by reflection spectroscopy. With these measured spectra it is possible to realize any reflection pattern by stacking mesoporous silicon layers, using the superposition of m wave functions ψ_{m} (Eq. 2.21).[11, 70]

$$\psi = \frac{\sum_{\mathrm{m}} \psi_{\mathrm{m}}}{\mathrm{m}} \tag{2.21}$$

The 1-D photonic crystal that is aimed for here, is very similar to a *Bragg*-reflector. This reflector consists of layers with alternating refractive indices, but each layer maintains the same EOT, meaning the layer with the higher refractive index is physically thinner. Such a *Bragg* reflector generates a photonic bandgap, resulting in high reflection over a specific wavelength range, termed the *stop band*. Its center position λ_{sb} in the wavelength spectrum is chosen by the EOT of the layers by $\lambda_{\mathrm{sb}} = 4nd$. Depending on the desired reflectivity several layers are stacked. The width of the stop band is proportional to the refractive index contrast and can be expressed by Eq. 2.22, where n_{h} and n_{l} are the refractive indices of the higher and lower porosity layer, respectively.[71]
By inserting a porous layer of $e_{\mathrm{ot}} = 2dn_{\mathrm{eff}}$ in the middle of two *Bragg*-stacks of arbitrary number, an optical *microcavity* is produced. This *microcavity* leads to a sharp valley in the stop band's reflection spectrum. Its tip λ_{PC} is responsive to any change of the effective refractive index at that central defect layer e.g. by substitution of air in the pore space with a higher refractive index material.[11, 31, 33, 72] Fig. 2.9 a) shows the physical structure and refractive index profile of

this kind of photonic crystal. The optical properties can be calculated by *transfer matrix method* and an EMA as demonstrated in b), where R is the reflection, T the transmission and *Abs* the absorption curve.

$$\Delta\lambda = \frac{2\lambda_{\mathrm{sb}}}{\pi} \arcsin\left(\frac{n_{\mathrm{h}} - n_{\mathrm{l}}}{n_{\mathrm{h}} + n_{\mathrm{l}}}\right) \tag{2.22}$$

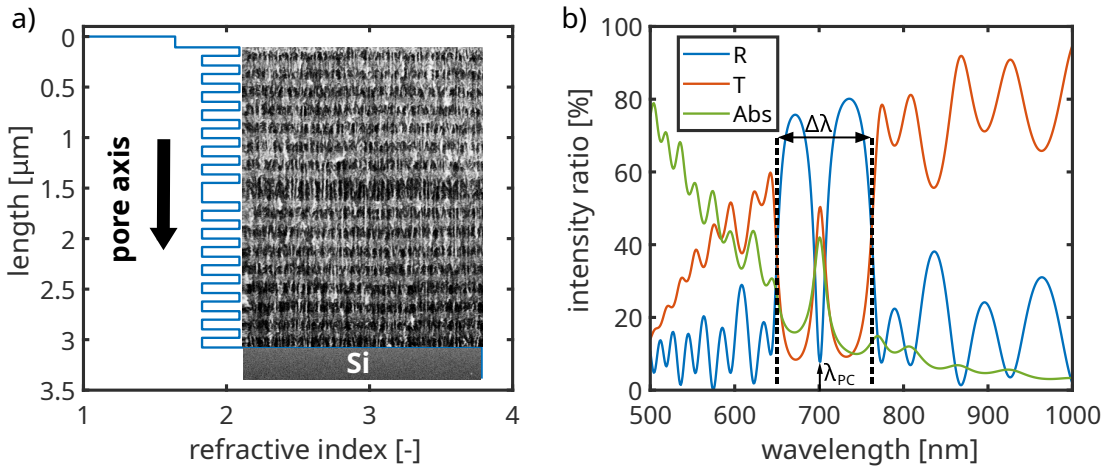

Figure 2.9: Porous silicon 1-D photonic crystal: a) effective, real part of the refractive index and its extend, together with an aligned SEM image of the cutting edge parallel to the main pore axis, b) calculated reflection, transmission and absorption spectra by *transfer matrix method* and *Looyenga* effective medium approximation. The *Matlab* script is provided by Raul Urteaga (Consejo Nacional de Investigaciones Científicas y Técnicas).

2.2.4 Chip Like Reflective Sensor (CLRS)

In this thesis, a *chip like reflective sensor* (CLRS) is designed for the use in conjunction with white light spectroscopy. The CLRS is composed of a homogeneous porous thin film (*Fabry-Pérot* layer) and an optical *microcavity*. Both are produced in a single etching procedure from a commercial silicon wafer. The homogeneous porous layer can be viewed as a column adjustable in thickness and porosity to investigate different infiltration run times. Additionally, the CLRS can be modified in terms of surface chemistry. As synthesized the pore walls are hydrogen terminated. Unlike bulk silicon, the pore interiors do not oxidize rapidly under standard laboratory conditions, maintaining their original hydrophobic state. The surface may be altered to become hydrophilic via thermal, chemical, or electrochemical oxidation. A silicon-dioxide layer can further be used for silanisation i.e. anchoring of hydrocarbons at the surface (see appendix B.2). During spectroscopic analyses, the overall filling is inferred from changes in the effective optical thickness (EOT)

of the total stack of porous layers, achieved by recording *Fabry-Pérot* fringes with a near-infrared spectrometer. Complementary, the photonic crystal acts as a local sensor, that can be positioned at different heights of the homogeneous porous layer. Its filling state is measured by its resonance wavelength with a spectrometer in the visible wavelength spectrum.
Cencha et al. [31] have demonstrated the analysis of fluid front shapes of polymers with a precision down to the sub-nanometer scale, by analyzing the resonance of 1-D *microcavity* based PC only and modeling the fluid dynamics in a homogeneous porous layer in front. In their study on liquids, the PC is positioned subsequent to the homogeneous layer. The positioning and higher thickness of the latter ensures that the porosity modulations of the PC have a minor impact on the measured dynamics.
Investigations involving biomolecules have utilized a combination of rugate filters (photonic crystals) and *Fabry-Pérot* layers, where intensity changes are measured instead of phase shifts, examining the interface between the porous layer and the analyte by refractive index contrast.[72] The sinusoidal pore trace of a rugate-filter spanning over the entire porous layer can be expected to have a high impact on the fluid dynamics though. Furthermore, the measurement of intensities is more prone to scattering e.g. by a broadening fluid front or the formation of bubbles.
For infiltration experiments with liquids here, the layer configuration of Cencha et al. [31] is chosen (Fig. 2.10), with the addition of simultaneous measurement of *Fabry-Pérot* fringes. Since the liquids are non-polar, the surface is left hydrogen terminated.

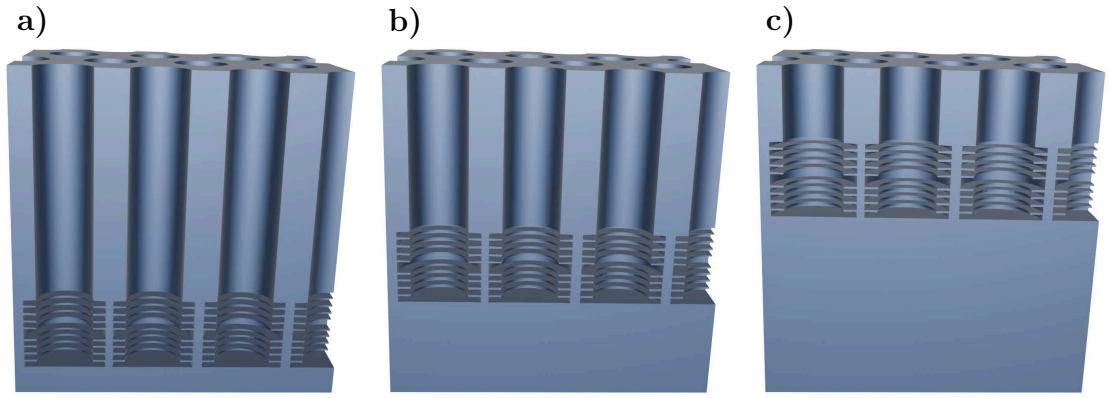

Figure 2.10: Configuration for investigation of liquids: Three samples with decreasing thickness of a homogeneous porous layer from a) to c) for different imbibition lengths, followed by a PC. The *Bragg*-layers with smaller pore radius and therefore lower porosity are thinner than the ones with higher porosity, both are equal in the EOT. The layer of twice the EOT at the center of the stacks is the central cavity.

In experiments on water ad- and desorption, the PC is positioned at different heights of the homogeneous porous layer (Fig. 2.11), aiming for local information on the transport mechanism. For these measurements the CLRS's surface is oxidized. The oxidation is kept minimal to sustain the optical characteristics, since a full oxidation induces an unequal change of the EOT of layers with different porosity.

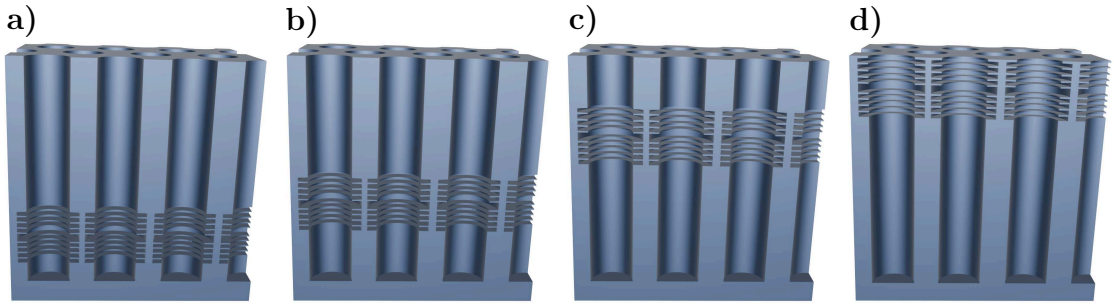

Figure 2.11: CLRS for water ad- and desorption measurements. The PC is positioned at decreasing distance from the free surface from a) to d) in a homogeneous porous layer of constant volume. The sides and the bottom of the pores are closed by bulk material. Notably, a PC at the center of the homogeneous layer is avoided. The porous layers below and above the PC would be equal in thickness as well as effective refractive index and therefore cannot be differentiated by their EOT.

2.3 Capillary Imbibition in Nanopores

Liquid transport in nanopores is to this day not fully understood, and elaborate techniques are necessary investigate it. The section under review focuses on capillary phenomena involving solid-liquid interactions under specific atmospheric conditions. From a macroscopic perspective this is linked to the wettability of a solid by a liquid droplet. The perimeter of the droplet where solid, liquid and vapor apparently coexist is termed contact line. On the microscopic scale the position of the contact line differs, because of a nanometer thin liquid layer advancing ahead of the macroscopic front.[73] It is further assumed that the droplet is small enough to neglect gravity but large enough that effects close to the contact line are also not dominant. Then a small displacement of the contact line on a flat and chemically homogeneous substrate, when the bulk energies of liquid and vapor are in equilibrium, can be described by the *Young* equation (Eq. 2.23). It relates the surface tensions of the interfaces solid/vapor (σ_{sv}), solid/liquid (σ_{sl}) and liquid/vapor (σ_{lv}) together with the macroscopic, equilibrium contact angle θ_{e}. The latter is the angle of the tangent towards the droplet starting in the microscopically apparent contact line. It can be differentiated in complete wetting $\theta_{\mathrm{e}} = 0°$, partial wetting $0° < \theta_{\mathrm{e}} < 90°$ and non-wetting.[74]

Capillary imbibition is the infiltration of a liquid into a solid scaffold driven by a liquid meniscus and energy minimization. This manifests e.g. if a liquid droplet infiltrates a glass capillary self driven against gravity, when the equilibrium contact angle is smaller than 90°. Liquid transport is usually discussed as pressure driven. The driving pressure in capillary transport arises from the pressure difference Δp of the liquid and its surrounding vapor phase. It is directly apparent from the curvature $C = r_1^{-1} + r_2^{-1}$ of the liquid meniscus with σ_{lv} as a proportionality constant. This relation is known as the Young-Laplace Equation.[75] The curvature of the liquid meniscus inside a capillary will be approximated as hemispherical in the following, which leads to the simplification $C = 2/r_{\mathrm{YL}}$.

$$\sigma_{\mathrm{sv}} - \sigma_{\mathrm{sl}} - \sigma_{\mathrm{lv}} \cos\theta_{\mathrm{e}} = 0 \tag{2.23}$$

$$\Delta p = \frac{2\sigma_{\mathrm{lv}} \cos\theta_{\mathrm{e}}}{r_{\mathrm{YL}}} \tag{2.24}$$

At the nanopore scale, gravity's influence remains negligible, similar to the previously described small droplet scenario. This is underscored by the very small dimensionless Bond numbers, which weigh hydrostatic pressure against capillary pressure.[76] The small pore size d_{pore} goes along with low Reynolds numbers (Re, Eq. 2.25) where flow is laminar. This dimensionless quantity of fluid flow, which includes the characteristic size (here d_{pore}), and fluid parameters such as density ρ_{f}, characteristic velocity u_{f} and viscosity μ_{f}, represents the relationship between inertial and viscous forces.

$$Re = \frac{\rho_{\mathrm{f}} u_{\mathrm{f}} d_{\mathrm{pore}}}{\mu_{\mathrm{f}}} \tag{2.25}$$

2.3.1 Capillary Imbibition in a Tube

Laminar flow in cylindrical pipes follows the well known *Hagen-Poisseuille* law (Eq. 2.26). It describes the volumetric flow $\dot{Q}_{\mathrm{t}}$ through a tube with length L and radius r driven by a pressure difference Δp along it and postulates a parabolic profile of the fluid velocity (Fig. 2.12). The fluid is assumed to have a constant viscosity μ i.e. a Newtonian fluid. During the initial stages of imbibition the velocity profile establishes. The length until *Hagen-Poiseuille* flow is accomplished can be approximated by $L_{\mathrm{e}} = 0.058Re \cdot d_{\mathrm{pore}}$.[77] Evidently, for large aspect ratios of length to radius this is only a very small portion of the imbibition and therefore insignificant.

$$\dot{Q}_{\mathrm{t}} = \frac{\pi r^4 \Delta p}{8\mu\ L} \tag{2.26}$$

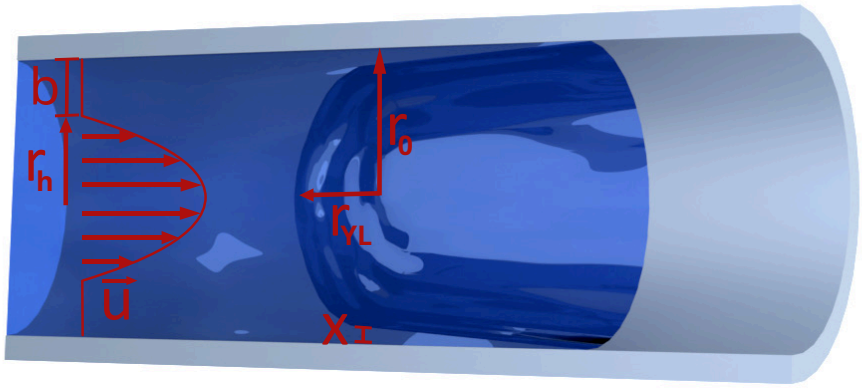

Figure 2.12: capillary imbibition in a tube with a pre-wetting layer in front of the main meniscus ($r_0 = r_{\mathrm{YL}} + x$). The parabolic velocity profile is reduced by an immobile layer, therefore the hydraulic radius is smaller than the geometrical one ($r_{\mathrm{h}} = r_0 + b$).

Capillary infiltration in an ideal tube (Fig. 2.12) can be described by the Lucas-Washburn equation (Eq. 2.27). It relates the driving Young-Laplace pressure to the counteracting viscous drag in a $\sqrt{t}$ versus imbibition length L dependency and is derived by the area mean velocity, $\dot{L} = \dot{Q}_{\mathrm{t}}/\pi r^2$, of *Hagen-Poiseuille* flow (Eq. 2.26). Γ_{l} is the penetrativity of a fluid i.e. its power to imbibe.[35, 78]

$$L(t) = \sqrt{\frac{r\sigma_{\mathrm{lv}} \cos\theta_{\mathrm{e}}}{2\mu} t} = \Gamma_{\mathrm{l}} \sqrt{rt} \tag{2.27}$$

At the nanopore scale, research frequently involves arrays of pores rather than isolated capillaries. In materials with a pore size distribution where the pores are parallelly aligned, uniform along their axes, and non-interconnected, Equation 2.27 applies for predicting the imbibition behavior using the mean radius. Alternatively, fitting measurements of imbibition length versus time with known bulk fluid parameters allows derivation of a representative pore radius. The imbibition front, indicating the fluid menisci's position within individual pores, broadens over time in proportion to the square root of time. Capillaries with smaller pore radii exhibit higher capillary pressures, however, they also experience greater viscous drag. In nanopores, this increased drag predominates, leading to slower filling of smaller pores. This scenario enables the estimation of the pore size distribution from imbibition time versus length measurements, accounting for broadening. Conversely, if the pore size distribution is known, it is possible to calculate the broadening of the imbibition front.[16]
The analysis to this point assumes no-slip boundary conditions at the interface between the pore wall and the fluid. In practice, an apparent slip is often hypothesized to account for observed mean velocity deviations and refers to an increased

viscous drag between liquid layers close to the wall. It is differentiated from true slip, which is a molecular level description of the fluid-wall interaction and cannot be zero. Positive, apparent slip extends the velocity profile beyond the capillary diameter, while negative slip reduces it. This subject is discussed extensively in literature, a recent summary focuses on nanoconfined water.[79] During spontaneous imbibition ($\theta_e < 90°$), negative slip is associated with a higher viscosity with a certain extend from the wall. Its exact analysis requires considerable effort [79], which is not the scope of this thesis. However, the correction of the fluid velocity profile by an immobile layer can be introduced by a negative slip length b from the geometrical radius r_0 of the pore. This leads to the introduction of a hydraulic radius Eq. 2.28.[16, 37, 80, 81] Positive slip is expected to occur for non-wetting conditions only ($\theta_e > 90°$) and therefore in forced imbibition. In summary capillary imbibition in cylindrical nanopores can be described by the driving Young-Laplace pressure and the viscous drag by *Hagen-Poisseuille's* law, including an immobile layer correction.

$$r_h = r_0 + b \tag{2.28}$$

Often, the capillary filling process can be described through modifications of the *Lucas-Washburn* equation or the underlying *Hagen-Poiseuille* law. If the capillaries deviate from a perfectly straight cylinder by a meandering pathway, a straight capillary of the same overall path length for the fluid can be calculated. Then, a streamline tortuosity τ_s, which reflects the course of the streamlines, is introduced as a linear elongation factor for the imbibition length $L_s = L_0\tau_s$.[54]
A further modification arises from the non-circular shape of pores. Cai et al. [82] suggested to introduce a shape factor as a multiplicand for the radius, which is 1 for a round shape and slightly higher for e.g. squares and triangles, in both *Hagen-Poisseuille* and *Young-Laplace equation*. This modification is useful in single capillaries or if the pore shapes of an array of capillaries is well known. In mesoporous membranes, where often billions of pores are measured in parallel, the shape factor can only be justified if a systematic shape variation is present.
A common occurrence in mesoporous materials is the axial pore size variation. Moderate pore radius changes, where the lubrication approximation $|\mathrm{d}r/\mathrm{d}L| << 1$ is valid, without large step changes in pore radius, are explored in subsequent sections. Additionally, *Darcy's* law is introduced for describing the imbibition in interconnected pores and the dimensionally dependent flow.

2.3.2 Darcy's Law

To this point, capillary imbibition in mesoporous materials with parallel and unconnected pores is considered by the *Lucas-Washburn* equation. In its original form, denoted as Eq. 2.27, the power of a liquid to imbibe is expressed by the penetrativity. The porous framework is characterized solely by the pore radius. Certain

adaptations, such as the incorporation of a representative hydraulic radius $\langle r_\mathrm{h} \rangle$ or a tortuosity can be implemented by simple modifications (Eq. 2.29). The geometrical parameters can be summarized as the permeability of the porous material Γ_pm. This effectively segregates the descriptors of imbibition between bulk liquid properties and the characteristics of the scaffolding material, although this delineation does not apply strictly to contact angle and immobile layer thickness. The distinction between permeability and penetrativity is beneficial for forecasting flow behavior in scenarios where either the liquid or the porous substrate undergoes change or modification.

$$L(t) = \sqrt{\frac{\langle r_\mathrm{h} \rangle}{\tau_\mathrm{s}^2}} \Gamma_\mathrm{l} \sqrt{t} = \Gamma_\mathrm{pm} \Gamma_\mathrm{l} \sqrt{t} \tag{2.29}$$

The permeability of isotropic porous media was investigated by *Darcy* in 1856. From his experiments a differential relation is derived (Eq. 2.30) that has proven its value in characterizing imbibition in different geometries including 2D and 3D problems as well as interconnected pore networks. *Darcy's* law links the flow due to a pressure gradient, by the ratio of a fluids viscosity and the permeability tensor K of the infiltrated medium to a superficial velocity u.[17]

$$-\nabla p = \frac{\mu}{K} u \tag{2.30}$$

Revisiting the capillary imbibition in a mesoporous material with an array of independent pores with *Darcy's* law, the permeability tensor can be simplified. With the introduction of the concept of a representative elementary volume (*rev*), following the arguments by Lake[17], one can relate the travel time through a tube to the individual fluid elements by Eq. 2.31. Here, v_rev is the local velocity of a *rev* related to the superficial velocity u by the geometrical porosity Φ_0, at a certain imbibition length L_rev. The denominator on the right hand side of Eq. 2.32 is the mean velocity of Hagen-Poiseuille's law. Given the discrete gradient $\Delta p / L_\mathrm{rev}$ in conjunction with Eq. 2.31, Eq. 2.32 and Eq. 2.30 the permeability Eq. 2.33 can be derived. The here derived *Darcy* tortuosity τ_D differs from the definition from streamlines used for the *Lucas-Washburn* equation above.

$$\frac{L_\mathrm{rev}}{v_\mathrm{rev}} = \frac{L_0}{\dot{Q}_\mathrm{t} / \pi r_0^2} \tag{2.31}$$

$$v_\mathrm{rev} = u / \Phi_0 \tag{2.32}$$

$$K = \frac{\Phi_0 r_\mathrm{h}^4}{8 \left(\frac{L_0}{L_\mathrm{rev}} \right)^2 r_0^2} = \frac{\Phi_0 r_\mathrm{h}^4}{8 \tau_\mathrm{D} r_0^2} \tag{2.33}$$

By integration of the discrete form of *Darcy's* law and inserting the permeability along with the driving capillary pressure (Eq. 2.24), a general description (Eq. 2.34) of flow in materials with an array of independent capillaries is derived. The radius $r_{\mathrm{YL}} = r_0 - x$, accounts for preadsorbed molecular layers of thickness x ahead of the main meniscus influencing the Young-Laplace pressure. Preadsorbed layers appear for example due to vapor deposition at the pore wall or a precursor film. Although the extend of x can be on the same order as the slip length b (Eq. 2.28) they are different, as the former influences the driving pressure at the fluid front and the latter the hydraulic resistance behind it. Preadsorbed molecules tend to be bounded strongly to the pore walls and are therefore also a likely part of the dead layer in the resistance to flow, but the actual slip length can differ. For the same reason the hydraulic porosity Φ_{h} is based on the slip length and not preadsorbed layers.
In case x and b are negligibly small, Eq. 2.34 can be simplified to Eq. 2.35. Comparing the modified *Lucas-Washburn* equation (Eq. 2.29) and Eq. 2.35, the relation $\tau_{\mathrm{s}} = \sqrt{\tau_{\mathrm{D}}}$ is obtained. Neither solution describing a meandering pathway in imbibition have been decisively validated. Darcy's method posits a *rev* length shortening with increasing pore deviation from a linear path, presuming self-similarity at a particular scale suffices in describing major structural perturbations impacting flow. The streamline approach suggests an elongated path with increasing tortuosity. Both definitions suggest that the tortuosity concept accounts for moderate pathway deviations, as abrupt changes fall outside the lubrication approximation's applicability.

$$L(t) = \sqrt{\frac{\Phi_0\ r_{\mathrm{h}}^4}{\Phi_{\mathrm{h}}\ r_0^2 r_{\mathrm{YL}} \tau_{\mathrm{D}}}}\Gamma_{\mathrm{l}}\sqrt{t} \tag{2.34}$$

$$L(t) = \sqrt{\frac{r_0}{\tau_{\mathrm{D}}}}\Gamma_{\mathrm{l}}\sqrt{t} \tag{2.35}$$

2.3.3 Inverse Problem of Capillary Filling

In capillary filling studies, the focus typically lies on investigating the imbibition dynamics, where both the driving pressure and pore geometry are known. Conversely, in *the inverse problem of capillary filling*, the primary variable of interest is the pore radius. The imbibition dynamics are measured the driving pressure is known or measured as well. At the mesopore scale, material defects are frequently unavoidable, particularly during etching or leaching processes, leading to gradients in pore radius.[42, 43, 56] Axial pore variations are intentionally designed in certain applications, including conical liquid diodes [83], capillary components analogous to electrical circuit elements [84], or nanofluidic membranes for osmotic energy conversion [85]. Non-destructive methods to resolve the geometry at that scale

require elaborate experimental techniques e.g. scanning electron or atomic force microscopy and x-ray diffraction techniques [42].

The method introduced here employs the dynamics of capillary infiltration of a volatile probing liquid to determine the pore radius. The foundational work on *the inverse problem of capillary filling* was conducted by *Elizalde* et al.[39], who proposed that solving the inverse problem for a single imbibition direction yields a spectrum of potential solutions with varying axial pore deviations. Their solution involved analyzing the imbibition dynamics from one end and, after drying, from the opposite end of a pore via an iterative approach, solving Eq. 2.36. In their experiment, a camera directly observed the imbibition length in a glass tube. Furthermore, this technique extended to assess the axial pore variation of a nanopore array in an anodized aluminum oxide membrane, utilizing laser interferometry to capture the volumetric filling fraction during capillary imbibition. To evaluate the pore radius from the filling fraction over time data, the inverse solution has to be modified by Eq. 2.37.
Khatoon et al. derived an analytical solution for the inverse problem using imbibition from both ends of a capillary by summing up the integrals for both imbibition directions.[40] They provided the solution for the imbibition length only.

$$r(l) = \frac{f(l)^{\frac{1}{3}}}{\Gamma_{\mathrm{l}}^*} \int_0^{L_0} f(x)^{-\frac{4}{3}} \mathrm{d}x \tag{2.36}$$

$$\mathrm{d}V = \pi r(x)^2 \mathrm{d}x \tag{2.37}$$

The analytical solution for fluid flow under axial pore variation can be derived using *Darcy's* law in combination with the *Hagen-Poiseuille's* law.[38] In case of moderate changes of the pore radius, where the lubrication approximation $|\mathrm{d}r/\mathrm{d}L| << 1$ holds, the radius can be integrated over the imbibition length. The local penetrativity is represented as $\Gamma_{\mathrm{l}}^* = \sigma_{\mathrm{lv}} \cos(\theta_{\mathrm{e}} + \mathrm{d}r/\mathrm{d}L)/\mu$. To determine the pore radius from imbibition dynamics, both forward and reverse capillary infiltration are considered. From the measuring perspective there are experiments where the imbibition length over time can be measured directly. In this case forward and reverse imbibition can be solved with Eq. 2.38 and Eq. 2.39, respectively. In the techniques used in this thesis the volumetric filling fraction is measured. Therefore, Eq. 2.38 and Eq. 2.39 are transformed for volume flow via Eq. 2.37.

$$u_{\mathrm{f}} = \frac{\mathrm{d}l}{\mathrm{d}t} = \frac{\Gamma_{\mathrm{l}}^*}{4r(l)^3 \int_0^l r(x)^{-4} \mathrm{d}x} \tag{2.38}$$

$$u_{\mathrm{r}} = -\frac{\mathrm{d}l}{\mathrm{d}t} = \frac{\Gamma_{\mathrm{l}}^*}{4r(l)^3 \int_l^L r(x)^{-4} \mathrm{d}x} \tag{2.39}$$

$$\dot{Q}_{\mathrm{f}} = \frac{\mathrm{d}V}{\mathrm{d}t} = \frac{\Gamma_{\mathrm{l}}^* \pi^2}{4r(x) \int_0^V r(V)^{-6} \mathrm{d}V} \tag{2.40}$$

The analytical solution for the inverse problem using volume as the variable parallels the work of Khatoon et al.[40]. Given the mathematical symmetry in forward and reverse imbibition equations, only the former is detailed here. The total integral I (Eq. 2.41) spans over the forward and reverse imbibition simultaneously (Eq. 2.42), based on Eq. 2.40. Rearranging Eq. 2.42 for $r(x)$ and simplification with Eq. 2.43 leads to the expression Eq. 2.44. This expression is inserted in Eq. 2.41 and rearranged to Eq. 2.45. Thereby an integral depending on the volume flows in both direction is obtained. This can be used in Eq. 2.44 rendering the right side independent of the radius, which leads to the result (Eq. 2.46) of this derivation for the volume flow. Experiments that quantify the normalized filling fraction facilitate linking volume change to the filling fraction, using Eq. 2.47, which is multiplied by the pore's total volume V_0. This total volume can be determined through alternative techniques, such as nitrogen sorption isotherms.
Subsequently, the pore radius at each point of filling fraction measurement is calculated using Eq. 2.46 in conjunction with Eq. 2.47, employing trapezoidal numerical integration. Furthermore, the imbibition length is determined by cumulatively summing the results, in accordance with Eq. 2.37.

$$I = \int_0^{V_0} r(V)^{-6} \mathrm{d}V \tag{2.41}$$

$$I = \int_0^{V} r(V)^{-6} \mathrm{d}V + \int_V^{V_0} r(V)^{-6} \mathrm{d}V = \frac{\Gamma_1^* \pi^2}{4 r(x)} \left(\frac{1}{\dot{Q}_\mathrm{f}} + \frac{1}{\dot{Q}_\mathrm{r}} \right) \tag{2.42}$$

$$f(V) = \frac{1}{4} \left(\frac{1}{\dot{Q}_\mathrm{f}} + \frac{1}{\dot{Q}_\mathrm{r}} \right) \tag{2.43}$$

$$r(x) = \frac{\Gamma_1^* \pi^2 f(V)}{I} \tag{2.44}$$

$$I = \left(\frac{\Gamma_1^{*6} \pi^{12}}{\int_0^{V_0} f(V)^{-6} \mathrm{d}V} \right)^{\frac{1}{5}} \tag{2.45}$$

$$r(x) = \frac{f(V)}{\Gamma_1^{*\frac{1}{5}} \pi^{\frac{2}{5}}} \left(\int_0^{V_\mathrm{tot}} f(V)^{-6} \mathrm{d}V \right)^{\frac{1}{5}} \tag{2.46}$$

$$\mathrm{d}V = \mathrm{d} \left(\frac{V - V_\mathrm{min}}{V_\mathrm{max} - V_\mathrm{min}} \right) V_0 \tag{2.47}$$

The now derived volume solution for the imbibition from both ends of a capillary is tested for the glass capillary experiment investigated in the first works on the inverse problem.[39, 40] Since measured data sets are not continuous functions but discrete points, differentiation and integration are done numerically. The imbibition length versus time measurement curves are depicted on the left side of Fig. 2.13. They are smoothed by a three point moving average. On the right side the same dynamics are displayed for the volume using Eq. 2.37. To solve the inverse problem for imbibition from both entrances, the dynamics from one side have to be reversed in order. This is shown on the left side of Fig. 2.14 for the volume case. The radius is then calculated by Eq. 2.46 using trapezoidal numerical integration (trapz in MATLAB) evaluated at the mean of neighboring points. On the right side of Fig. 2.14 good agreement is found for both length and volume solution of the problem.

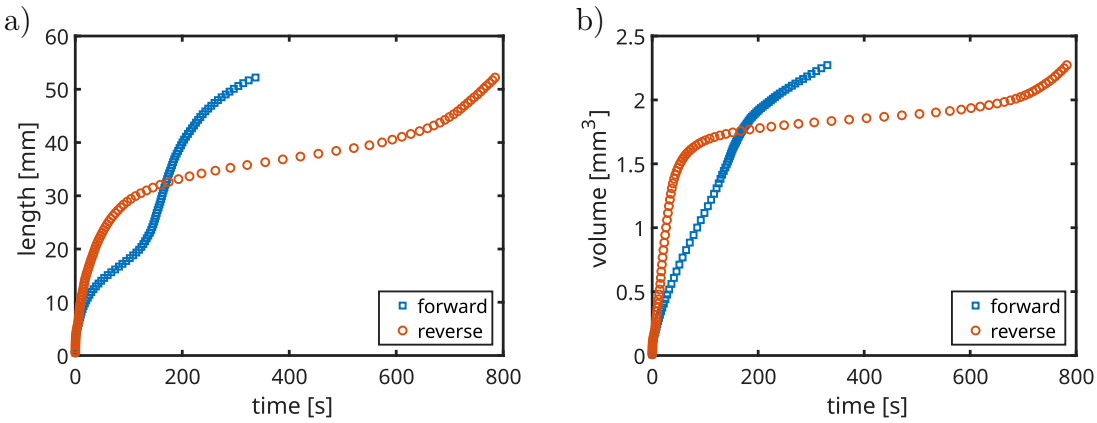

Figure 2.13: dynamics of capillary imbibition in a glass tube. a) Imbibition length against time. b) Imbibed volume versus time. (licensed reuse of the data)[39]

2.3.4 Constriction Model

In the following, a fluidic model is derived to capture the primary mechanism of fluid transport in porous materials with a repetitive bottle-neck building block (Fig. 2.15).[86–90] A key requirement is that the overall length of the imbibition path is significantly greater than the length of the repetition unit.[90] Initially, a model is introduced for solid scaffold materials exhibiting a random distribution of segments with varying pore sizes. These segments typically possess an aspect ratio close to one in actual porous media.[86] Given that the diameters are on the nanoscale and the overall imbibition length is on the microscale, this model is adequately justified.
Assuming capillary imbibition in an array of m_p independent pores within a mesoporous membrane, the description is attained by analyzing a representative capillary. With this similarity within the material, the porosity can be expressed by

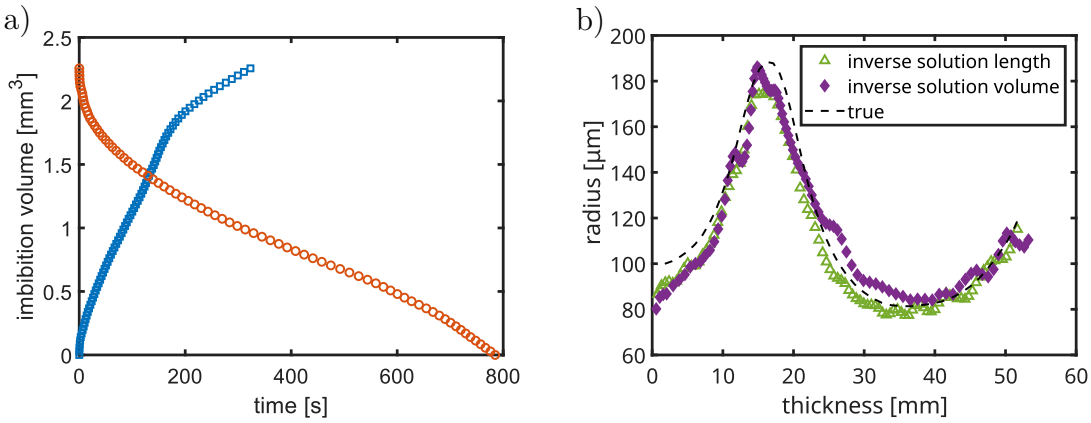

Figure 2.14: Inverse problem solution of capillary imbibition in a glass tube. a) capillary imbibition curves from imbibition from both sides. For the reverse imbibition curve the imbibition data is subtracted from the last point in time of the measurement. b) Radius courses in comparison. The "true", i.e. measured, geometry is provided by Elizalde et al..(licensed resuse)[39]

Eq. 2.48, with the cross sectional area A, which is perpendicular to the long axis of the pores and the overall thickness L along them.[90] The flow rate through a representative pore is taken from the previous subsection (Eq. 2.38). Consequently, the overall flux $\dot{Q}_{\mathrm{tot}}$ is the product of the single fluxes and m_{p} (Eq. 2.49). The $m-$th probability moment of the radius distribution is defined in Eq. 2.50. It can be applied to Eq. 2.49 to define a representative capillary radius for an array of uniform tubes by Eq. 2.51.[90]

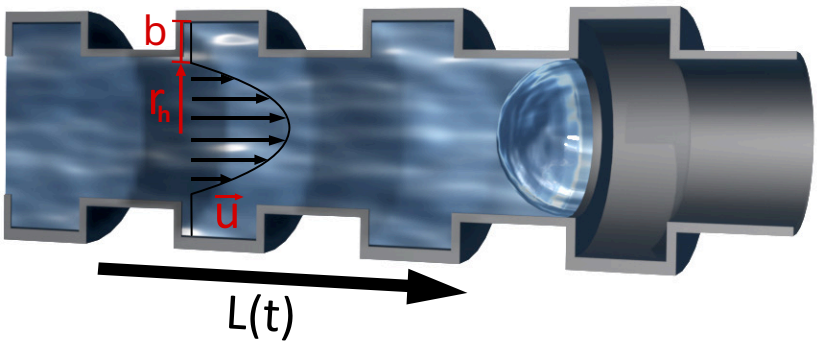

Figure 2.15: Illustration of the constriction model. The parabolic shape of the velocity profile is preserved and the immobile layer b assumed to be constant for the material composition.

$$\Phi = \frac{m_{\mathrm{p}}\pi \int_0^L r(x)^2 \mathrm{d}x}{AL_0} \tag{2.48}$$

$$\dot{Q}_{\mathrm{tot}} = \frac{\Phi A \Delta p}{8\mu L \int_0^L r(x)^2 \mathrm{d}x \int_0^L r(x)^{-4} \mathrm{d}x} \tag{2.49}$$

$$\langle r^m \rangle \equiv \frac{1}{L} \int_0^L r(z)^m \, dz \tag{2.50}$$

$$r_{\mathrm{ut}} \equiv \sqrt{\frac{1}{\langle r^{-4} \rangle \langle r^2 \rangle}} = \sqrt{\frac{8\mu L \dot{Q}_{\mathrm{tot}}}{\Delta p \Phi A}} \tag{2.51}$$

In the flow through a stack of cylinders with two different diameters mass continuity is conserved (Eq. 2.52). A primary distinction from a uniform tube is the ratio between the cross-sectional areas of the fluid meniscus, denoted as $A(l)$ and the capillary $A(x)$ situated posteriorly. Eq. 2.53 represents the discrete adaption of *Darcy's* law for this case. Given a simplified permeability $K = r(x)^2/8$ without immobile layer and tortuosity (compare Eq. 2.33), Eq. 2.52, Eq. 2.53 and the Young-Laplace pressure (Eq. 2.24) are combined to Eq. 2.54. The inner integral on the right side of Eq. 2.54 is substituted by the momentum equation (Eq. 2.50) dividing it into a meniscus position dependent and independent part (Eq. 2.55). The remaining integral can be solved by partial integration, but a more applicable solution is obtained by the argument of large numbers of the repetition unit. Considering the total length L of the imbibition path is suitable expressed by the number of repetition units m_{ru} with length l_{ru} as $L \approx m_{\mathrm{ru}} l_{\mathrm{ru}}$, the integral can be approximated by Eq. 2.56. Since m_{ru} is large, the sum can be further simplified to $\langle r^3 \rangle {l_{\mathrm{ru}}}^2 \sum_{i=1}^{m} i \approx \langle r^3 \rangle L^2/2$, thus Eq. 2.57 is derived. Similar to the representative capillary radius of uniform tubes such equivalent radius r_{eq} (Eq. 2.58) is obtained here for the further on termed *constriction model*. This result draws a direct connection to the *Lucas-Washburn* equation (Eq. 2.27), where the apparent radius r_{app} in a measurement can substitute the radius in the prefactor. This derivation is a summary based on [38, 86, 87, 89–91].

$$u(x) = \frac{\mathrm{d}l}{\mathrm{d}t} \frac{A\,(l)}{A\,(x)} \tag{2.52}$$

$$\Delta p = \mu \int_0^L \frac{u\,(x)}{K} \mathrm{d}x \tag{2.53}$$

$$\frac{\sigma_{\mathrm{YL}} \cos\theta}{4\mu} \int_0^{t_{\max}} \mathrm{d}t = \int_0^L r\,(l)^3 \left[\int_0^L \frac{1}{r\,(x)^{-4}} \mathrm{d}x \right] \mathrm{d}l \tag{2.54}$$

$$\frac{\sigma_{\mathrm{YL}} \cos\theta}{4\mu} t_{\max} = \langle r^{-4} \rangle \int_0^L r\,(l)^3\, l\ \mathrm{d}l \tag{2.55}$$

$$\int_0^L r\,(l)^3\, l\ \mathrm{d}l \approx \int_0^{m_{\mathrm{ru}} l_{\mathrm{ru}}} r\,(l)^3\, l\ \mathrm{d}l = \sum_{i=1}^{m} \int_{(i-1) l_{\mathrm{ru}}}^{i l_{\mathrm{ru}}} r\,(l)^3\, l\ \mathrm{d}l \tag{2.56}$$

$$\frac{\sigma_{\mathrm{YL}} \cos\theta t_{\max}}{4\mu} \approx \langle r^{-4} \rangle \langle r^3 \rangle \frac{L^2}{2} \tag{2.57}$$

$$r_{\mathrm{eq}} \equiv \frac{2L^2\mu}{\sigma_{\mathrm{YL}} \cos\theta t_{\max}} \approx \frac{1}{\langle r^{-4} \rangle \langle r^3 \rangle} \tag{2.58}$$

A connection to a uniform tube is established via an apparent pore radius, enabling the introduction of a singular geometrical factor Ω for conversion to the mean hydraulic radius $\langle r_{\mathrm{h}} \rangle$ (Eq. 2.59). From the probability moment equation (Eq. 2.50), which ranges over the length of the imbibition path L, it is evident that Ω is directly relatable to a tortuosity as defined by *Darcy* (compare Eq. 2.33) and therefore also to the one defined based on streamlines. The *constriction model* remains independent of the concept of tortuosity itself but the geometrical correction factor links to the commonly applied modifications of the *Lucas-Washburn* law, accommodating discrepancies such as high tortuosities or seemingly small apparent radii [91].

$$r_{\mathrm{app}} = \frac{\langle r_{\mathrm{h}} \rangle}{\Omega} = \frac{\langle r_{\mathrm{h}} \rangle}{\tau_{\mathrm{s}}^2} \tag{2.59}$$

When periodic alternation occurs between a small and large representative radius, the probability moment is represented by $\langle r^m \rangle = \left(r_{\min}^m + r_{\max}^m\right)/2$. This alters the equation for the equivalent capillary radius, as shown in Eq. 2.58, progressing into Eq. 2.60. It is posited that the periodically constricted tube results in an equivalent radius lesser than that of a uniform cylinder with radius $r_{\min}$. Approximating $r_{\max}/r_{\min} \gg 1$ in Eq. 2.60 identifies a common pattern as observed experimentally within various porous media characterized by a constricted pore geometry, as expressed in Eq. 2.61.[86, 92] The model excels in providing comparability between $r_{\min}$ and $r_{\max}$ with actual structural appearances across different assessment techniques. This is similarly applicable for techniques that acquire pore size distributions, where Eq. 2.58 bridges this gap. Although tortuosities from disparate methodologies lack direct relation to a fluid model, the geometric constriction model conveys a more consistent relation through statistical minimum and maximum radii.

$$\frac{r_{\mathrm{eq}}}{r_{\mathrm{min}}} = \frac{4}{\left(\frac{r_{\mathrm{min}}}{r_{\mathrm{max}}}\right)^4 + \left(\frac{r_{\mathrm{max}}}{r_{\mathrm{min}}}\right)^3 + \frac{r_{\mathrm{min}}}{r_{\mathrm{max}}} + 1} \tag{2.60}$$

$$\frac{r_{\mathrm{app}}}{r_{\mathrm{min}}} \approx 4\left(\frac{r_{\mathrm{min}}}{r_{\mathrm{max}}}\right)^3 \tag{2.61}$$

Additionally, a slip length b can be incorporated into the constriction model by defining $\alpha = [(r_{\mathrm{max}}/r_{\mathrm{min}}) - \beta] / (1 - \beta)$ and $\beta = b/r_{\mathrm{min}}$ (Eq. 2.62).[33] This allows the accommodation of higher liquid viscosity proximal to pore walls by simulating it as an immobile layer. Such findings align with observations for simple liquids.[81, 93, 94] Here, the geometrical interpretation of constrictions instead of tortuosity explains a much stronger effect of such a layer.

$$\frac{r_{\mathrm{app}}}{r_{\mathrm{min}}} = \frac{4(1-\beta)}{\alpha^{-4} + \alpha^3 + \alpha^{-1} + 1} \tag{2.62}$$

2.4 Solid Gas Interaction and Transport

2.4.1 Gas Transport

Gas or vapor transport involves a highly intricate phenomenon. The *kinetic theory of gases* provides a quantitative framework by considering the statistical motion of numerous molecules. In this theory, molecules behave as hard spheres, small compared to the mean distance between them, undergoing short, elastic collisions. Within a large volume where wall collisions are infrequent, diffusive transport is primarily dictated by inter-molecular collisions. The mean velocity $\langle v \rangle$ (Eq. 2.63) is derived from the *Maxwell distribution*. Here R is the ideal gas constant, T the temperature and M the molecular mass.[53, 95]

$$\langle v \rangle = \sqrt{\frac{8\mathrm{R}T}{\pi \mathrm{M}}} \tag{2.63}$$

The mean free path $\langle s \rangle$ (Eq. 2.64) between collisions can be expressed by the mean velocity and the impact frequency $z = \sqrt{2}\langle v \rangle \pi d^2 N/V$, where πd^2 is the collision cross section and N/V the number density of molecules. For an ideal gas, the number density can be substituted by $p/\mathrm{k_B}T$. The mean velocity and mean free path determine the diffusion constant D for a gradient of chemical potential, often manifested in a gradient of concentration c (Eq. 2.65). The molecule flux J is given by *Fick's first law* (Eq. 2.66).

$$\langle s \rangle = \frac{\langle v \rangle}{z} = \frac{V}{\sqrt{2}\pi d^{\,2} N} \tag{2.64}$$

$$\mathrm{D} = \frac{1}{3}\langle v \rangle \langle s \rangle \tag{2.65}$$

$$J = \mathrm{D}\nabla c \tag{2.66}$$

Under pore space confinement, the frequency of collisions with pore walls surpasses that of molecular interactions. This scenario is characterized by *Knudsen diffusion* (Eq. 2.67), occurring at high *Knudsen* numbers Kn (Eq. 2.68) e.g. for mesopores ($2 - 50\,\mathrm{nm}$).[96]

$$\mathrm{D_{Kn}} = \frac{2r_{\mathrm{pore}}}{3}\sqrt{\frac{8\mathrm{R}T}{\pi \mathrm{M}}} \tag{2.67}$$

$$\mathrm{Kn} = \frac{\langle s \rangle}{r_{\mathrm{pore}}} \tag{2.68}$$

2.4.2 Gas Physisorption

The isothermal physisorption of gases stands as a well-established technique for assessing porous materials. In this context, gas molecules are weakly attracted to the solid medium's surface via *Van-Der-Waals* forces, without forming chemical bonds. The adsorption enthalpy, indicative of released energy during gas molecule attachment, is relatively low at approximately $20\,\mathrm{kJ/mol}$. Physisorption isotherms are carried out in small increments of pressure increase. At each step the amount of adsorbed material is measured once an equilibrium is established. The duration required to reach equilibrium is termed *relaxation time* contingent on gas transport processes and step size. Common methods to quantify adsorbed material include volumetric, gravimetric, or optical isotherms.

Often noble gases, e.g. nitrogen or helium, are used since their intermolecular interaction is closest to an ideal gas. This characteristic is favorable during adsorption, as the gas energetically favors occupying free surface spaces and adheres in layers rather than forming clusters during multilayer adsorption. This layering propensity facilitates surface area calculation of the material. At high relative pressures and sufficiently small pores or cavities, capillary condensation occurs, forming liquid bridges between opposing pore walls with two concave menisci. This phenomenon

is described by the *Kelvin*-equation (Eq. 2.69), where V_m is the molar volume and r_K is the *Kelvin*-radius. It is the fluid-wall interaction and curvature of the liquid meniscus that are reducing the chemical potential, which is the origin of capillary condensation. At the wall the adsorption of three to four molecular layers can be expected until the chemical potential decreases to zero.[97] These preadsorbed layers of thickness d_{pa} before capillary condensation make out the difference between geometrical and *Kelvin*-radius via $r = r_K + d_{pa}$.

$$r_K = \frac{-2\sigma_{lv} V_m}{RTln(\frac{p}{p_0})} \tag{2.69}$$

3 Photonic Crystal: Dynamics of Oligostyrenes

Advanced imaging techniques enable the ex situ resolution of single pore capillary filling in polymers by utilizing melt freezing (appendix D). This freezing method is similarly applied in the synthesis of nanotubes through molding processes.[14] These nanotubes originate from a molecularly thin layer, known as a precursor film, which spreads along the pore wall at a faster rate than the main liquid meniscus. The following discussion introduces an enhanced approach to in situ investigation of capillary filling and the rapid precursor film within nanoporous scaffold materials. It combines in situ thin film analysis with photonic crystal light spectroscopy, achieving high precision in monitoring both simultaneously. This interferometric technique offers sub-nanometer accuracy with time resolution down to microseconds. The technique's foundation is a mesoporous silicon (PSi) chip-like reflective sensor (CLRS), which is introduced in subsection 2.2.4, comprising a micrometer-thick thin film followed by a photonic crystal. This assembly is interfaced with a white light spectrometer under normal incidence and reflection conditions. The previously published study [33] is extended herein with additional datasets and further refined analysis, particularly in relation to the FFT.

3.1 Experimental Procedure

The experimental setup includes a reflection probe equipped with a glass fiber bundle, comprising two read fibers surrounded by 17 illumination fibers. The light source, AVALIGHT-DH-S-BAL, covers a spectral range of $215-2500\,\mathrm{nm}$ through a combination of deuterium and halogen sources. Prominent peaks within the spectrum of the halogen source ($>500\,\mathrm{nm}$) are mitigated by a built-in filter, permitting extended integration times for the detectors without causing over saturation at specific spectral points. During measurements, the deuterium source is deactivated to prevent material degradation from ultraviolet exposure. Two spectrometers are individually connected to each read fiber. A UV-VIS spectrometer (AvaSpec-2048CL) with a $10\,\mu\mathrm{m}$ slit provides a spectral range of $200-1100\,\mathrm{nm}$ and an average spectral resolution of $1\,\mathrm{nm}$. It is complimented by an near infrared spectrometer (AVASPEC-NIR512) equiped with $25\,\mu\mathrm{m}$ slit, having a spectral range of $850-1650\,\mathrm{nm}$ with an average spectral resolution of $4\,\mathrm{nm}$. Both spectrometers support

a store-to-RAM mode, utilized for continuous measurements at integration times below 15 ms. At higher integration times (>15 ms), the spectrometers synchronize via a coaxial cable, whereas such synchronization is not attainable at lower times. The minimum integration time achievable for both devices is 20 µs, with overall continuous measuring duration restricted by RAM storage capacity for approximately 16,000 measurements.

The liquids examined are mono disperse oligostyrenes (OS) (from Polymer Standards Service) with two (OS-2) and five (OS-5) monomer repetition units. These are synthesized by anionic polymerization, resulting in a polydispersity of one for the dimer and close to one for the pentamere. Both have a sec-butyl and proton end group. Molecular weight remains below the critical threshold for entanglements ($M_c \approx 35,000$ g/mol [98]). The viscosity is measured by a rheometer (Kinexus Prime Series) in plate to plate geometry at room temperature. Resulting in a viscosity of $34,000 \pm 570$ mPa s under a shear rate of $0.01 - 100$ Hz and 9.4 ± 2.1mPa s at $100 - 51600$ Hz for OS-5 and OS-2 respectively. Both liquids show Newtonian fluid behavior within the shear-rate range.

The porous silicon (PSi) samples undergo electrochemical etching to vary the thicknesses of homogeneous layers preceding the 1-D photonic crystal. Figure 2.10 illustrates the samples, fabricated from monocrystalline boron-doped (p-type) silicon wafers, possessing a resistivity between $1-4$ mΩcm and are cut in 100-orientation. Electrochemical anodization is conducted with a HF(50 w%):EtOH 1:2 volumetric solution in a polytetrafluoroethylene cell with a round 78.74 mm^2 window towards the wafer and a platinum counter electrode. The homogeneous layer is etched under constant current application of 10 mA, adjusting the application time for thicknesses from $3 - 15$ µm. The 1-D photonic crystal, a layered construct exhibiting variable porosities, results from current density variation, with etching time adjusted to produce layers of uniform optical thickness, equivalent to 1/4 the resonant wavelength λ_{PC} of the desired resonance position of 750 nm. For the central cavity of the PC a thickness according to $\lambda_{PC}/2$ is used. Current sequences in mA are as follows: 60 $\lceil 10\ 40 \rceil_8$ 40 $\lceil 10\ 40 \rceil_8$. Each current's application time is determined from a reference synthesis (Tab. 3.1). References undergo etching for a specific duration, $5 \cdot 681.3846$ s divided by the respective current. The etching time is subdivided in equal pulses with a maximum application duration based on the pure time divided by 50/current. In between, the current is held at zero for 2 s. Further details can be found in [31]. The samples were synthesized by Dr. Raul Urteaga (Consejo Nacional de Investigaciones Científicas y Técnicas).

For imbibition experiments, the oligomers were deposited onto a glass object carrier and positioned in front of the glass fiber reflection probe. Prior to each experiment, PSi samples are cleansed with toluene and dried. In accordance with the difference in viscosity, the sampling rate of the spectrometers is chosen to 500 ms and $1-5$ ms for OS-5 and OS-2, respectively. Spectroscopy measurements commence

Table 3.1: Currents applied for etching of 1-D photonic crystal interference structures in mesoporous silicon. The reference thickness and porosity are the result of the defined current application time in the etching of reference samples for each current.

current [mA]	reference thickness [nm]	porosity [%]
10	3121	55.5
40	2453	69.0
60	2330	75.5

prior to the oligomer film's direct contact with the sample, which initiates capillary rise.

3.2 Analysis of Fluid Dynamics

3.2.1 Spectra Analysis

The capillary-driven imbibition of oligomer melts into mesoporous silicon (PSi) samples, consisting of a homogeneous layer followed by a 1-D photonic crystal, results in a proportional increase of the effective refractive index n_{eff} regarding the infiltrated volume fraction. Utilizing white light spectroscopy, changes in effective optical thickness (EOT) e_{ot} are analyzed using the equation $e_{\text{ot}} = 2d{\cdot}n_{\text{eff}}$, where d represents the physical thickness. This analysis is performed through thin-film interference patterns and the band gap position λ_{PC} of the photonic crystal. Samples are engineered with λ_{PC} prevailing in the wavelength range of $600 - 1000\,\text{nm}$, while thin-film interference is dominant from $1000 - 1650\,\text{nm}$. This setup allows for the extraction of local filling dynamics at the photonic crystal's center and global ones from interference patterns. The EOT $\Delta e_{\text{ot}}(t)$ (Eq. 3.1) measured is normalized by initial t_0 and final t_{end} filling times, directly correlating to the volumetric filling fraction.

$$\Delta e_{\text{ot}}(t) = \frac{e_{\text{ot}}(t) - e_{\text{ot}}(t_0)}{e_{\text{ot}}(t_{\text{end}}) - e_{\text{ot}}(t_0)} \tag{3.1}$$

Different methods are used to analyze the EOT of measured spectra in the NIR region within this thesis. In a simple but not always applicable approach, a single peak from the interference pattern in the direct spectrum is directly fit by a *gaussian* and observed as it shifts to higher wavelengths, as shown in Fig. 3.1 for OS-5 imbibition. It is recommended to track fringes at higher wavelengths due to the dominance of PSi thin film reflection. The respective wavelength position is then normalized by its initial and final values. The filling of the PC is assessed

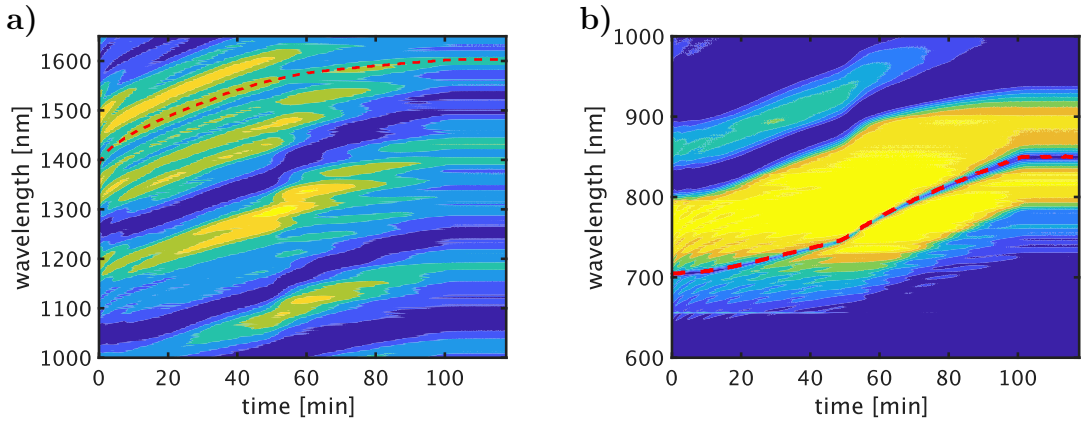

Figure 3.1: Imbibition of OS-5 in the sample b from Tab. 3.2. a) NIR spectrum, the dashed line indicates an analysis of the dynamics by fitting an interference fringe. b) PC infiltration, the resonance position is determined by a *Gaussian* fit.

by following its resonance wavelength in the visible spectrum.[31] Therefore, the intensity of the spectrum is inverted and a *Gauss* fit is applied for the region of the initial band width of the PC. The subsequent resonance positions are determined by a Gaussian in the respective prior window. This resonance position is sensitive to the optical thickness of its central defect layer.

A FFT is superior in disentangling the interference pattern from a stack of layers. To reduce the noise in the FFT, zero padding is applied. Additionally, Hann-windowing is used to reduce spectral leakage and thereby side lobes i.e. smaller artificial peaks next to a real peak. Analyzed is the absolute of the FFT with the magnitude squared, which is called power spectrum. This improves the detection of peaks.
The samples' stacked structure results in three significant peaks, representing the optical thickness of the PC, the homogeneous layer, and their combined stack. Fig. 3.3 demonstrates the *reflectometric interference Fourier transform spectroscopy* (RIFTS) analysis for OS-5 imbibition across three main samples. Higher integration times for OS-5, compared to OS-2, yield an improved signal-to-noise ratio (SNR). In the direct spectrum (Fig. 3.3 a), a complex superposition of sinusoidal functions is observed. Overall the reflected intensity decreases during the infiltration, but the spectrum is normalized for each time position to improve readability. The intensity decrease can be attributed to a loss of refractive index contrast between porous layer and bulk silicon. In the FFTs b)-d) the two most prominent peaks are directly apparent and can be found by using a peak finding algorithm and sorting by height. The one between 10 and 15 µm is identified as the PC and the one at much higher OT as the overall stack. Less clear is the identification of the homogeneous layer. Here the orthogonal Maxwell Garnett equation (Eq. 3.2 [65]) provides helpful guidance.

$$n_{1/2}^2 = \frac{\Phi_i \left(n_{1/2}^2 \frac{2n_{\mathrm{Si}}^2}{n_{1/2}^2 + n_{\mathrm{Si}}^2} - n_{\mathrm{Si}}^2 \right) + n_{\mathrm{Si}}^2}{\Phi_i \left(\frac{2n_{\mathrm{Si}}^2}{n_{1/2}^2 + n_{\mathrm{Si}}^2} - 1 \right) + 1} \tag{3.2}$$

Comparing the initial air filled state with the final oligomer filled one, the porosity and thickness can be calculated in conjunction with $e_{\mathrm{ot}} = 2d \cdot n_{\mathrm{eff}}$ using the MATLAB *solve* function. Φ_{i} is the average porosity of the i-th layer, $n_{1/2}$ is the refractive index of the medium filling the pore space and n_{Si} the one of silicon. Subsequently, the equation $d_{\mathrm{stack}}\Phi_{\mathrm{stack}} = d_{\mathrm{film}}\Phi_{\mathrm{film}} + d_{\mathrm{PC}}\Phi_{\mathrm{PC}}$ is used to find the peak of the homogeneous layer. In c) and d) their position is magnified.
An often more prominent peak, that should not be confused with the homogeneous layer, appears directly adjacent to the one of the overall stack. On some occurrences it just appears as a shoulder of the overall stack peak. It cannot be clearly attributed, but it is assumed to be the stack of homogeneous layer and the first half of the PC. Because of the windowing function and the missing symmetric lobe on the other side of the overall stack peak, it is not considered a side lobe. The peak shows a weakness of the FFT method in combination with the complex structure of the material. If the optical thickness of layers is too close they cannot be differentiated. This can especially occur during dynamic changes of the optical thickness in capillary imbibition experiments.

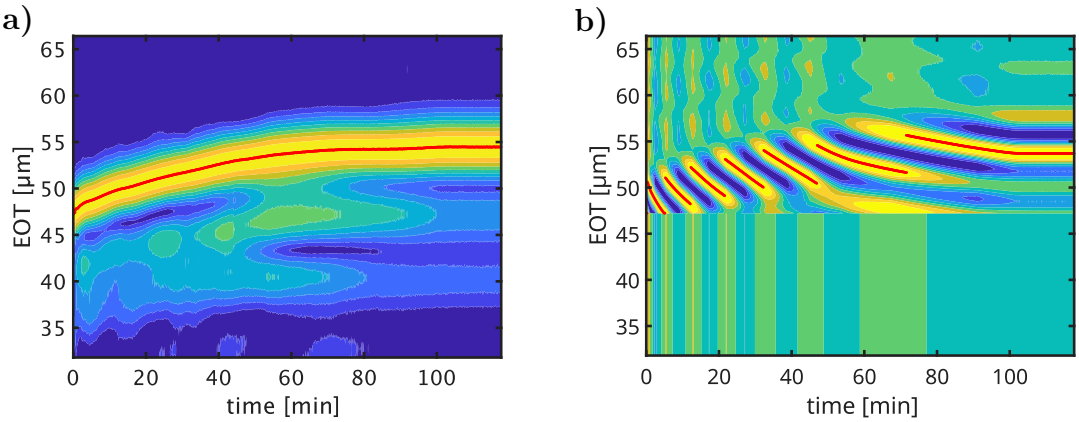

Figure 3.2: FFT of the NIR spectra during OS-5 imbibition in the sample (refer to Tab. 3.2 b). a) Absolute FFT. b) Imaginary part of the FFT.

Despite this issue, capillary imbibition dynamics can be analyzed by the EOT of the overall stack over time (Fig. 3.2). For a single layer the center of gravity provides best peak determination for the EOT (subsection 4.2.2). In the case here of numerous layers with similar EOT a peak height detection is found to be more robust, but the resulting filling fraction over time shows broad bumps. These are potentially due to an overlapping of peaks, or due to phase steps or

Table 3.2: The thickness d_{oMG} and porosity Φ_{oMG} by orthogonal MG using the RIFTS method[11] correspond to the measurement displayed in Fig. 3.3.

	layer	d_{SEM} [µm]	d_{oMG} [µm]	Φ_{oMG} [%]
	PC	3.5	3.5	77
b)	thin film	9.3	8.3	53
	stack	12.7	11.7	59
	PC	3.4	3.3	78
c)	thin film	14.0	10.7	55
	stack	17.2	14.0	59
	PC	2.7	3.2	73
d)	thin film	5.1	5.7	63
	stack	7.9	8.8	64

Table 3.3: Literature values used in the calculations. The refractive indices are the mean between $1150 - 1650$ nm.

σ[99] [mJ/m^2]	$\cos(\theta)$[100]	n_{Si} [68]	n_{air} [101]	n_{OS}[102]
40.7	1	3.51	1	1.57

the effect of concurrent phase and frequency change of the sinusoids in the direct spectrum. Evaluating solely phase shifts, using the FFT's imaginary component, offers dynamic assessment with minimal noise. The phase jumps are identified by numerical differentiation and are corrected by back oriented numerical differences. A detailed description of this method is given in chapter 4. The first mentioned peak fitting method in the direct spectrum is found to be in good agreement with the latter method.

3.2.2 Constriction Model

The measurement method of white light spectroscopy on porous silicon *Fabry-Perót* structures and a photonic crystal allows the distinction of the imbibition dynamics into global and local filling. This analysis draws upon previous studies.[31, 33] Initially, imbibition dynamics of the thin film are examined using the constriction model, which offers an alternative interpretation of tortuosity, modifying the *Lucas-Washburn* equation (Eq. 3.3). In this context, tortuosity is viewed not as a meandering path but as a geometric factor Ω, reflecting the impact of numerous constrictions. It is sensitive to synthesis methodology but exhibits high reproducibility under consistent synthesis conditions, as addressed in chapter 4 regarding the *inverse problem of capillary filling*. Previously, a tortuosity literature value of 2.6 with a hydraulic radius of 5.8 nm based on glycol imbibition was used for PSi by this synthesis.[54] These values stem from SEM surface recordings and image analysis, which are challenging at this scale due to angles and gray scale

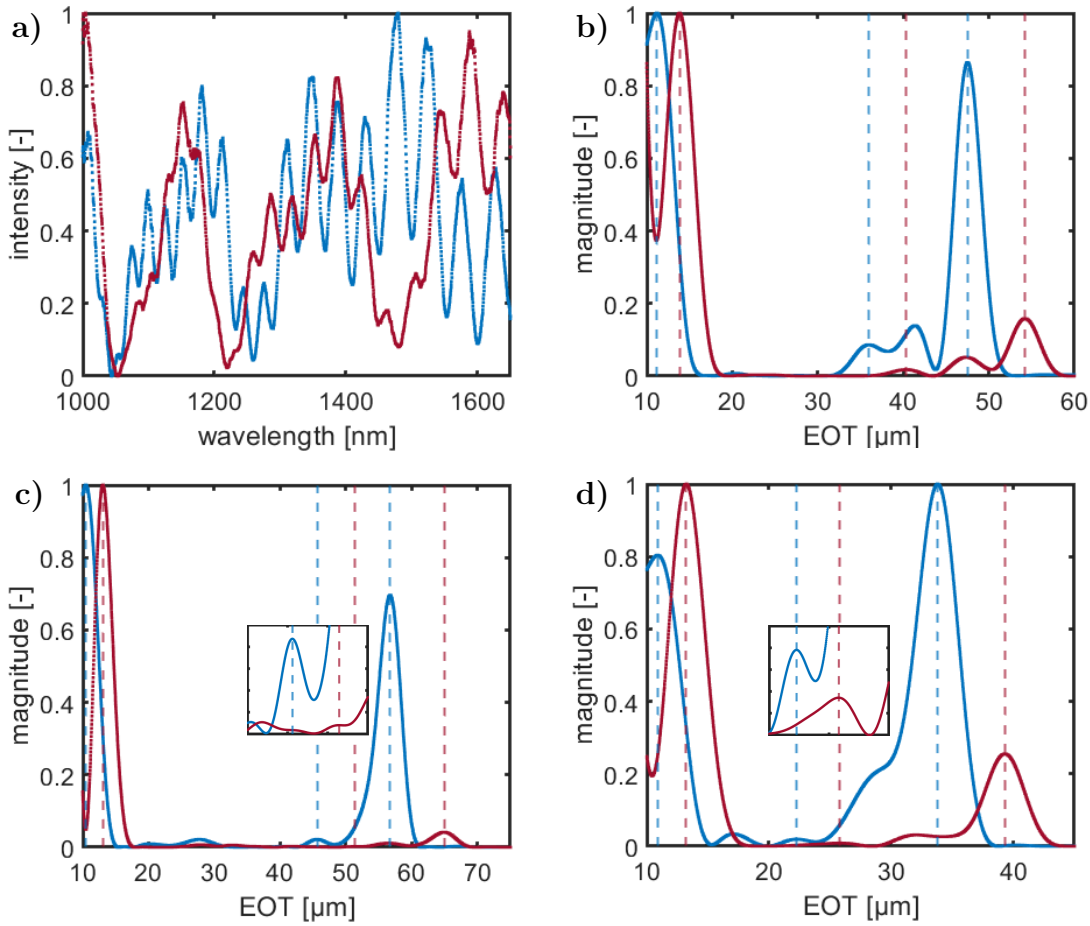

Figure 3.3: RIFTS analysis of the samples in Tab. 3.2. Blue curves depict air-filled states, while red ones show OS-5 filled states. Insets enlarge peaks correlating with the thin film. a) is the direct spectrum of b). c) and d) refer to the samples with the respective name in Tab. 3.2.

thresholds. Additionally, the surface layer of porous silicon often exhibits a higher pore size than the bulk of the material.[11] Here instead, a tortuosity of 2.3 and a hydraulic radius of 4 nm are taken from the analysis in subsection 4.2.3.
Inserting $\langle r^m \rangle = (r_{\min}^m + r_{\max}^m)/2$ in Eq. 3.4 and the equivalent radius of the constriction model for the effective radius in Eq. 3.5, Eq 3.6 is obtained. Here $\alpha_0 = r_{\max}/r_{\min}$ simplifies the expression, to calculate explicit values from the reference for the constriction model. The tortuosity of 2.3 relates to an α_0 of 2.26. This value is used in Eq. 3.7 to calculate $r_{\min} = 2.46\,\text{nm}$ and $r_{\max} = 5.55\,\text{nm}$.

$$L(t) = \sqrt{\frac{\langle r_\text{h} \rangle}{\tau_\text{s}^2}} \sqrt{\frac{\sigma_\text{lv} \cos\theta_\text{e}}{2\mu}} \sqrt{t} \tag{3.3}$$

$$r_{\mathrm{eq}} \approx \frac{1}{\langle r^{-4}\rangle \langle r^{3}\rangle} \tag{3.4}$$

$$r_{\mathrm{app}} = \frac{\langle r_{\mathrm{h}}\rangle}{\Omega} = \frac{\langle r_{\mathrm{h}}\rangle}{\tau_{\mathrm{s}}^{2}} \tag{3.5}$$

$$\tau_{\mathrm{s}}^{2} = \Omega = \frac{(1+\alpha_0)(1+\alpha_0^{-4})(1+\alpha_0^{3})}{8} \tag{3.6}$$

$$\langle r_{\mathrm{h}}\rangle = \frac{r_{\mathrm{min}} + r_{\mathrm{max}}}{2} = \frac{r_{\mathrm{min}}(1+\alpha_0)}{2} = \frac{r_{\mathrm{max}}(1+\frac{1}{\alpha_0})}{2} \tag{3.7}$$

The radius of a rigid scaffold appears largely unaffected by the liquid type. However, fitting imbibition curves for different liquids in identical samples using the classical *Lucas-Washburn* law yielded varying effective radii. Thus r_{app} from this equation is an apparent radius for fluid dynamics. Conclusively, the geometrical correction factor cannot explain the dynamics alone. A slip length b has to be considered to account for the fluid molecule layers close to the pore wall. As discussed in the theory (subsection 2.3.4) b is treated here as the thickness of an immobile layer at the pore wall that diminishes the hydraulic radius. The extend of this layer in a certain scaffold material can be viewed as a fluid specific property. Eq. 3.8 with $\alpha = [(r_{\mathrm{max}}/r_{\mathrm{min}}) - \beta]/(1-\beta)$ and $\beta = b/r_{\mathrm{min}}$ explains the different effective radii in the framework of the constriction model. This model is developed in major parts by Claudio L.A. Berli (INTEC (Universidad Nacional del Litoral-CONICET), Argentina).[33]
In Fig. 3.4 the results of the imbibition dynamics are presented. The normalization of time to the respective moment of complete infiltration allows the comparison of the characteristics of the two oligomers, although OS5 is in the order of hours and OS2 of milliseconds. The end of the thin film dynamics is around a filling fraction of 0.8 determined by double logarithmic plotting. Simultaneous evaluation of the OS-2 and OS-5 dynamics in the thin film by the constriction model (Eq. 3.8), based on the apparent radius, reference tortuosity and bulk fluid parameters, agrees well with the measurements. The apparent radius is determined by a fit with the classical *Lucas-Washburn* equation i.e. Eq. 3.3 with a tortuosity of 1. The results of the fitting are summarized in Tab. 3.4. Notably, the square root fit parameters are bigger for the sample with a thin film of 13 µm and therefore also the apparent pore radii, but the immobile layers appear smaller. This suggests a higher actual pore radius than the other samples. Indeed if a pore radius of 5 nm is assumed instead of 4 nm all of the parameters fit close to the other samples.
The immobile layer thicknesses align with molecular dimensions. For OS-2 and OS-5 a respective size of $0.9 - 1.2$ nm and $1.4 - 1.8$ nm is estimated by a quantum

mechanics based molecule calculator.[103] Despite the dimensional agreement, these values represent a semi-quantitative trend of increasing immobile layer thickness with molecular dimensions. In reality the immobile layer has a complex composition including adsorbed trains, loops and tails of the molecules, discernible via in-situ nanodielectric spectroscopy.[104] The physical impact of a strongly adsorbed layer potentially extends beyond a monolayer. Multilayers with increased effective viscosity could enhance the apparent extent of the immobile layer, as found in the case of water.[79] For the molecules in question, steric hindrance is presumably more relevant.

$$\frac{r_{\mathrm{app}}}{r_{\mathrm{min}}} = \frac{4(1-\beta)}{\alpha^{-4}+\alpha^{3}+\alpha^{-1}+1} \tag{3.8}$$

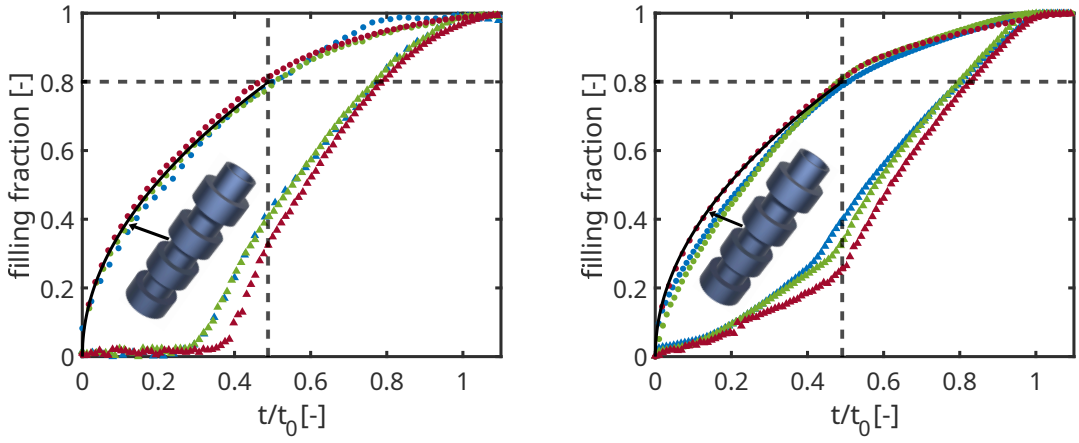

Figure 3.4: Overall infiltration dynamics of OS-2 (left) and OS-5 (right). The final imbibition time t_0 for each individual measurement can be calculated from Tab. 3.4 in conjunction with the equation $t_0 = d_{\mathrm{oMG}}^2/a^2$. Dots indicate thin film interference, reflecting overall filling, while triangles depict local filling based on photonic crystal resonance shift. Identical colors represent identical sample measurements. Blue corresponds to a homogeneous porous layer of 5 µm, green 8 µm and red 13 µm in front of the photonic crystal. The solid black line is the calculated constriction model for the filling of the homogeneous porous layer.

3.2.3 Fluid Front

A prominent difference in the measured dynamics relates to the filling of the photonic crystal (Fig. 3.4). For OS-2, the resonance shift attributed to liquid infiltration is delayed, whereas for OS-5, it initiates earlier relative to overall filling. This phenomenon is scrutinized subsequently.

Table 3.4: Results: The decelerated dynamics in capillary filling of the homogeneous porous layer with thickness d_{oMG} can be illustrated by the apparent radius r_{app}. In the constriction model the different capillary imbibition dynamics of the oligomers are explained by the immobile layer thickness b. The squared fit parameter a of the main meniscus can be compared to the diffusion-like coefficient D_{PF} of the precursor film spreading. Additionally, a thickness d_{PF} for the precursor film is derived.

	d_{oMG} [µm]	r_{app} [nm]	b [nm]	a^2 [m^2/s]	D_{PF} [m^2/s]	d_{PF} [nm]
OS-2	5	0.07	1.38	$1.57{\cdot}10^{-10}$	-	-
OS-5	5	0.04	1.59	$2.91{\cdot}10^{-14}$	$3.3{\cdot}10^{-12}$	0.50
OS-2	8	0.08	1.37	$1.66{\cdot}10^{-10}$	-	-
OS-5	8	0.05	1.52	$3.97{\cdot}10^{-14}$	$4.7{\cdot}10^{-12}$	0.52
OS-2	13	0.18	1.00	$4.00{\cdot}10^{-10}$	-	-
OS-5	13	0.11	1.23	$6.55{\cdot}10^{-14}$	$6.4{\cdot}10^{-12}$	0.53

By employing spatio-temporal re-scaling of PC filling dynamics using $\mathrm{x}_0/(\mathrm{a}\sqrt{\mathrm{t}})$ the fluid front shape is obtained (Fig. 3.5), where x_0 is the distance from the samples surface to the center of the PC and a is the measured coefficient for capillary imbibition in the preceding homogeneous layer. x_0 is determined by the time, where the filling fraction is converging to one and adjusted for the abscissa position of one. The abscissa is limited to a value of 6 to enhance readability, as the course remains constant beyond this point. For each oligomer consistent shapes are obtained. OS-5 shows a flat fluid front, whereas OS-2 has a broad onset region. Start and end of the latter are determined by interceptions of tangents (Fig. 3.5 right). The onset x_{PF} is in the region of 4.7 of the abscissa. For the thickest sample c) in Tab. 3.2 the onset is already at 4.2, but this fits the previous observation that this particular sample has a higher pore diameter. Samples b) and d) are in very good agreement. Overall trends remain independent of the homogeneous layer's thickness. For the OS-5 measurements a diffusion like coefficient D_{PF} for the precursor film spreading can be derived by $D_{\mathrm{PF}} = (\tau\ a\ x_{\mathrm{PF}})^2$ (Tab.3.4). The precursor film follows a faster $\sqrt{\mathrm{t}}$-law than the main meniscus, as can be seen by comparing the squared pre-factor of the capillary imbibition. This in agreement with molecular dynamics simulations on nanopores.[32] *Sukhishvili* et al. found a proportionality of $D \sim N^{-3/2}$, where N is the degree of polymerization. In conclusion D_{PF} for the oligomers can be expected to be at the same order of magnitude.[105]
The end of the precursor film region is determined by deviation from a linear fit of the meniscus region by more than the standard deviation in 10 consecutive points. A simple tube model is used for an approximation of the precursor thickness by $\Phi_{\mathrm{PF}} = \frac{2\langle r_{\mathrm{h}}\rangle d_{\mathrm{PF}} - d_{\mathrm{PF}}^2}{\langle r_{\mathrm{h}}\rangle^2}$, resulting to $d_{\mathrm{PF}} \approx 0.5\ nm$.

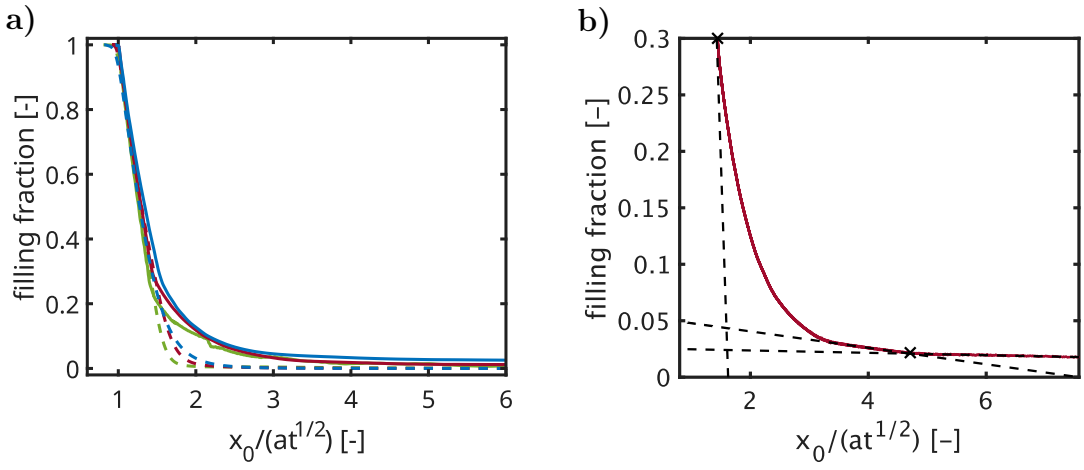

Figure 3.5: Fluid front shapes by re-scaling of the dynamics at the PC by the pre-factor of the square root of time fit of the dynamics in the homogeneous layer. a) Dashed lines correspond to OS-2 and continuous lines to OS-5. b) Displays the tangent method to determine the precursor film region.

3.2.4 Conclusion

The method presented offers a novel platform utilizing porous silicon to study polymeric fluids with sub-nanometer resolution and variable time resolution, ranging from microseconds to indefinite longer durations.[31, 33]
Recent molecular dynamics simulations have identified a deceleration in capillary imbibition for polymeric liquids with low polymerization degrees even in weak nanopore confinements.[34] This anomalously slow transport is attributed here to a bottle neck structure and an additional contribution by a liquid-wall interaction depending on the molecule. The latter is quantified by an immobile layer adhering to the pore wall. This layer is smaller for the styrene dimer than the pentamer.
Previously, the anomalously slow capillary filling of PSi is reported in conjuction with a high streamline tortuosity (2.6) for its degree of anisotropy.[54] In this thesis it is explained by the high impact of local undulations at the given pore size. This is modeled by a *constriction model*, based on bulk fluid parameters, tortuosity, and apparent pore size derived from the Lucas-Washburn equation. A reference tortuosity of 2.3 from 2-propanol imbibitions in chapter 4 serves as the basis. Ideally, a liquid with perfect wall-slip behavior would be optimal, yet the complexity of this subject extends beyond the thesis scope. Based on the reference, where the immobile layer $b \approx 0$, a *modified constriction model* with $b \neq 0$ is calculated to quantify the individual slip length of the dimer ($\langle b \rangle = 1.37\,\mathrm{nm}$) and pentamer ($\langle b \rangle = 1.55\,\mathrm{nm}$) by solving the model with the dynamics from both liquids simultaneously.
The novelty lies in the simultaneous recording of overall filling and local filling via *Fabry-Pérot* interference and photonic crystal resonance, respectively, enabling direct spatio-temporal re-scaling of the PC's filling dynamics. The rescaling reveals the fluid front shape with sub-nanometer resolution. For the pentamer, a precursor

film of approximately 0.5 nm with a diffusion like coefficient of $4{\cdot}10^{-12}\,\mathrm{m}^2/\mathrm{s}$ develops during the infiltration. The capillary filling transport coefficient of the pentamer is two orders slower, while that for the dimer is two orders higher than the diffusion-like coefficient, elucidating the discrepancy between precursor presence and absence.[33]

4 Mesoporous Silicon: Inverse Problem of Capillary Filling

In the following the pore structure of mesoporous silicon membranes is investigated by measuring the capillary filling of a volatile liquid. Liquid dynamics are recorded via in situ optical thin film spectroscopy. It involves the inversion of the common inquiry of throughput i.e. fluid flow, when geometry and pressure are known, to a scenario where throughput and pressure are known, while the geometry is determined. This scenario is termed the *inverse problem of capillary filling*. The solution involves the imbibition process initiated from one side of the membrane, followed by drying and subsequent imbibition from the opposite side.[39, 40] Consequently, it is limited to membranes, which provide a pore opening on both sides. In this study, the method is employed for a comparative analysis of synthesis routes for mesoporous silicon. This is the first time the *inverse problem of capillary filling* is applied for a mesoporous material. Attempts of the technique are documented in [106], where the superiority of spectroscopy over laser interferometry is demonstrated.

4.1 Inverse Problem Experiments

Mesoporous silicon is electrochemically etched using p-type (boron doped), monocrystalline silicon wafers, oriented along the [100]-direction. This chapter examines varying synthesis conditions, including different doping levels, application of constant or pulsed current, and pre- as well as post-treatments identified in literature.[11] All samples are produced in a PTFE-batch reactor with a platinum counter electrode, and wafers are fully contacted on the unpolished backside by aluminum foil, while the polished topside faces the reaction chamber. It is to noteworthy that the etching procedures differ dpending on the doping level of the silicon wafer. The produced membranes are in a thickness range of $45 - 65\,\mu m$.

p^{++}-wafers (SIL'TRONIX) with resistivity between $0.6-1\,m\Omega cm$ are first cleaned for 10 min in an ultrasonic bath using 2-propanole. The etching is performed in a PTFE-cell, using an O-ring, which exposes a circular area $2.27\,cm^2$ of the wafer to etching. The etching procedure is taken from [11]. Initially, samples undergo a pretreatment anodization at $200\,mA/cm^2$ with a 3/1 volumetric ratio of hydrofluoric acid (49 %) and ethanol (HF/EtOH). Following the etching solution disposal, the

chamber is rinsed three times with ethanol. Subsequently, a 1 mol/l aqueous NaOH solution with a 10 % volumetric addition of EtOH is allowed to take effect for 5 min. This step is succeeded by the main etching using a 7/3 HF/EtOH solution and a current density of 150 mA/cm^2. After 624 s of constant current application, the solution is exchanged and the current is started for another 624 s. Detachment of the porous section from the bulk wafer is achieved by employing a 1/29 HF/EtOH mixture with a current density of 6 mA/cm^2 for 240 s. This leads to the detachment of the membrane. The procedure concludes with three ethanol rinses.
The p^+-wafers (Si-Mat), exhibiting resistivity of $10 - 20\,m\Omega cm$, are also cleaned for 10 minutes in an ultrasonic bath with 2-propanol prior to processing. Here the electrochemical etching is conducted with a 2/3 volumetric HF/EtOH solution applying a current density of 12.5 mA/cm^2. Prior to the main etching the current is set to zero for 640 s. Main etching proceeds with either a constant current (galvanostatic) or in pulses alternating between 0 mA/cm^2 and 12.5 mA/cm^2 per second for different samples. Various recipes are used for detachment, broadly characterized by either low HF concentration with low current density or high HF concentration with high current density.[11]
Samples produced via pulsed etching are divided into multiple membrane fragments for analysis and post-treatment, which involves chemical oxidation with hydrogen peroxide (30 %) for 20 h, followed by a dip in 1/29, 2/3 or 1/1 ratio of HF/EtOH solution for 2 h.
Samples are designated based on their unique synthesis conditions. A "p^{++}-sample" refers to a sample produced by the technique for p^{++}-wafers. A "constant-sample" is synthesized galvanostatically from a p^+-wafer. Samples etched using a pulsing current pattern are termed "pulsed-samples," with post-treated fragments named after their specific HF/EtOH dipping ratios, such as "29/1-sample".

The basic characterization of porosity and thickness consists in weighting the samples on a microbalance, taking a photo at normal incidence of the membrane surface with millimeter paper as a reference and measuring the thickness with a touch probe or scanning electron microscopy. The volume of the sample is determined from the area in the photograph and the thickness. Thereby the porosity can be determined gravimetrically from the measured weight and literature density of 2.329 g/cm^3 [107]. Alternatively, the porosity is determined by a nitrogen isotherm using the *Barrett-Joyner-Halenda* method and the thickness by scanning electron microscopy.
Results are compared to the RIFTS method detailed in section 2.2 from $1000 - 1650$ nm wherein optical thickness is measured for completely air- and 2-propanol-filled states. Porosity and thickness are determined, solving the *orthogonal Maxwell-Garnett* effective medium model for both states simultaneously (see subsection 3.2.1). A reference of the reflection is measured on an equally doped bulk silicon wafer. Despite differing integration times due to stronger reflections, this reference effectively

normalizes the light source's spectral profile. Figure 4.1 illustrates the spectroscopy setup.

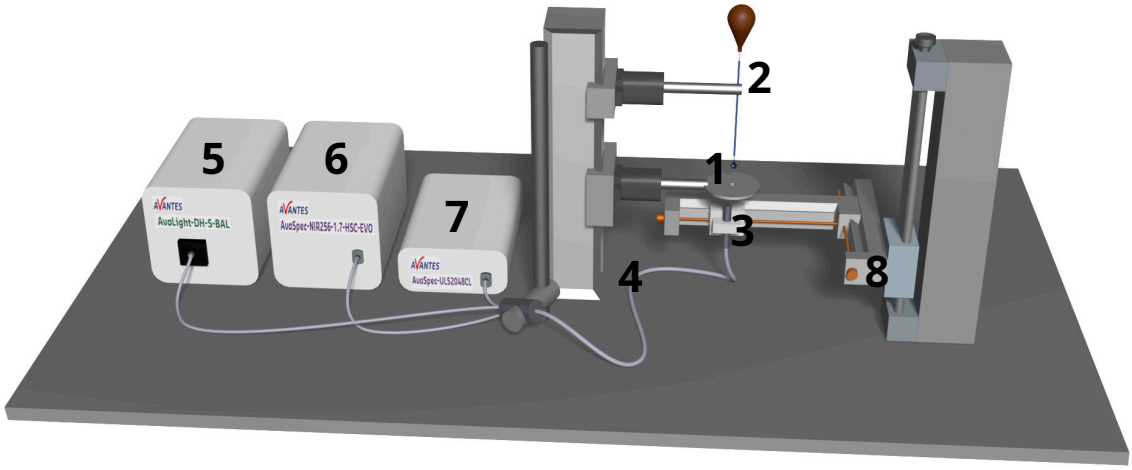

Figure 4.1: Thin film spectroscopy setup: 1) sample holder with fixed 180° rotation, 2) micro pipette, 3) reflection probe, 4) glass fiber, 5) light source, 6) NIR spectrometer, 7) UV-VIS spectrometer, 8) linear XYZ-stage.

For the inverse problem method, synthesis-grade 2-propanol is drop-cast onto the porous silicon samples. Capillary filling is recorded in-situ using near infrared reflection spectroscopy, as outlined in section 3.1. Due to the probing liquid's low viscosity but adequate detectability for the optical method, an integration time of 500 ms is chosen, enabled by direct internal RAM storage on the instrument. After the imbibition from one side samples are given time to dry. Then, the imbibition is initiated from the opposite side. The sample holder is designed to allow a rotation keeping the measuring spot in place.

4.2 Inverse Problem Solution: Porous Silicon

The solution to the *inverse problem of capillary filling* for porous silicon membranes, as determined through optical spectroscopy on imbibition dynamics, involves a structured approach encompassing three primary stages. Initially, the raw spectra are evaluated to assess changes in optical thickness throughout the process. This is succeeded by a numerical inversion and a solving algorithm. Finally, the results are evaluated by considering fluid dynamic models and structural features are compared to scanning electron microscopy images.

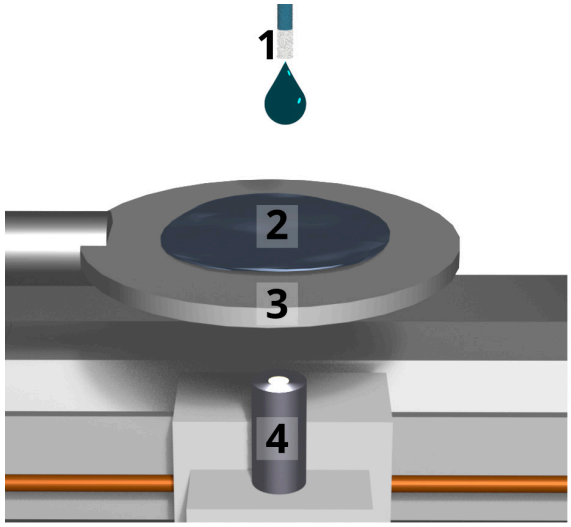

Figure 4.2: Zoom in on drop-cast for spectroscopy during capillary imbibition: 1) micro pipette with dispensed droplet, 2) PSi membrane (in reality held in position by a clamp) 3) sample holder with hole at the center , 4) reflection probe.

4.2.1 Spectra Analysis

The interference pattern of a porous silicon thin film is a sinusoidal function. Substitution of air by 2-propanol in the pore space of mesoporous silicon induces a phase shift and a frequency increase of the interference pattern according the change in optical thickness. There are several different analysis methods available to track this change of the optical thickness.[108] The precision of the *wavelet* transformation is counterbalanced by its extensive computational demands and the need for calibration of its arbitrary units. The classical FFT method of following a peaks center of gravity in the absolute of a FFT led to some artifacts due to simultaneous frequency and phase shift of the effective optical thickness (EOT) peak in frequency space. An example of the absolute FFT method (RIFTS) is displayed in Fig. 4.3. The bumps in the peak position (red curve) have a strong influence in the evaluation of the *inverse problem of capillary filling*. A third method is a simple fit, either using a sinusoidal function for the whole spectrum or a gaussian for a single peak. This tends to generate a noisy signal, adversely impacting subsequent physical analysis. None of these methods achieves a robust evaluation without additional refinement.
In this study, phase unwrapping is accomplished using the imaginary part of a Hann-windowed FFT. Fig. 4.4 presents the power spectrum of the imaginary part. Maximum peaks are identified at each time step within a predefined window surrounding the preceding peak position. The phase steps are pinpointed using first-order backward numerical differentiation to identify local maxima exceeding a threshold value. Corrections are applied by optimizing the discrepancy between backward numerical differentiation before the step and forward of the data point after the step. This optimization employs MATLAB's *solve* function over segments, typically

1/5 of the data set at a time, securing a stable correction factor for each segment. Segmentation is optional but facilitates robust analysis. The efficacy is verified through numerical differentiation post-correction.

A simple phase correction employs backward numerical differentiation, assuming the phase changes continuously, with forward differentiation used at the onset of a phase shift. Both variants of correcting the phase rely on a smooth continuation of the trend in the data, otherwise higher order numerical differentiation may be necessary. In the last step of the raw data preparation, the phase shift is inverted for a positive direction and normalized. The latter is done under the assumption of complete filling.

The chosen method, while non-standard, is validated for its robust performance, yielding smooth results efficiently. While a simple multiple of 2π could theoretically compensate for phase steps, this method's computational efficiency and robustness justify its selection. The resulting concordance with absolute FFT, free from its limitations, further substantiates the method's reliability (see Fig. 4.4).

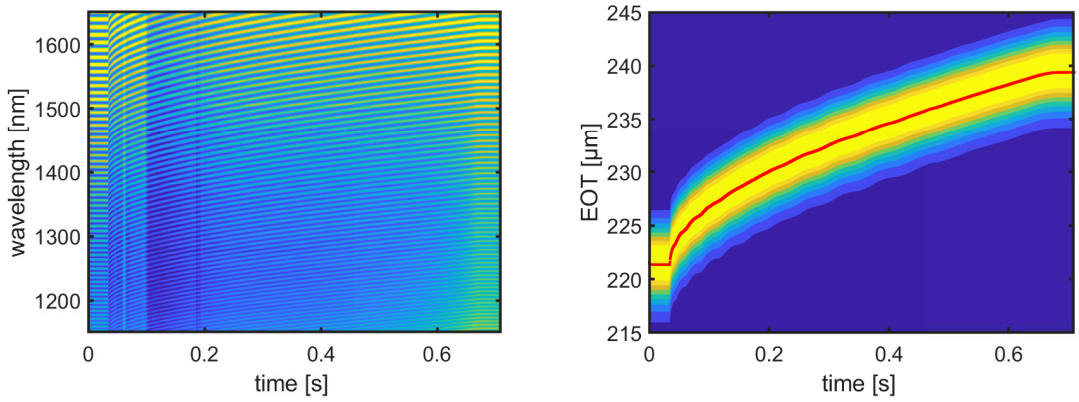

Figure 4.3: a) Spectrum of a p^+ pulsed-sample ($d = 50\,\mu m$, $\Omega = 55$ %) during capillary imbibition of 2-propanol. b) Power spectrum of the absolute FFT.

4.2.2 Metrology

In this study thickness, porosity, and pore size are essential parameters characterizing the investigated porous membranes. The mean pore radius of the mesopores is measured using nitrogen sorption isotherms (Table 4.1).

Two independent methods are employed to determine the thickness and porosity of the samples (Tab. 4.2). In the first method, pieces of $30-100\,mm^2$ are photographed at normal incidence and weighted by a micro-balance (Sartorius). Their thicknesses are measured from cleaved edges in SEM. The porosity is obtained by the formula $\Omega_{SEM} = 1 - \rho_{sample}/\rho_{Si}$, where ρ_{sample} is the measured density and $\rho_{Si} = 2.329\,g/cm^3$ [107] the bulk density of silicon.

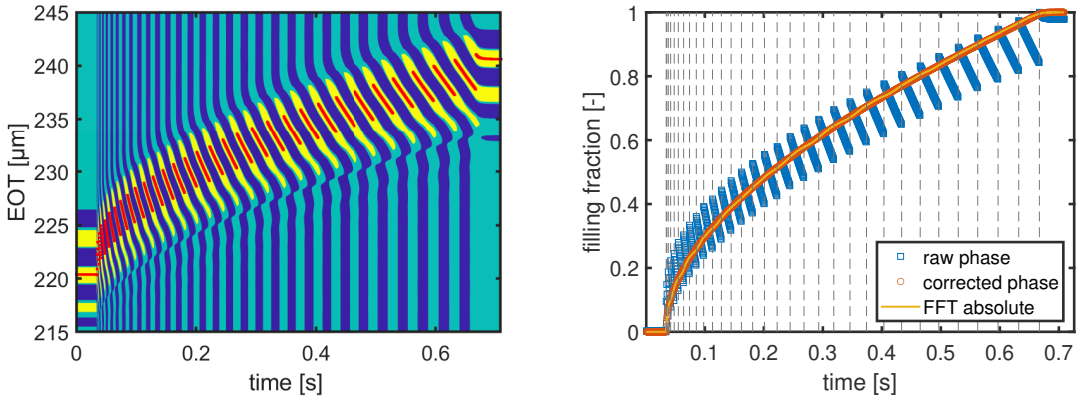

Figure 4.4: (left) Imaginary part of the FFT, with highest peaks marked in red. (right) Comparison of normalized raw and corrected phase with the absolute FFT, corresponding to the spectrum in Fig. 4.3. Here, the disadvantage of the absolute FFT is apparent by artificial bumps of the curve. The course of the corrected phase doesn't show this flaw.

Additionally, the porosity and thickness are ascertained via the RIFTS method.[11] The procedure is described in subsection 3.2.1. Here, rather than the highest peak, the center of gravity G (Equation 4.1) is used to determine the optical thickness from the power spectrum of the FFT, specifically the squared intensity I.[57] Tab. 4.2 shows excellent alignment between the orthogonal *Maxwell Garnett* model and the density method. This effective medium model is particularly suited for independent cylindrical pores, as demonstrated by *Brandt et al.* through simulations and experiments with mesoporous and macroporous silicon.[63] For the 1/29-sample, a notable discrepancy between the density and optical methods suggests an increased number of pore interconnections. Interestingly, this discrepancy does not occur in the p^{++} sample, which has an even higher porosity. This can be attributed to the fabrication process. During electrochemical etching, the pore walls remain mostly inert to the nucleophilic attack of HF, especially the thinnest walls, keeping the pores primarily independent. In post-treatment for the 1/29-sample, the entire surface undergoes oxidation, and the oxidized layer is then removed, potentially leading to breakthroughs in the pore walls.

$$\mathrm{G} = \frac{\sum_{\mathrm{n}} e_{\mathrm{ot,n}} I_{\mathrm{n}}^2}{\sum_{\mathrm{n}} I_{\mathrm{n}}^2} \tag{4.1}$$

4.2.3 Inverse Problem

The primary goal of addressing the *inverse problem of capillary filling* in mesoporous silicon (PSi) involves probing the structure at the pore scale over the whole length. Solving this problem is predicated on the assumption of a representative mean radius

Table 4.1: Nitrogen sorption isotherms conducted with a Quantachrome AS-iQ. The isotherms are analyzed using the *Barrett, Joyner, Halenda* (BJH) method.

sample	radius [nm]	pore volume [cc/g]	surface area [m^2/g]
p^{++}	4.6	1.78	863
constant	3.9	0.47	253
pulsed	5	0.55	231
1/29	6.3	1.13	314

Table 4.2: Comparison of thickness d and porosity Φ determined by SEM and image area assessment with weighting, and the orthogonal *Maxwell Garnett* (oMG) effective medium model using the *spectral liquid infiltration method* (see subsection 2.2.1), which can be summarized as two RIFTS measurements of a membrane entirely filled by air and by a liquid.[11]

sample	d_{SEM} [µm]	Φ_{SEM} [%]	d_{oMG} [µm]	Φ_{oMG} [%]
p^{++}	48	80	50	82
constant	59	52	60	54
pulsed	50	52	52	55
1/1	53	66	52	65
2/3	49	66	52	69
1/29	53	77	55	83

for the material across each finite layer slice perpendicular to the fluid's entrance plane. Consequently, the reasonableness of assuming such a radius for PSi must be evaluated.
Scanning electron microscopy reveals a dendritic, branching structure of mesoporous silicon, particularly pronounced in p^+-doped wafers. Consequently, the notion of independent pores warrants scrutiny. Despite this, a preferential pore directionality exists in the etching process, with lateral connections being relatively small compared to the main pores, as shown by transmission electron microscopy.[109] Section 2.3 formally derives the laws governing capillary flow, elucidating the driving mechanisms, namely the *Young-Laplace* pressure and hydraulic resistance. Beyond initial imbibition stages, wall friction imposes transport resistance, defined by the preceding filled length up to the fluid front. Phenomenologically, most of the fluid transport is achieved via the path of least resistance, as effectively modeled by a representative pore in the main transport direction. According to *Hagen-Poiseuille's* law, smaller pores such as the lateral connections show significantly lower transport rates and can therefore be neglected as long as they are not bottlenecks for the fluid transport in the structure.

Section 2.3.3 offers a volumetric solution to the *inverse problem of capillary filling* from pore extremities. The equation's volumetric variant (Eq. 4.2) is applied to dynamic spectroscopy imbibition curves. The latter are normalized by minimum

and maximum EOT in each measurement, thereby yielding the volumetric filling fraction. For any membrane with pores that deviate from a perfect cylinder and homogeneous surface chemistry, the imbibition time will not be equal in both directions. Since the data is recorded in equal time steps, this results in different array length. Therefore, the shorter data set is interpolated to equal it. Furthermore the data sets are treated by a moving average over five points.
Solving Eq. 4.2 requires the differential of the volume fillings, the respective times and the bulk fluidic parameters. Given that volume fillings are measured indirectly via volume fractions, supplementary steps are essential. Utilizing MATLAB's *fsolve*, optimization seeks a single volume for both directions of imbibition. The optimization task involves a simple cylinder volume function $V_0 = \pi r_0^2 d$ and a nested function for Eq. 4.2. The latter solves for the apparent mean radius r_0, minimizing discrepancies between membrane thickness d of the membrane, and the imbibition length obtained from Eq. 4.2. Subsequently, r_0 is employed to calculate volume filling through Eq. 4.3, culminating in the determination of the radius course over the imbibition length.
In the nested function around Eq. 4.2 the volume filling for the reverse direction is inverted by subtracting the data set from its terminal point. Next, an equally spaced volume filling is calculated. It is followed by an interpolation of imbibition times with the respective volume and the query points from the equally spaced volume filling. The imbibition times over fixed volume steps are differentiated by first order numerical backwards differences. The radius course is then derived through trapezoidal numerical integration of Eq. 4.2. Finally, the imbibition length is obtained by cumulatively summing the derivative of the evenly spaced volume, divided by the circular area spanned by each radius.
In the absence of optimization, the height computed in the final step deviates from the membrane's thickness. As discussed before (subsection 3.2.2) the pore structure of mesoporous silicon can be conceptualized as a tube with a series of constrictions. This recurring bottleneck structure at the nanoscale necessitates accounting for a geometric correction factor, as it diminishes liquid transport compared to predictions from a mean radius using the *Lucas-Washburn* equation. Consequently, the pore radius obtained by this method is considered apparent rather than geometrical.
For the *inverse problem of capillary filling* in PSi, 2-propanol is utilized. It has a bulk viscosity of 2.0120 mPas [110], a surface tension of 20.9 mN/m [111] and the contact angle is assumed to be zero. As long as the surface chemistry does not alter from wetting to non-wetting, the contact angle dependent *Young-Laplace* pressure remains a relatively constant driving pressure, maintaining its order of magnitude. This constancy is valid even when the meniscus encounters the edge of a constriction.

$$r(x) = \frac{f(V)}{\Gamma_1^{*1/5}\pi^{2/5}} \left(\int_0^{V_{\text{tot}}} f(V)^{-6} \mathrm{d}V \right)^{1/5} \tag{4.2}$$

$$\mathrm{d}V = \mathrm{d}\left(\frac{V - V_{\min}}{V_{\max} - V_{\min}}\right) V_0 \tag{4.3}$$

In the first application of the method the inverse problem is solved for three typical synthesis procedures of mesoporous silicon. Fig. 4.5 displays the results of the capillary imbibition and the respective inverse solution for the radius of a p^{++}-sample, a p^+ pulsed-sample and a p^+ constant-sample. Each radius profile undergoes validation by reversing the inverse solution using an ordinary differential equation solver based on *Hagen-Poiseuille's* law, which calculates the imbibition curves for comparison with the initially measured curves. Fig. 4.6 confirms reasonable agreement with the measured imbibition dynamics. For a) and b) the agreement in one direction is clearly better than for the other. This can be due to a slight discrepancy of the measured spots. Another reason involves the sampling rate, since capillary imbibition slows down over time, time steps average over a decreasing segment size. Conclusively, imbibition in the initial etching direction provides more structural detail at the substrate's base, and the reverse is true for the opposite direction. Towards the end of the imbibition measurement, an apparent reduction in kinetic speed is noted, attributed to the material's pore size distribution. As pores fill at different rates, filled pores cease to affect filling dynamics, leading to an apparent reduction of the imbibition kinetics. Despite these potential error sources, the demonstrated reversibility confirms the method's self-consistency.
The radii in Fig. 4.5 are divided by their means over the entire length to detect any gradients in pore radius. It is evident that the imbibition of the p^+-doped membranes is faster in the original etching direction compared to the reverse, whereas the opposite is observed for the p^{++}-sample. This observation aligns with the radius profiles, where the p^{++}-sample exhibits a linear increase in radius along the etching direction. In contrast, the p^+ constant-sample demonstrates an inverse trend, albeit less pronounced, and the p^+ pulsed-sample remains relatively constant, tapering slightly towards the bottom in the etching direction. Detailed examination of the radius profiles reveals local minima and maxima approximately 1 µm wide, seemingly with periodic patterns. These regular features might be attributed to measurement technique errors or FFT evaluation inaccuracies. Previously considered constrictions are expected on a nanometric scale in terms of length and width, potentially exceeding resolution limits. Nevertheless, a notable agreement exists between these apparent constrictions and density distribution visualizations from mean field theory for sorption isotherms.[112]

Furthermore, the inverse problem is employed to investigate p^+ pulsed-samples that are post treated by oxidation and subsequent HF-dipping at different ratios of hydrofluoric acid and ethanol. The technique, as previously documented, results in a smooth pore wall surface, confirmed by *Raman* spectroscopy and SEM imaging.[113] Unfortunately, the procedure and composition of the etching solution are not reported in detail. Here, three different solutions (section 4.1) are tested for the post electrochemical etching procedure and investigated by the *inverse problem of capillary filling*.

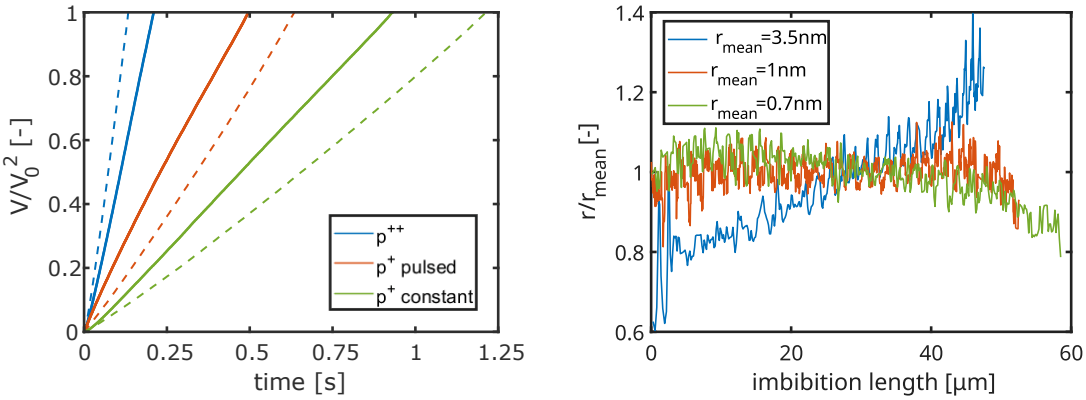

Figure 4.5: (left) Normalized squared filling fractions plotted against time, illustrating imbibition in the etching direction (solid lines) and against it (dashed lines). (right) Inverse solution of a p^{++}-sample ($r_{\mathrm{mean}} = 3.5\,\mathrm{nm}$), compared to p^+ membranes under pulsed ($r_{\mathrm{mean}} = 1\,\mathrm{nm}$) and constant ($r_{\mathrm{mean}} = 0.7\,\mathrm{nm}$) etching. The resulting pore radius is divided by the respective mean, to reveal the trends of the radii. The length is plotted in the direction of the etching procedure i.e. the ordinate origin is the top side in the etching.

Capillary infiltration depicted in Fig. 4.7 adheres to a square root of time, corresponding to a squared filling fraction uniformly across all samples. The infiltration rate in the prior etching direction consistently surpasses that in the opposite direction. Furthermore, the post-treatment substantially enhances permeability, dictated by the HF/EtOH ratio, an observation corroborated by the apparent pore radius profiles derived via the *inverse problem of capillary filling*. The 2/3- and 1/1-samples exhibit only minor differences, but they display clear distinction from the initial p^+ pulsed-sample. Among the samples, the 1/29-sample from the same batch demonstrates significantly enhanced permeability. Its radius profile appears more complex, having a stronger slope at the first fifth of the top side during the electrochemical etching and a less steep slope in the rest of the membrane. Replication of the 1/29-sample synthesis from a fresh p^+ pulsed-sample confirms the repeatability of both synthesis and investigative methodology.

Comparing SEM images of a p^{++}-sample and a p^+ pulsed-sample (Fig. 4.8), the pore channels of the former are more obvious and better aligned, whereas the latter seems to have a more dendritic structure. This structural disparity is reflected in the apparent mean radii $\langle r_{\mathrm{app}} \rangle$ derived from the inverse problem. There, the p^{++}-sample shows a significantly higher value than the p^+-samples and approaches the radius $\langle r_{\mathrm{BJH}} \rangle$ from the nitrogen sorption isotherms (Tab. 4.1). The ratio Eq. 4.4 can be used to approximate the geometrical correction factor Ω for the constriction model or the streamline tortuosity τ_{s} (Tab. 4.3). Ω is highest for the as prepared p^+-samples, whether they are constantly or pulsed etched has a comparatively low influence. Interestingly, the post treated 1/29-sample reaches a

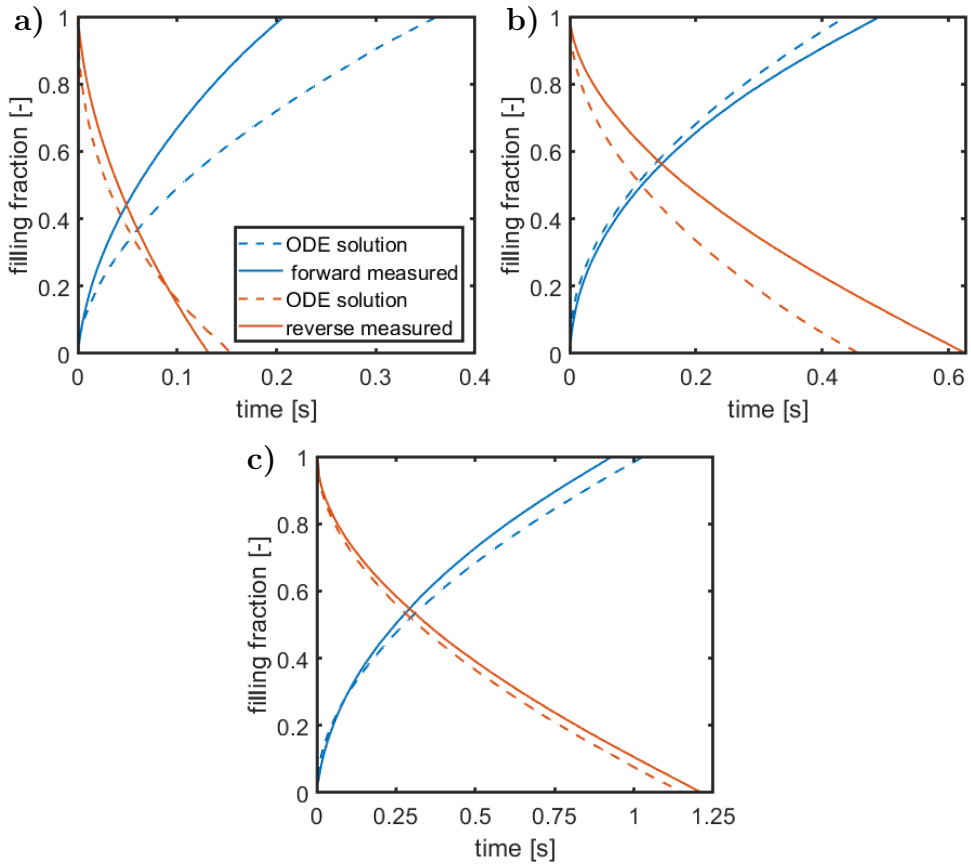

Figure 4.6: This figure displays the reverse calculation of imbibition curves of the inverse problem. MATLAB's *ode23*-solver is used to solve *Hagen-Poisseuille's* law with the radii from the inverse problem of the a) p^{++}-sample b) p^{+} pulsed-sample and c) p^{+} constant-sample.

similarly low geometrical correction factor as the p^{++}-sample. In the second SEM image series (Fig. 4.9) the transition from a dendritic to a skeletized structure is observable depending on the dilution by ethanol in the post treatment solution. In Fig. 4.9 d) a relatively straight pore pathway is revealed, once the dendrites that sit on the surface of the pore walls in a) are selectively etched. This supports the hypothesis that slow imbibition dynamics are due to numerous successive bottle-neck structures, as explained by the constriction model (subsection 3.2.2). The constriction model without immobile layer (Eq. 3.6, 3.7) is used to calculate the minimum and maximum pore radius along the main pore axis, that explain the low apparent pore radius.
The streamline tortuosity of mesoporous silicon with p^{+}-doping is previously reported with a value of 2.6.[54] This value is in approximate agreement with the results in Tab. 4.3, also given the fact that the synthesis deviates slightly. However, it is important to note that this literature value is based on SEM images from the surface, which may not be ideal due to SEM's reliance on grayscale thresholding

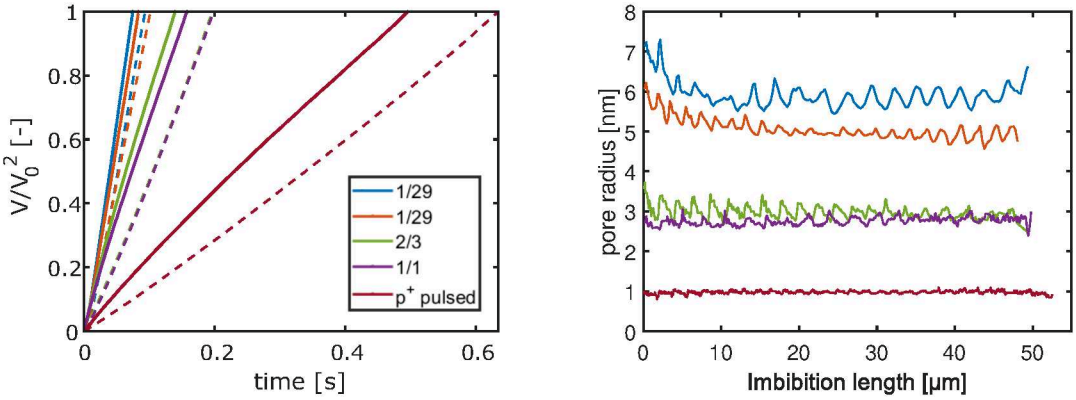

Figure 4.7: (left) Normalized filling fractions squared versus time of imbibition in direction of the etching (solid lines) and against it (dashed lines). (right) Inverse solution of a p^+-etched membrane, cut into separate samples that are post-treated differently after primary etching. The orange curve represents a complete repetition of synthesis, including a fresh membrane.

and the tendency for surface pore entrances to appear larger.[11] The magnitude of these values viewed in the context of stream lines suggest a strongly meandering path, which must involve meandering pore walls. This observation conflicts with the much lower tortuosity found in the 1/29-samples, as extensive pore wall dissolution would compromise structural integrity and necessitate rectifying etching mechanisms. Thus, a plausible explanation is that dendrites on pore walls contribute to the repeated bottle-neck formations, and the elevated tortuosity should be interpreted through the constriction model.

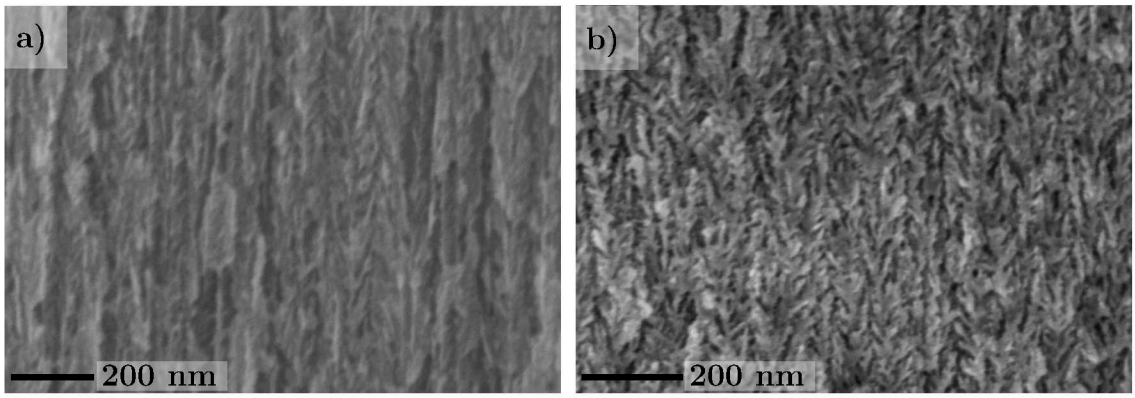

Figure 4.8: SEM images of cleaved edges taken by a Zeiss Supra 55 VP (WD 2 mm, EHT 2 kV, aperture 20 µm). The top side during electrochemical etching is also the top side in the excerpts shown. a) p^{++}-sample b) p^+ pulsed-sample.

Table 4.3: Apparent pore radius, geometrical correction factor Ω and streamline tortuosity τ_s by evaluation of the inverse problem and nitrogen sorption isotherms. Ω is further used to calculate the minimum and maximum pore radius.

sample	$\langle r_{app} \rangle$ [nm]	Ω	τ_s	r_{min} [nm]	r_{max} [nm]
p^{++}	3.5	1.3	1.1	3.9	5.3
constant	0.7	6.0	2.4	2.3	5.5
pulsed	1.0	5.1	2.3	3.1	6.9
1/29	5.1	1.2	1.1	5.6	7.1

$$\frac{\langle r_{BJH} \rangle}{\langle r_{app} \rangle} \approx \Omega = \tau_s^2 \tag{4.4}$$

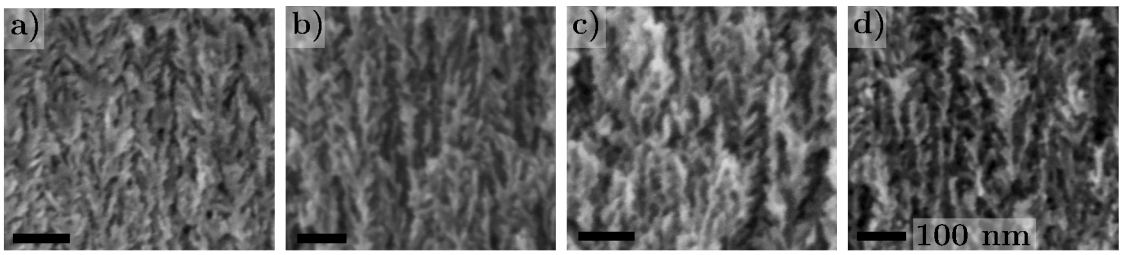

Figure 4.9: SEM images taken by a Zeiss Supra 55 VP (WD 2 mm, EHT 2 kV, aperture 20 µm) investigating the cleaved edge of samples with different treatments after pulsed etching. The top side during electrochemical ecthing is also the top in the images. a) as prepared p^+ pulsed-sample b) 1/1-sample c) 2/3-sample d) 1/29-sample.

Electrochemical etching of porous silicon below the electropolishing limit tends to remain within existing grooves, such as pre-existing pores or pre-patterns on a silicon wafer. Changes in concentration or current density do not typically generate new pores but rather alter the dimensions of existing ones. This phenomenon is attributed to the quantum wire effect and the susceptibility of stretched bonds to fluorine attacks.[8, 11] Consequently, porosity and pore radius scale largely similar. An x-ray scattering study, supported by SEM and nitrogen sorption isotherms, on mesoporous silicon synthesized from p^{++}-doped wafers shows that the surface porosity is depending on the applied current density. Their porous layers have a thickness range from 10 to 25 µm using constantly applied current densities between 50 mA/cm^2 and 110 mA/cm^2 for 5 min each. For the in depth porosity they found a variation specific for the different etching conditions, but always an increasing trend in the etching direction.[42] This increasing porosity agrees with the results in this thesis (Fig. 4.5).
Thelen et al. utilized elastic guided waves to probe mesoporous silicon, prepared

using methods similar to the p^+ constant-sample approach. In their investigation of the effective mechanical behavior from the dispersion relation they found a stiffness gradient in depth of the membrane along the main pore axis. This is explained by a cone shape of the pores, where the widest radius is the top side during the etching.[43] Here, the inverse solution corroborates this trend for p^+ constant-samples, with the determined radius profile revealing only minor deviations from a conical shape (Fig. 4.5).
Pulsed etching of porous silicon, known in the context of photoluminescence research, exhibits steeper pore walls, a more uniform optical appearance, and enhanced emission efficiency compared to samples etched constantly. This enhancement is linked to the more stable concentration of the etching solution in the reaction area [114–116], consistent with the observations in this thesis (Fig. 4.5).
Kumar et al. proposed chemical surface oxidation followed by hydrofluoric acid solution treatment. This study revisits this approach by examining effects at varying ethanol dilutions, achieving less dendritic pore morphology in alignment with *Raman* shift analyses.[113] Critically, the original study lacked details regarding the concentration of hydrogen peroxide and the hydrofluoric acid to ethanol ratio during post-treatment. Furthermore, SEM images appear to be mislabeled, as samples in this thesis show that post-treated samples resemble what was documented as untreated in their work, with no equivalent found here for the exceptionally smooth pores following their post-treatment.

The fundamental query in synthesis and material design concerns the explanation of radius profiles based on synthesis conditions and formation mechanisms. Literature presents numerous methods and parameters affecting pore morphology.[10, 11, 117] Key to the electrochemical dissolution process is the availability of electron holes in the valence band, facilitating nucleophilic attacks by fluorine anions on silicon. In p^+-doped silicon these holes are mainly influenced by quantum confinement diminishing the transport of holes in the pore walls and the higher field density at pore tips attracting the charge carriers. Despite high HF ratios intended for uniform pore growth as employed here, such uniformity is only observed in pulsed etching conditions. For p^+ constant-samples pores are decreasing in the etching direction. The probable explanation includes chemical etching processes, where pores enlarge over extended exposure to the etching solution. However, p^+ pulsed-samples, subjected to longer exposure due to waiting periods between pulses, experience a different response. A possible explanation suggests formation of less stable crystal facets that dissolve slowly over time during constant etching, while more stable (111)-planes dominate in pulsed etching.
An increasing diffusion path length and the constant current application are ascribed a decrease in the HF concentration at the pore formation region. This would shift the reaction kinetics in favor of oxidation by water. Such formed oxides hinder the conduction of electron holes, which slows down the dissolution by HF even more and the oxidation continues. The oxide layer is prone to chemical etching by HF. This is the mechanism leading to electropolishing.[11] Therefore, a decrease of the

concentration is expected to increase the pores. This explains a pore gradient in the opposite direction than observed for p^+ constant-samples, as observed for the p^{++}-samples.

4.2.4 Conclusion

The presented *inverse problem of capillary filling* by imbibition from both ends of a mesoporous membrane effectively reveals the pore structure of PSi and establishes a connection to its synthesis conditions. It is complimented by a constriction model describing the capillary imbibition dynamics. The only requirement for the analysis are bulk fluid parameters and a mean pore radius, here from nitrogen sorption isotherms.
Porous silicon from p^{++}-doped wafers exhibits a linear pore widening in the etching direction. The opposite trend is observed for p^+-doped ones. There, the pore pathways resulting from constant and pulsed current applications are distinguished as well. Pulsed current application results in nearly straight pores, whereas constant current application yields conical pores. Beyond pore traces, mean apparent pore radii are determined, measuring approximately 1/5 and 3/4 of the radii derived from nitrogen isotherms for p^+- and p^{++}-wafers, respectively. This discrepancy is attributed to the microstructure. Evaluation with a *constriction model* leads to an appropriate geometrical correction factor Ω, linked to the sizes of pore constrictions and cavities. The previously used streamline tortuosity τ_s, which reflects the path length of fluid molecules through a meandering pore can be calculated from the square root of Ω. For p^{++}-samples a τ_s of 1.1 is calculated. p^+-doped ones have a higher τ_s of 2.4 and 2.3 for constant and pulsed current application, respectively.
A stripping technique, consisting in wet chemical oxidation and a subsequent HF-bath, on pulse etched p^+-samples reveals straight pore traces and the same τ_s as for p^{++} samples. This confirms that the high τ_s is linked to the dendritic surface apparent in SEM images. Therefore, the *constriction model* is an improvement compared to standard tortuosity models. Discrepancies between tortuosity and constriction description are particularly impacting, if an immobile layer must be taken into account (see subsection 3.2.2). Additionally, the theory based on mean radii of constrictions and cavities connects well to the discoveries and novel models of sorption isotherms on mesopores.[91, 112, 118]
The presented inverse solution method is also applicable for other measuring techniques of capillary imbibition e.g. measuring the mass uptake by liquid infiltration. These can be used for membranes thicker than 100 µm, where the applicability of the optical method tapers of. It should be noted though, that the *inverse problem of capillary filling* is based on the lubrication approximation and laminar flow. Sharp corners or outliers lead to artifacts.

In summary, the morphology of porous silicon can be manipulated through various parameters and methods. Extensive efforts have been previously required to evaluate fabrication recipes, particularly at the mesopore scale. The method

presented here, involving imbibition from both sides and solving capillary filling laws for pore radius, offers an affordable, rapid, and detailed solution. This technique can evaluate etching procedures, designed flow resistance, and quality assurance. Recent theoretical work on the *inverse problem of capillary filling* by imbibition from one side only, provides the advantage of even being applicable to pores with only one opening.[119] The technique is more demanding with regard to numerical methods.

5 Reflectometry: Water Ad- and Desorption

For the subsequent investigations, the chip-like reflective sensor (CLRS), which is introduced in subsection 2.2.4, is optimized for water sorption experiments. Stacks of hydrophilic homogeneous porous layers and 1-D photonic crystals (PC) of mesoporous silicon are employed to measure water sorption isotherms, capillary filling and drying. Measurements are conducted using in situ white light spectroscopy at normal incidence and reflection.

5.1 Sample Preparation

The samples produced for this study are etched by the same method and setup as described in section 3.1, wherein the calibration procedure for etching is detailed. The PC, an optical microcavity, is etched in at different positions of an otherwise homogeneous porous layer. Sample designs maintain a constant total volume. Therefore, the homogeneous layer, even if split into two parts by the PC, overall amounts to a thickness of 18 µm (compare Table. 5.1). The PC itself extends to a thickness of $\approx 3\,\mu m$. During the etching of the homogeneous layer, a current of 10 mA is applied for an area of 78.74 mm^2, which produces the lowest porosity of 55.5 % and therefore also pore diameter in the overall sample. The sequence for the PC is 60 $\lceil 10\ 40 \rceil_8$ 40 $\lceil 10\ 40 \rceil_8$ mA, with a porosity of 69 % and 75.5 % for 40 mA and 60 mA, respectively. After etching the samples are still attached to their approximately 500 µm bulk material. To turn the samples hydrophilic, they are oxidized for 2 h at 673 K in an oven with standard atmosphere. At this temperature the oxidation is limited to a thickness of few nanometers covering the in- and external surface.[11]

Table 5.1: Homogeneous layer apportionment around the PC, where d_{first} and d_{last} are the thicknesses of the layer in front and after the PC with respect to the open pore side. These values are estimated from calibration of the etching process.

sample	d_{first} [µm]	d_{last} [µm]
I	0	15
II	3	12
III	9	6
IV	12	3

5.2 Optical Water Sorption: Setup and Experiments

For optical soprtion experiments, the previously detailed spectroscopy setup (section 3.1) is extended by a commercial humidifier (proUmid MHG32) and a custom-designed cell. The humidifier provides an accuracy of $\pm 0.8\,\%$ in a range from $2-98\,\text{rh}\%$ at $283-303\,\text{K}$ and flow rates from $5-1200\,\text{ml/min}$. Fig. 5.1 illustrates the components of the custom-designed cell. A throttle ensures good mixing directly in front of the main chamber and a spring-loaded valve with a long plastic hose serves as an outlet. The sample holder is equipped with a hold-down having a cutout to ensure good gas exchange, at the same time it service as a spacer for an ideal distance of 2.4 mm of the reflection probe.

5.2.1 Water Sorption Isotherms

The sampling frequency for water isotherms was 6 s for both humidifier and spectroscopy setup. Integration times for the spectrometers are adjusted individually. Before the isotherm samples and measuring cell are flushed by nitrogen for at least 16 h with a set flow rate of 800 ml/min. The actual rate is lower because of throttling elements of the self build cell. During the isotherms the flow rate is adjusted by the humidifier according to the programmed humidity course (Fig. 5.2 b). The humidity is set to a maximum of 85 rh% to limit bulk condensation.

5.2.2 Water Imbibition

Capillary imbibition of ultra pure water is initiated by drop-casting with a micro capillary. The experimental procedure and analysis follow the approach described in chapter 3, with minor modifications. A center of gravity formula is utilized to track the effective optical thickness in FFT, instead of the peak height algorithm used previously. A time resolution of 200 μs is achieved by directly storing with the respective integration time on the RAM of the spectrometers. The spectrometer

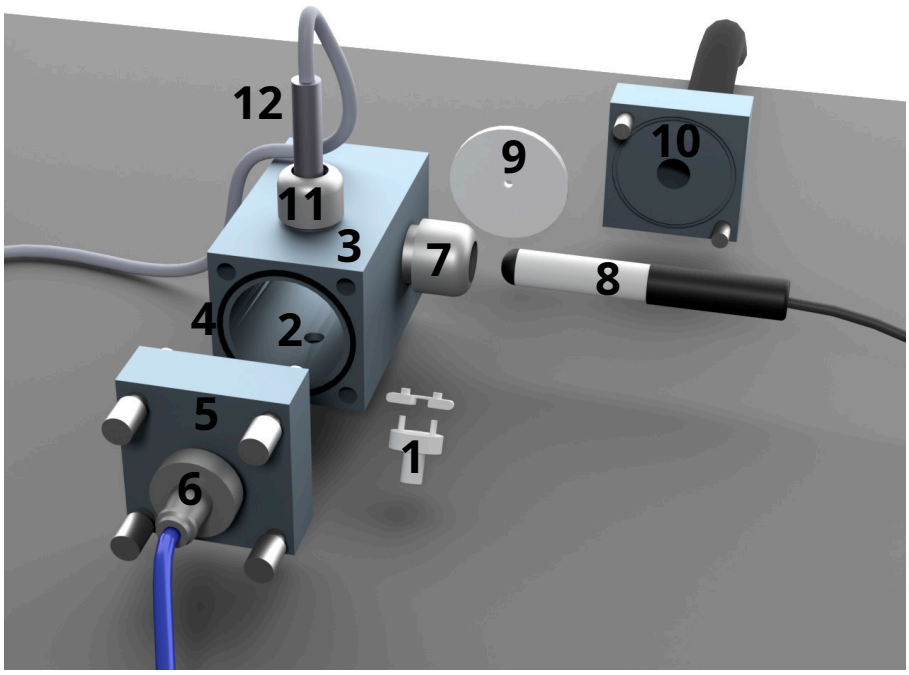

Figure 5.1: Schematic of the optical water sorption setup: 1) PTFE sample holder with clamp, 2) recess for sample holder, 3) cell body (VA steel), 4) O-ring in groove, 5) front cover with knurled screws, 6) valve, 7) pinch seal, 8) humidity probe, 9) throttle, 10) connector to humidifier (proUmid MHG32), 11) pinch seal, 12) reflection glass fiber probe.

for the visible and near infrared region cannot be initiated simultaneously from the instrument side in this case. A transmitted trigger by USB cables could induce different delays, but they can be synchronized by the obvious onset shifts in the measured spectra.

5.2.3 Drying Experiments

For the drying experiments samples are saturated via vapor phase at $85 - 90\,\mathrm{rh\%}$. A complete filling is assured by a constant optical thickness over a period of 15 min. The drying is induced by a nitrogen stream, setting the humidifier $0\,\mathrm{rh\%}$. Three flow rates 200 ml/min, 400 ml/min and 800 ml/min are tested for each sample. The temperature stays at $299 \pm 3\,\mathrm{K}$.

5.3 Optical Water Isotherms

In the following optical water sorption isotherms on mesoporous silicon with a PC at different positions are analysed. Given a spot size of approximately 0.25 mm^2, the technique is complementary to volumetric sorption isotherms, as it allows to create maps from local measurements or measure small samples, that are below a critical volume for other techniques. This is limited to a layer thickness with sufficient reflectivity and a frequency of the interference pattern low enough for the given spectral resolution. Notably, the latter can be increased by using a smaller entrance slit of the spectrometer. The loss off intensity accompanied by this exchange can be compensated by higher integration time for slow processes. For the given configuration an upper thickness limit of 100 µm is determined experimentally for homogeneous mesoporous silicon membranes with a porosity of 55 %.

Continuous measurements are conducted for optical water sorption isotherms here, capturing transients between equilibrium points where the relative pressure remains constant. Figure 5.2 a) displays the measured spectrum of a sample with the PC directly at the surface, followed by a 15 µm homogeneous layer (sample I in Tab. 5.1). The resonance position of the PC, marked by a red dashed line starting at 790 nm, is determined using a *Gaussian* fit of the inverted intensity around the central wavelength of the preceding spectrum within the *Bragg* reflection region, where the reflectivity is high (yellow area near the central cavity). A width of 60 nm suits all samples of this study. Above a wavelength of 1000 nm, a superposition of interference patterns emerges. The lower frequency component corresponds to the PC's overall effective optical thickness (EOT), while the higher frequency component arises from the entire porous structure stack. A peak of the latter is highlighted and tracked by a red dashed line. For the actual analysis the respective EOT is determined by FFT (Fig. 5.3), using the algorithm outlined in section 4.2. It involves interpolation, Hann-windowing and zero padding for the FFT. The EOT is determined by the center of gravity in a window around the peak of the overall porous layer stack.
To identify the equilibrium points of the isotherm a two step thresholding procedure is applied. In the first step the equilibrium points of the humidity course (Fig. 5.2 b) are determined. The data is treated by a moving mean and then differentiated by numerical central differences. Then, equilibrium points are determined by cutting of all points with a derivative value higher than the threshold. In the second step the same procedure is repeated for the filling fraction. Start and end positions of equilibrium point clusters, black dots in Fig. 5.2 c), can be identified by forward numerical differences of the remaining humidity data selecting all points higher than a threshold. Finally, the isotherms are obtained by plotting the mean of the equilibrium point clusters only (Fig. 5.2 d).

In Fig. 5.4, the isotherms of the overall stack a) and the PC b) are separately presented. Capital letters A-D in a) indicate characteristic points common across all

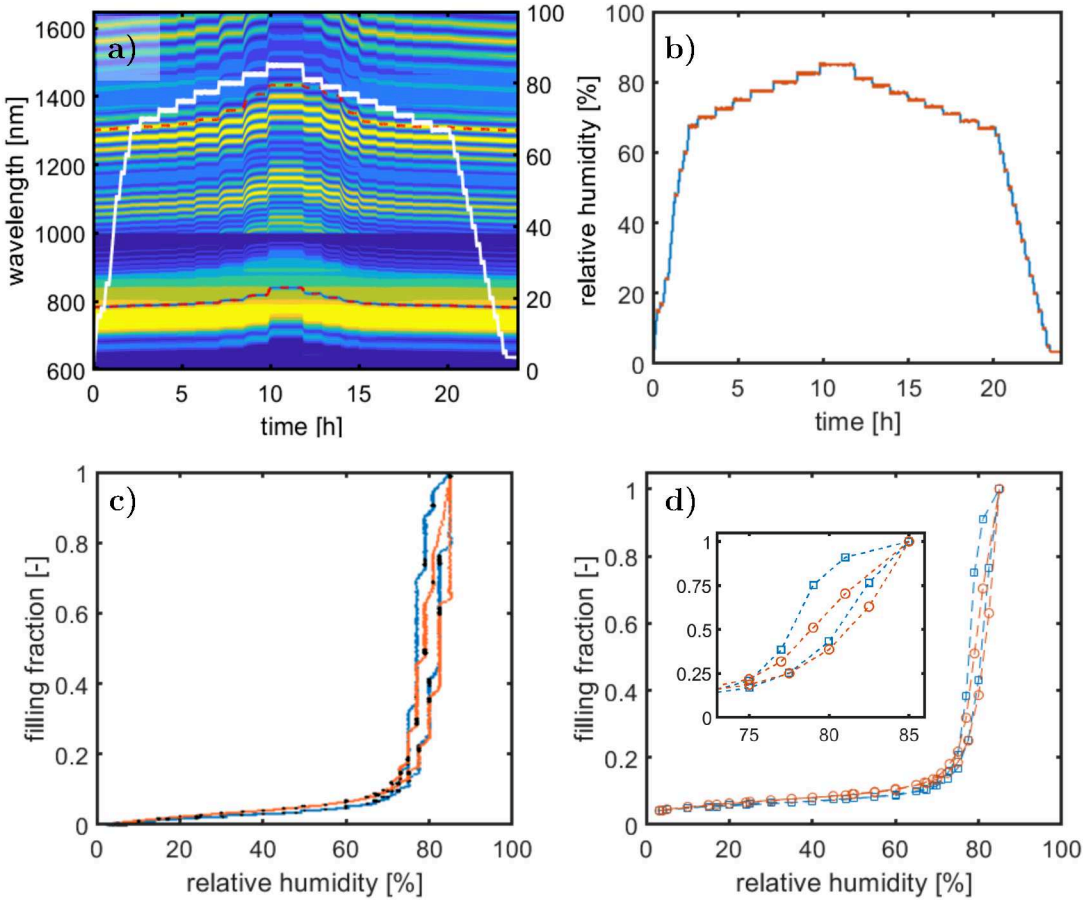

Figure 5.2: Optical water sorption isotherm a) contour plot direct spectrum over time. The intensity is depicted using a Parula color palette from blue, indicating low intensity, to yellow, indicating high intensity. Fits of a peak (upper) and the resonance position (lower) of the PC are indicated by red dashed lines. Measured humidity is displayed in white, with its magnitude indicated on the right abscissa. b) Plot of the humidity course in blue, with constant regions in orange. c) Optical isotherm showing transients in orange and blue for the optical thickness of the overall layer stack and resonance of the PC, respectively. Black dots represent equilibrium points. d) Optical isotherm of overall filling (blue, squares) and PC (orange, circles). The inset magnifies the hysteresis region.

sorption curves. Point A denotes the onset, where typically the first monolayer of the adsorbate covers the surface. Given that the drying procedure prior to the sorption isotherm involves flushing with dry nitrogen only, this initial monolayer is already adsorbed. Consequently, the onset of the filling fraction at 0.023 is determined from the last point of a volumetric desorption curve of sample II measured by a VSTAR sorption setup (Anton Paar). Preceding the volumetric isotherm, the sample undergoes drying at 453 K and vacuum conditions. In section A-B, where B consistently measures 24 %rh, a second layer develops, causing the filling fraction to

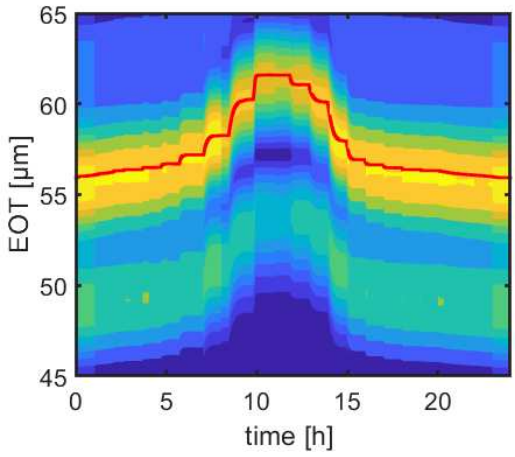

Figure 5.3: FFT power spectrum over time of sample I). The EOT of the overall stack peak is determined by the center of gravity in a fixed window size.

increase by 0.04. Point C marks the onset of hysteresis, occurring at approximately 70 %rh across all curves in a) and b). At point D, complete filling is achieved. The holding time for this final point of adsorption is extended to establish an equilibrium. Figure 5.2 a) indicates that the relaxation time for this final point is substantially shorter than for the preceding two humidity levels, as evidenced by the shorter transient region. In the interference pattern of these two prior points, filling proportional to the square root of time is observed. The observed shape and slow relaxation suggest meniscus-driven capillary filling.
The isotherms depicted in Fig. 5.4 adhere to a type V classification according to the IUPAC convention.[120] The initial flat region, indicative of a weak adsorbent-adsorbate interaction, suggests a type III profile, while the presence of hysteresis confirms classification as type V. The hysteresis is typically associated with capillary condensation and delayed evaporation due to pore blocking in mesopores. The observed hysteresis loops resemble the H1 type, characterized by similar slopes in both the adsorption and desorption branches. Notably, this similarity aligns with the reference IUPAC H1, particularly evident in isotherms I and IV in panel a). H1 hysteresis loops are linked to porous systems with minimal cooperative network effects, and ink bottle pores, with pore size distributions of constrictions and cavities of similar widths.[97, 120]
Upon comparing the hysteresis loops in Fig. 5.4 a) across the entire stack, isotherms I and IV demonstrate strong concordance. Sample II exhibits a consistent shape across both the overall stack and the PC. Sample III appears as a hybrid, combining elements of the shapes observed in I/IV and II. While for II and III the adsorption branches of the overall stack and PC coincide entirely, the slope in the capillary condensation region (adsorption branch C-D) for I and IV begins more sharply for the overall stack than the PC. The PC isotherms (Fig. 5.4 b) display a consistent shape, with a slightly larger hysteresis loop noted for I and IV when compared to the other samples. Notably, the absence of a plateau at the commencement of the

desorption branch D-C is attributed to a low number of data points at this junction, despite the clear presence of hysteresis. Tapered hysteresis loops of H3 and H4 types display a concave termination at the desorption branch from an abscissa standpoint, whereas the loops discussed here exhibit a convex nature, thus reinforcing their classification as H1. It is known for porous silicon that smaller pores have a more pronounced hysteresis.[11] Therefore, the overall less pronounced hysteresis of the PC compared to the overall stack is ascribed to larger pore sizes within the PC's central cavity. The pressure p_{oh} of the hysteresis onset is located at approximately 70 %rh across all isotherms.
A prior investigation into the sorption properties of PSi involved two stacking *Fabry-Perót* layers of varying pore size.[26] There, ink bottle shapes i.e. a layer of smaller mean pore radius in front of a layer with a larger one, with respect to the free surface, shows two hysteresis steps. It was concluded that the smallest radius in series with direct access to the pressure reservoir predominantly influences condensation and evaporation, and when situated before a larger radius segment, it delays subsequent evaporation. Corresponding to the constriction model, each etched mean pore size possesses a distinct constriction dimension, and layers with smaller radii can act as constrictions for those with larger pores. This scenario suggests that bottleneck phenomena induce local minima in free energy, effectively isolating pores in isotherms.[26] This mechanistic explanation accounts for the remarkably similar overall and PC hysteresis observed in sample II. It can be concluded that the PC in this sample acts as a bottle neck as a result of synthesis variance regarding the pore size.

A simplified approach for estimating pore size involves utilizing the *Kelvin* equation (Eq. 5.1) for characteristic points of the hysteresis loop.

$$r_{\mathrm{K}} = \frac{-2\sigma_{\mathrm{lv}} V_{\mathrm{m}}}{\mathrm{R}Tln(\frac{p}{p_0})} \tag{5.1}$$

At 293 K the molar volume V_{m} of water is $1.8 \cdot 10^{-5}\,\mathrm{m}^3/\mathrm{mol}$[121], the surface tension σ_{lv} is $73 \cdot 10^{-3}\,\mathrm{N/m}$[122] and R is the ideal gas constant. The characteristic points of the hysteresis loop are identified by enhancing the sampling rate by a factor of five using *Matlab*'s *interp* function. This is followed by the computation of numerical central differences and the subsequent identification of local maxima. The results are summarized in Tab. 5.2. Furthermore, the radius r_{oh} associated with the onset of the hysteresis at p_{oh} is 3 nm. Notably, sample II yields consistent results for both PSi and the overall stack isotherm. Given the sparse data points in the hysteresis region, these findings should be interpreted cautiously, though the pore sizes fall within expected ranges. Typically, the *Kelvin* equation tends to underestimate pore radius from sorption isotherms, since at the point of condensation already several layers of adsorbtive diminish the apparent pore radius. However, for a tube with random constrictions, a different mechanism emerges. Initial condensation occurs at constrictions, with further liquid meniscus ingress into adjacent pores occurring when the relative pressure is sufficiently elevated. This is

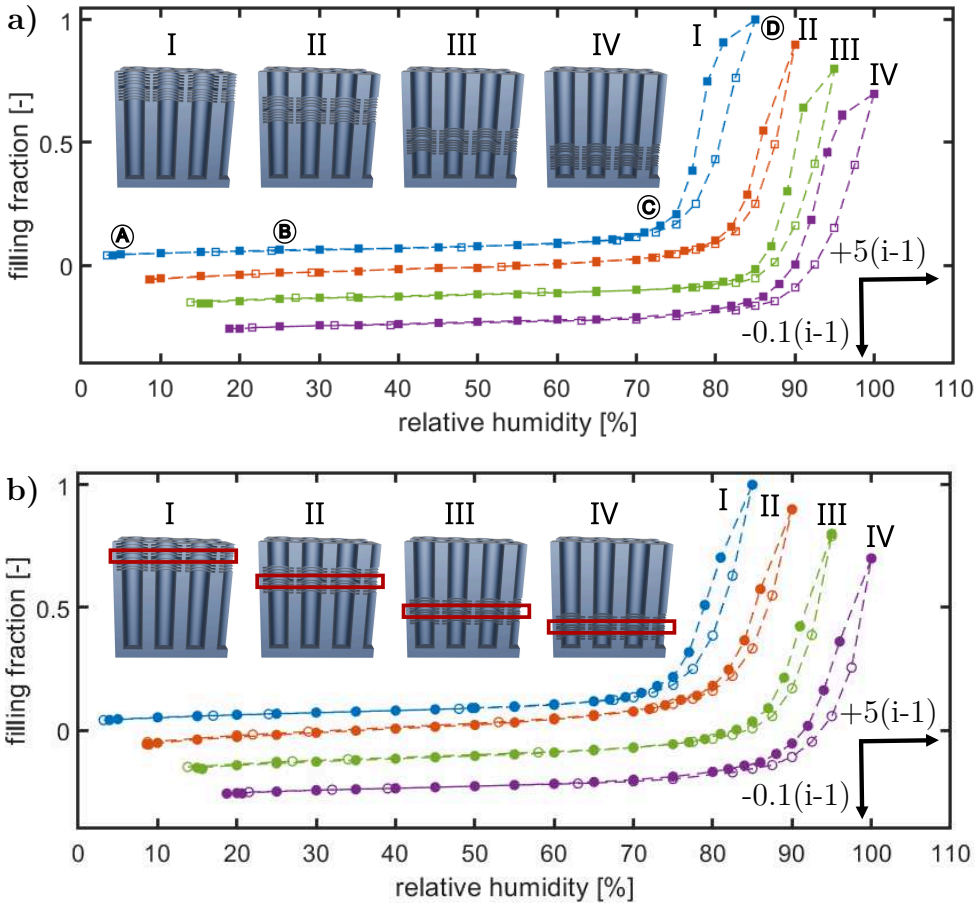

Figure 5.4: Optical water sorption isotherm of four samples with a PC at different heights in a porous layer of 18 µm, after I) 0, II) 3, III) 9 and IV) 12 µm from the surface. To avoid clutter the measurements are shifted according to the indicated arrows, where "i" is the respective roman number. Empty data tips indicate the adsorption and filled ones the desorption branch. the dashed lines are guide for the eye. a) is obtained from the EOT of the overal stack by FFT. b) is the result of the resonance shift of the PC.

known as *phase growth*.[118] In phase growth fewer adsorbtive layers are involved than in condensation, since the meniscus does not have to be formed, therefore the meniscus radius calculated by the Kelvin equation is closer to the actual radius.[118] For the overall stack's isotherms, the average radius of condensation $\langle r_c \rangle$ exceeds the average radius of evaporation $\langle r_e \rangle$, consistent with expectations for the hysteresis type. The smaller evaporation radius is connected to a lower relative humidity and attributed to constrictions impeding the emptying of larger pores, thus causing hysteresis.

For comparison with the previous chapters r_{oh} and $\langle r_c \rangle$ of the overall stack are inserted in the constriction model (subsection 3.2.2). The results are listed

Table 5.2: Characteristic pressures of the overall stack isotherms: $\langle p_c \rangle$ and $\langle p_e \rangle$ refer to the pressures used to approximate the average pore radius via the *Kelvin* equation, from the adsorption and desorption curve, respectively.

sample	$\langle p_c \rangle$ [%rh]	$\langle p_e \rangle$ [%rh]	$\langle r_c \rangle$ [nm]	$\langle r_e \rangle$ [nm]
I	82	78	5.3	4.4
II	85	85	6.6	6.6
III	85	80	6.6	4.7
IV	85	78	6.6	4.3

Table 5.3: Hydraulic radius $\langle r_h \rangle$ and streamline tortuosity τ_s, calculated from the square root of the geometry factor Ω using the simple constriction model (subsection 3.2.2). r_{oh} and $\langle r_c \rangle$ serve as the minimum and maximum radius, respectively.

sample	$\langle r_h \rangle$ [nm]	τ_s
I	4.2	1.5
II	4.8	2.2
III	4.8	2.2
IV	4.8	2.2

in Tab. 5.2, which includes the mean hydraulic radius $\langle r_h \rangle$. For comparability with literature, the streamline tortuosity τ_s is listed instead of the geometrical correction factor. Oxidation of samples induces a notable strain, potentially causing pore deformation and a subsequent decrease in pore size. In contrast to the as-prepared samples detailed in section 4.2, the tortuosity τ_s appears to remain largely unchanged. Direct comparison of the hydraulic mean radius is challenging due to the inclusion of varying pore sizes within the PC. Enhanced analysis using the mean field model for classical nucleation, as developed by *Saam* and *Cole* [123], which is frequently employed for mesoporous materials [27, 93], could offer improvements, given additional hysteresis loop data points. From the measured sorption isotherms here, there are several indications for a combination of nucleation and phase growth, where the more recent *serially connected pore model* [118] may be appropriate. A more comprehensive pore size distribution, accounting for radii at the full width half maximum, would provide better data for the constriction model.[91]

5.3.1 Microsecond Spectroscopy on Water Imbibition

Fig. 5.5 displays the capillary driven water imbibition for sample IV. The imbibition measurement, conducted under environmental conditions i.e. 293 K and $\sim$ 30 %rh, presumes that at least two layers of adsorptive water initially cover the surface. These layers are implicit zero points for normalizing the specified filling fractions in Fig. 5.5. The filling of the first homogeneous layer of 12 µm thickness is associated

with approximately 2/3 of the overall filling fraction. The calculated constriction model (black dashed line) closely agrees with input parameters of a water viscosity of 1.005 mPa s [124], surface tension of $73 \cdot 10^{-3}$ N/m[122] and a contact angle close to 0 at 293 K. An apparent radius of 0.4 nm is determined by a fit of a *Lucas Washburn* like equation $\mathrm{L}(t) = a \mid t - t_0 \mid^{1/2} + \mathrm{L}_0$, where $a = r_{\mathrm{app}} \sigma_{\mathrm{lv}} \cos\theta / \mu$. Here, t_0 and L_0 are the onset parameters of time and and imbibition length, respectively. The squared coefficient a^2 has a value of $3.6 \cdot 10^{-8} m^2/s$. It is two orders higher than a styrene dimer with a viscosity one order higher (compare Tab. 3.4). These dynamics align well with a prior study on oxidized porous silicon, where a value of 10^{-10} m^2/s is measured for an apparent radius of 0.02 nm.[125] Lastly, the streamline tortuosity of 2.3 from chapter 4, alongside the apparent radius of 0.49 nm, is used to calculate a hydraulic radius of 2.6 nm. From the constriction model, a minimum radius of 1.6 nm and a maximum radius of 3.6 nm are deduced. Considering an immobile layer of 0.5 nm [80] i.e. two molecular layers, for the tortuosity of 2.3, the hydraulic radius of 3.1 nm with a minimum radius of 2.1 nm and maximum radius of 4.1 nm is obtained.
In Fig. 5.5 b), the filling dynamics in the PC are rescaled by the prefactor of the $\sqrt{t}$-fit. Chronologically, the plot reads from right to left. The initial region of the spectrum presents a low signal-to-noise ratio, resulting in outliers in the determined filling fraction. Outliers exceeding a threefold standard deviation are omitted from the figure. As demonstrated in chapter 3, the filling of the PSi prior to the main meniscus arrival is identifiable via this plot. A simple cylinder formula approximates a precursor film or adsorbed layer on the surface. Taking the difference of the average filling fraction from 5 to 1.5 of the abscissa and the onset of a consistently increased filling fraction from 1.5 to 1.2, a layer thickness of 0.19 nm is calculated. This value aligns closely to the approximate size of a water molecule previously reported as 0.17 nm.[126]
The imbibition study coupled with sorption isotherms provides complementary insights. In the case of sorption isotherms, the resultant higher average pore radii encompass all pore sizes within the stack. Through the imbibition study, the average radius of the homogeneous porous layer is determined.

5.4 Drying Rates: Photonic Crystal

In a previous study drying of *Vycor* (*Dow Corning*), a porous glass monolith with a sponge like pore morphology is investigated by magnetic resonance imaging. The macroscopic monolith with 1.2 cm length and a 4 x 6 mm^2 base, has a pore radius of 4.6 nm and a Darcy based tortuosity of 3.6 [20]. The magnetic resonance technique enables the recording of one-dimensional saturation profiles along the sample's longitudinal axis. Instead of a drying front propagating into the samples, a homogeneous drying is observed. This phenomenon is attributed to a percolation mechanism and a diffusion-like drying.[127]
The pore radius of mesoporous silicon aligns closely with that of the previously

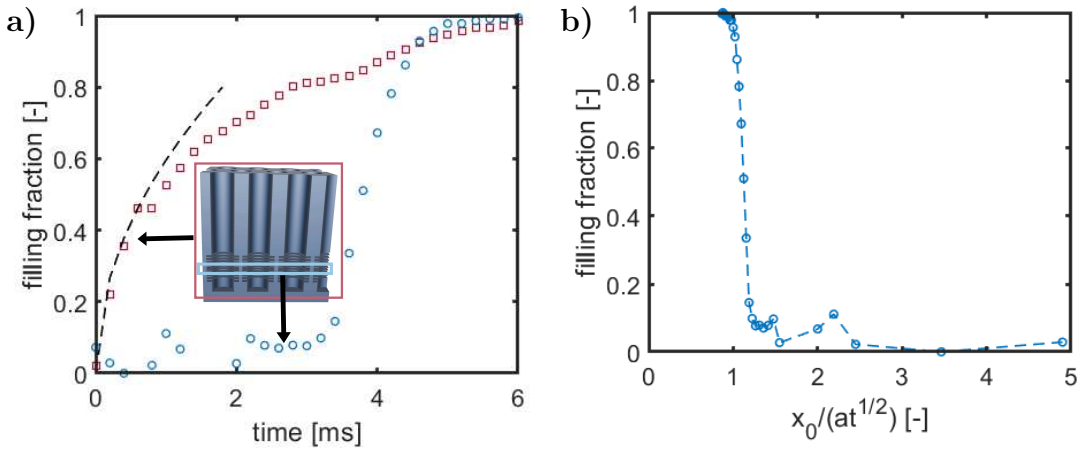

Figure 5.5: Dynamic white light spectroscopy during the imbibition of water in sample IV. a) Shows the filling of the overall stack (red squares) and PC (blue circles). The black dashed line is calculated by the constriction model. b) Spatio-temporal rescaling of the PC curve by the prefactor a of the Lucas-Washburn equation, displaying the fluid front shape.

studied *Vycor*, yet exhibits a higher degree of anisotropy (chapter 4). The subsequent exploration involves examining the drying dynamics of porous silicon through various height positions of a PC to elucidate the drying mechanism. A primary research question investigates whether drying occurs at an individual pore level or in a network-like fashion. Additionally, the study seeks to determine the influence of the PC on drying behavior.

Fig. 5.6 presents an optical microscopy experiment that illustrates macroscopic phenomena throughout the drying process. The sequence commences with complete saturation leading to bulk condensation at stage a). Initial formation of small droplets is observed on the surface, gradually covering it entirely. Drying is initiated by a directly applied nitrogen stream, resulting in a uniform recession of the bulk water film, while the pores remain largely filled as depicted in stage b). Upon the disappearance of bulk water, the porous layer begins to empty its contents, shown in stage c). The main origin of the colored appearance is the PC, that efficiently reflects light within its band width. Water filled parts appear green under polarized light, whereas air filled ones are magenta. Interestingly the sample does not appear to go through the color palette of visible light homogeneously. Instead a coexistence of green and magenta is observed in d). The green parts then start to disappear until the sample reaches a clear magenta.

Dynamic spectroscopy drying experiments are conducted using samples I and IV. Based on the water sorption isotherms (section 5.3), these samples offer optimal comparability. Similar to the previous analysis on capillary filling, the white light spectroscopy analysis is divided into global and local filling. The former is obtained

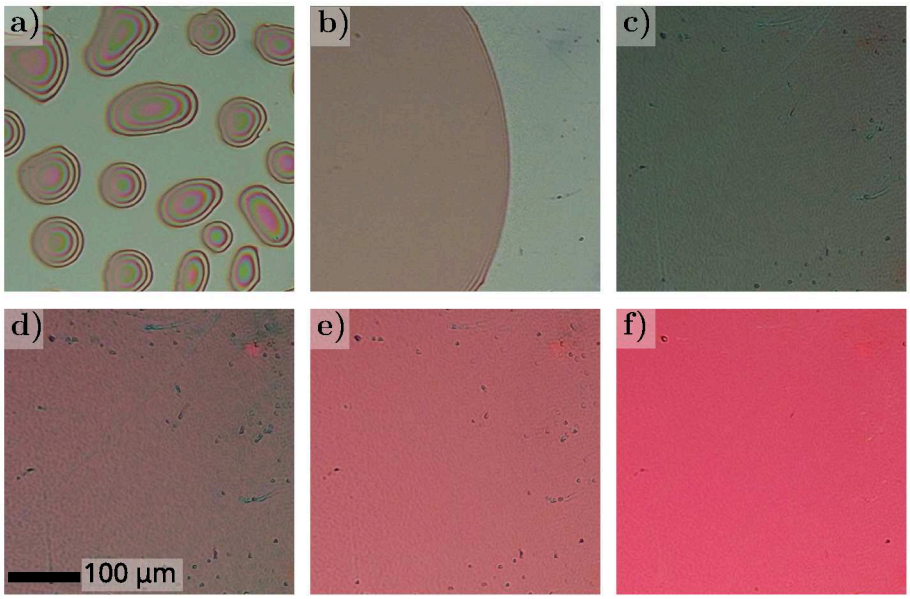

Figure 5.6: Light microscopy with polarization filter, during a) the onset of bulk condensation b) bulk film recession c)-f) drying at 2 s intervals. Vapor and nitrogen streams of 1000 ml/min are applied directly using an open sample cell.

from FFT of the spectra from 1000 – 1600 nm. Details regarding the FFT are specified in section 4.2. Notably, using a small window size ($\approx 2\,\mu m$) for determining the center of gravity around the peak with the highest effective optical thickness (EOT), which corresponds to the overall porous layer, proves to be more robust than employing a wider window encompassing the entire peak width. This window must be sufficiently large to accurately track the changes in EOT over time. The discontinuities in the peak width cannot be definitively attributed. The FFT analysis of the PC does not appear as a homogeneous layer when it is partially filled, e.g. when the drying or wetting front is encountered. While the EOT of a homogeneous layer exhibits changes in a single direction due to the refractive index differential of an infiltrate, the EOT of the PC displays both positive and negative fluctuations. In homogeneous filling states, the PC manifests an EOT peak across its full extent in FFT, akin to a homogeneous porous layer.

Fig. 5.7 presents the overall drying curves of sample I and IV under a dry nitrogen supply rate of 200, 400 and 800 ml/min. It should be noted that the gas stream passes through a premixing chamber with a small connection to the main sample cell, which is fitted with a long, narrow outlet pipe. As a result, only an indirect stream reaches the sample. Samples are fully saturated prior to measurement, thereby allowing bulk condensation on the surface. To ensure consistent initial conditions for the drying curves, i.e., removal of all bulk water, the onset is determined by identifying a numerical threshold in the forward differences of 30 consecutive points and then calculating back to the point of initial change. The total drying time aligns with the supply rates and agrees well for both samples,

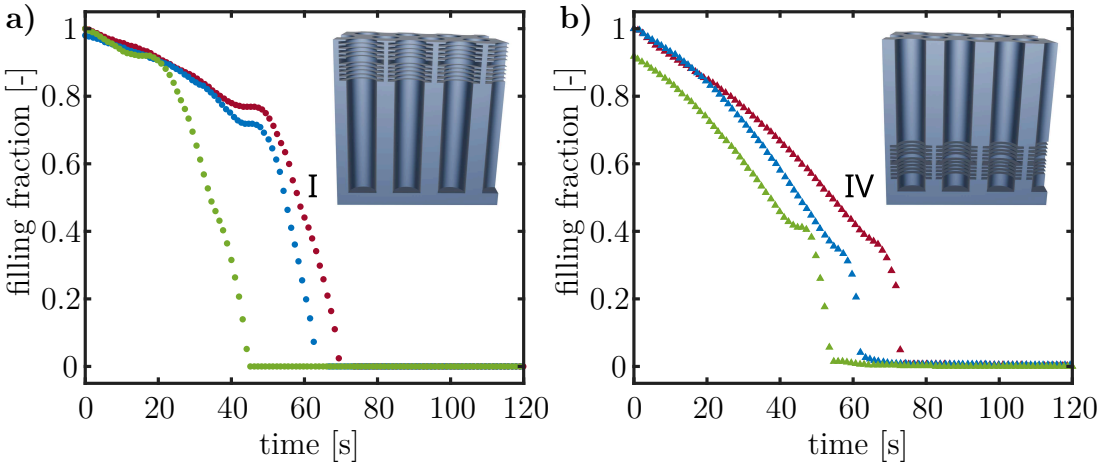

Figure 5.7: NIR analysis of dynamic spectroscopy during drying. The filling fractions correspond to the EOT of the overall porous layer stack. Red, blue and green symbols are linked to the nitrogen supply rates 200, 400 and 800 ml/min, respectively. a) drying of sample I b) drying of sample IV.

indicating that the drying rate can be effectively modulated by adjusting the supply rate.

Sample I in Fig. 5.7 exhibits a gradual decrease in saturation for the 200 and 400 ml/min up to a filling fraction just below 0.8, which fits to the volume fraction of the PC. Subsequently, the drying process significantly accelerates. In b), the drying initially progresses slowly until the filling fraction reaches 0.4, where a steeper decline is observed compared to the initial region in part a). This initial phase corresponds to the homogeneous layer within sample IV. The rate change, coinciding with the PC, increases thereafter. Although a meniscus recession coupled with a drying front could explain the distinct separation of regions with varying porosity, this does not align with the drying curves at an increased supply rate of 800 ml/min, where the rate change onset occurs at a higher filling fraction.
Examining the drying curves of the PC (Fig. 5.8 a) and b)) reveals a clear agreement of the curves. Even though the PC is located at different heights within the respective sample, there is no quantifiable delay between the overall start of the drying given a scan rate 100 ms. This shows a very fast in depth drying of the sample with a macroscopically homogeneous saturation. Cavitation or percolation are drying mechanisms typically describing this phenomenon.
In comparing the overall filling curves (Fig. 5.7) with localized measurements (Fig. 5.8), the atypical shape of the former stands out. Employing numerical central differences in tandem with quadratic regression, the *gradient*, and *loess* Matlab functions facilitate deriving the filling-fraction-dependent drying rate, as shown in (Fig. 5.8 c). In conjunction with simulations on pore network drying, four principal stages emerge.[128, 129] These stages are highlighted along the drying curve for sample I at a nitrogen supply rate of 200 ml/min in a) and c). First, a variable rate initiation

region due to invasion percolation is observed, until separated wet and dry clusters are established (1). This is followed by a constant rate (2), where the main transport originates from liquid clusters ranging from the pore tips to the free surface or just below if already a dry region is established. At stage (3) the drying rate falls moderately, which is usually related to a receding front of the liquid phase and decay of liquid clusters into smaller ones disconnected from the free surface. The drying rate becomes limited by vapor phase transport through a dry region below the free surface. This slow down of dynamics is here less perfect than in literature, which seems to be related to the pore morphology of the PC. Stage (4) consists in a fast falling rate, where only vapor transport takes place. In conclusion, the drying profile demonstrates strong alignment with percolation theory [128, 129] for the PC.

The overall fractional drying rate courses of sample I and IV (Fig 5.9) are segregated into three segments. A high but rapidly falling rate in the beginning (A), with the only exception of sample I at a supply rate of 800 ml/min, succeeded by a mostly constant rate over most of the filling fraction (B) and a sharp rate decrease at very low filling fractions. The most significant deviations between samples occur within outlined sections, attributable to the PC's influence and placement. For instance, the valley within the demarcated area for sample I with 200 ml/min corresponds to the initial 40 s for the drying curve in Fig. 5.7 a) and the constant rate region of the PC (Fig. 5.8 c) 2). Evidently, the PC impacts the initial drying rate significantly in sample I and is in total 10 seconds faster compared to the same supply rate for sample IV. A swift formation of a dry zone could explain this discrepancy. Such formation may also explain the inverted initial contour for sample I at 800 ml/min. Besides this measurement, the overall drying time reduces linearly with the supply rate. In general, it appears that the influence of the PC on the drying rate is more spread out and less pronounced, if it is located at a larger distance from the free surface.

The drying process of porous media is a highly intricate phenomenon and is often modeled using molecular dynamics simulations or pore network models. Theoretical approaches typically necessitate substantial simplifications to manage complexity. Here, the drying process is elucidated from a phenomenological perspective. Drying occurs due to a gradient of relative humidity, which may exist within the pore space or externally between the sample's free surface and the environment. Water molecules inside a porous material can be transported either by vapor diffusion, in regions where the liquid phase is already substituted, or by capillary transport of the liquid phase. Research on *Vycor* has shown that the vapor flux inside a porous layer due to a relative humidity gradient is negligible compared to external vapor transport.[127]

$$\langle s \rangle = \frac{p}{\sqrt{2}\pi d^2 \mathrm{k_B} T} \tag{5.2}$$

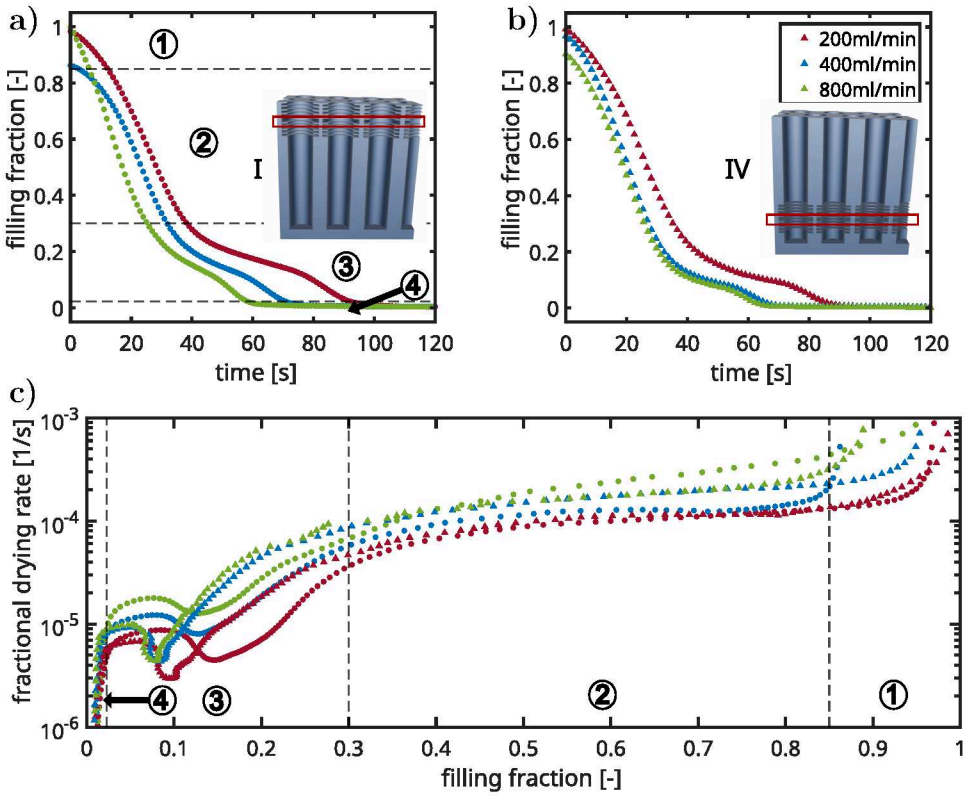

Figure 5.8: Dynamic white light spectroscopy during drying. The filling fractions correspond to the normalized resonance shift of the PC. Red, blue and green symbols are linked to the nitrogen supply rates 200, 400 and 800 ml/min, respectively. a) drying of sample I b) drying of sample IV c) drying rate versus filling fraction of samples I (dots) and IV (triangles). The dashed lines delineate drying regions of the 200 ml/min measurement of sample I in a) and c).

$$\mathrm{D_{Kn}} = \frac{r_\mathrm{h}}{6}\sqrt{\frac{8\mathrm{R}T}{\pi\mathrm{M}}} \tag{5.3}$$

The *Knudsen* number (Eq. 2.68) for vapor in the PSi samples approximates 5, based on a mean free path of 90 nm for vapor at 298 K (Eq. 5.2).[130]. Consequently, diffusion inside the pore space is governed by molecule-wall collisions, which is described by *Knudsen* diffusion (Eq. 5.3), where $r_\mathrm{h} = 4.8\,\mathrm{nm}$ is the hydraulic pore radius, R the ideal gas constant, $T = 298\,\mathrm{K}$ the temperature, M is the molecular mass. The diffusion constant $\mathrm{D_{Kn}}$ is accordingly $1.9 \cdot 10^{-6}\,\mathrm{m^2/s}$. In comparison, the coefficient for capillary imbibition of water in the previous subsection is $3.6 \cdot 10^{-8}\mathrm{m^2/s}$. Even if one assumes the same apparent radius of $4.9 \cdot 10^{-10}\,\mathrm{m^2/s}$, the diffusion coefficient in the *Knudsen*-regime would be one order higher ($\mathrm{D_{Kn}} = 1.9 \cdot 10^{-7}\,\mathrm{m^2/s}$), than the liquid transport. The measured total drying times between 45 and 75 seconds are much longer than to expect from the to this

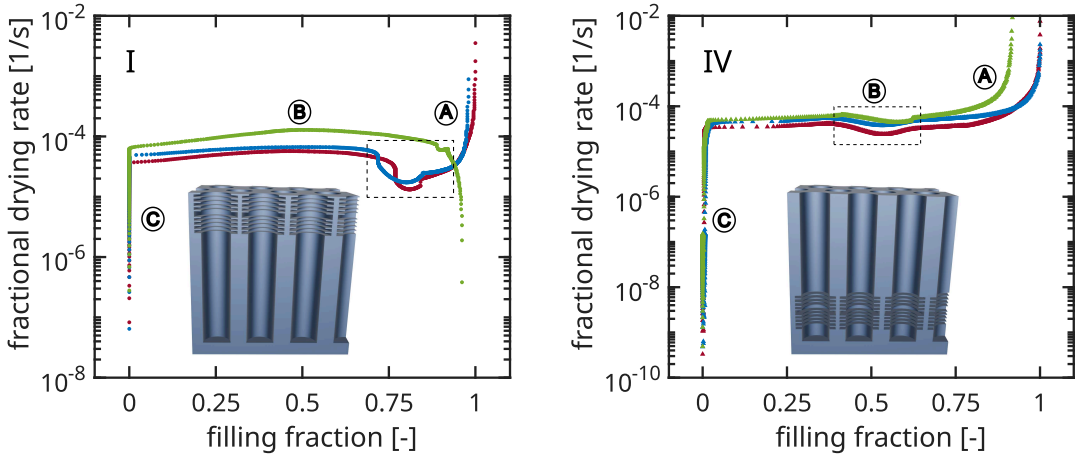

Figure 5.9: Drying rates over the entire porous layer of samples I and IV, with the nitrogen supply rates of 200, 400 and 800 ml/min in red blue and green, respectively.

point considered transport coefficients. A simple approximation of L^2/t_{tot} gives a range of $3-5\cdot10^{-12}\,\mathrm{m}^2/\mathrm{s}$. But, the measured overall drying curves in Fig. 5.7 do not strictly adhere to a square-root-time dependence. Assuming exclusively *Knudsen* diffusion oversimplifies the issue. In fact, vapor phase conduction, influenced by local saturation gradients, typically proceeds slower than liquid phase transport. These insights lead to the conclusion that drying mechanisms cannot be segregated into purely capillary-driven or vapor-phase transport regimes. Rather, a complex interplay exists between the two, where the liquid phase potentially acts as an impediment. Liquid bridges lacking connection to the free surface particularly hinder transport, supporting the notion of percolative drying.
There exists an analytical solution for drying in porous media [131], recently applied to cellulose fibers drying [132] and suggested for use with *Vycor* [127]. This solution is deemed elaborate given the system's complexity. Finite element modeling [127] or percolation modeling [133] serve as both effective and compatible methods for modeling the measured drying curves, yet lie beyond the scope of this study.

5.5 Conclusion

In this tripartite study, water sorption isotherms, capillary imbibition and drying of mesoporous silicon are investigated. The CLRS design, when combined with spectrometric techniques, reaches a time resolution ranging from hours for isotherm studies to microseconds during imbibition experiments, delivering global and local information. The cell used for sorption isotherms and drying resembles open environmental cells from spectral ellipsometry setups, characterized by a defined exhaust rather than being gas-tight.
Water sorption isotherms are effectively analyzed through the total effective optical

thickness (EOT) of the porous layer, derived using the FFT of interference patterns detected in the near-infrared region. Concurrently, the PC resonance is observed within the visible light spectrum. The water sorption isotherms, identified as type V, indicate stronger intermolecular interactions among water molecules than between water and the adsorbents. Notably, the hysteresis loops in both the central cavity and homogeneous layers are well-differentiated, enabling the identification of characteristic points. These loops are classified as type H1, typical of weakly interconnected pores with larger constrictions along the main pore axis. In agreement, no steps are observed in the hysteresis profiles, in contrast to previously reported ink bottle-shaped pores.[26] Calculations with the *Kelvin* equation, using the onset and maximum pressure of the hysteresis are used to approximate the hydraulic radius and streamline tortuosity based on the constriction model to 4.8 nm and 2.2, respectively.
In capillary imbibtion experiments a coefficient of $3.6 \cdot 10^{-8}\mathrm{m}^2/\mathrm{s}$ and a hydraulic radius of 3.1 nm are determined for the homogeneous porous layer preceding the PC. The discrepancy between this and the pore size from the isotherms partly results from the latter's inclusion of the PC region, which incorporates layers with larger pore radii. A flat fluid front shape is calculated from spatio-temporal rescaling of data from PC and global thin film interference measurements, suggesting an additional water layer of 0.19 nm ahead of the main fluid meniscus.
The drying of mesoporous silicon is influenced by external humidity gradients, proceeding slower than predicted by capillary transport or *Knudsen* diffusion. Drying rates show typical stages of percolative drying. There is also no splitting of EOT peaks in the FFT, which is reported for cavitation in mesoporous silicon.[27] Furthermore, the PC analysis indicates consistent drying rate stages across different height positions, lacking significant delays.
There are some improvements on the sample design, that are picked on during the analysis. If a PC is dividing a porous layer into two parts, these should be of significantly different physical thickness, ensuring that the EOT peaks do not overlap in FFT analysis. It should also be accounted for different filling states of the layers and the width of the peaks. Additionally, the layers should exceed the PC in thickness. The *orthogonal Maxwell Garnett* EMA serves as a straightforward predictive method for EOTs. For the samples synthesized here, one *Bragg* layer is of the same pore radius as the homogeneous layers. It can be ensured that the PC does not act as a constriction for a subsequent porous layer, by choosing a higher pore radius for all layers of the *Bragg* stack.
Overall, the material design of optical microcavity and *Fabry-Perót* layers, coupled with light spectroscopy, offers significant insights into nanoscale structure and dynamics. The temporal resolution of the described setup suggests potential applications in measuring sorption process relaxation times in future studies, which could elucidate the interactions between pore morphology and diffusion.[134] This study concludes that mesoporous silicon's pore structure is defined by constricted tubes aligned in the etching direction, with smaller interconnections relative to

constrictions. While interconnections minimally impact capillary filling, they significantly influence sorption isotherms and drying dynamics.

6 Synopsis

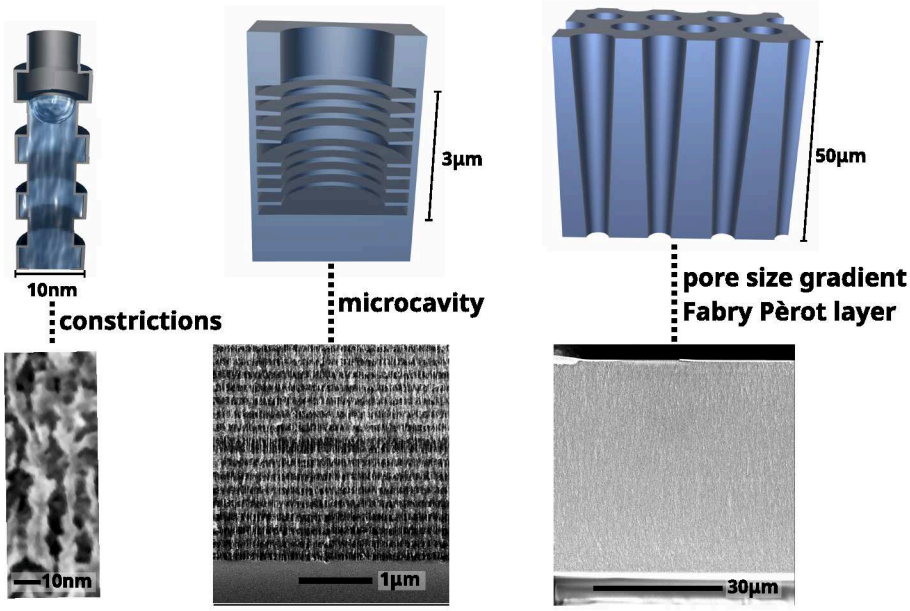

Figure 6.1: Mesoporous silicon at different scales in SEM (bottom) and the respective physical models (top).

This thesis explores white light reflection spectroscopy on mesoporous silicon and is divided into three distinct sections. Two sections focus on a *chip-like reflective sensor* (CLRS) that is optimized for capillary imbibition and sorption experiments, respectively. The third section examines the reconstruction of pore radius evolution from capillary imbibition dynamics in membranes, termed the *inverse problem of capillary filling*. This problem involves reversing the typical question regarding imbibition dynamics, usually addressed by known pressure and pore radius variations.

The CLRS, introduced here, enables the analysis of fluid dynamics within mesopores with remarkable spatial and temporal precision when used with modern, portable white light spectrometers. These spectrometers offer a spectral range from $200 - 1650\,\mathrm{nm}$ and enable scan rates down to microseconds. At $\approx 100\,\mu\mathrm{s}$ interference fringes of mesoporous silicon up to a thickness of about $100\,\mu\mathrm{m}$ are still well resolved. The CLRS is composed of homogeneous porous layers (*Fabry-Perót* layers) and a one-dimensional photonic crystal (PC). The PC is a compact microcavity, approximately $3\,\mu\mathrm{m}$ in thickness. Air substitution at the central cavity

is indicated by a shift in resonance wavelength, while the NIR region captures interference of the *Fabry-Perót* layers. The effective optical thickness of the layers is analyzed via FFT, facilitating simultaneous evaluation of both overall and local fluid filling dynamics.

Typically, observing transport phenomena of polymeric liquids in nanopores requires complex methods, such as polymer melt freezing and investigation through scanning electron microscopy in conjunction with energy dispersive X-ray spectroscopy or X-ray tomography.[15, 16] Unlike these ex-situ techniques, the CLRS presented here allows in-situ assessment of fluid dynamics. For liquid investigation, the *Fabry-Perót* layer is followed by the PC. Porosity and layer thickness are determined through static effective optical thickness measurements in both air and liquid-filled states using the *orthogonal Maxwell-Garnett* effective medium approximation.[63] A comparative study of a styrene dimer and pentamer demonstrates the importance of both global and local filling dynamic information. In the central cavity, dynamics reveal two distinct regimes for the pentamer and one for the dimer. These dynamics, when rescaled according to the kinetics in the preceding *Fabry-Perót* layer, illustrate fluid front shapes, showing a precursor film for the pentamer. By graphical determination, this precursor film exhibits a diffusion-like coefficient of $4 \cdot 10^{-12}\,\mathrm{m}^2/\mathrm{s}$ and a thickness of 0.5 nm. Moreover, a *constriction model* with inclusion of an immobile layer describing the capillary filling of a homogeneous PSi layer is applied. Without relying on tortuosity, slower dynamics than predicted by the *Lucas-Washburn* law are explained by the ratio of statistical segment radii. This elucidates small apparent radii derived from the *Lucas-Washburn* law using bulk fluid parameters. Applying the *constriction model*, immobile layers of 1.37 nm and 1.55 nm are calculated for the dimer and pentamer, respectively.[31, 33]

For water sorption experiments, the PC is positioned at varied distances from the free surface within the mesoporous layer, maintaining a constant sample volume. Thermal oxidation is applied to the surface. Reflective spectroscopy, with the addition of a humidity cell, monitors saturation analogous to the liquid imbibition approach. This study encompasses equilibrium sorption isotherms, drying, and capillary imbibition experiments, spanning temporal resolutions from hours to microseconds. Vapor phase transport processes reveal collective phenomena attributed to percolation within the porous samples.[127] This might seem contrary to the liquid phase capillary transport, modeled throughout this thesis as utilizing a representative pore for the entire array. The explanation lies in the constriction sizes along the main pore axis being larger on average than smaller, less frequent lateral pore interconnections. For vapor phase transport, even fewer lateral constrictions than lateral interconnections suffice to impact the drying path. Capillary transport in the liquid phase is driven by the menisci at the fluid front, with long-term kinetics determined by increasing wall friction due to extended transport paths.

Finally, an analytical solution for the *inverse problem of capillary filling* is derived for volumetric pore filling fractions, following previous arguments.[39, 40] This solution applies to any experimental method assessing liquid volume or volume fraction uptake rather than imbibition front progress. It is restricted to laminar flow

and relies on the lubrication approximation, requiring subsequent measurement of dynamics from both pore extremities. This method systematically assesses different freestanding, mesoporous silicon membrane synthesis routes by utilizing thin film interference spectroscopy to measure 2-propanol imbibition dynamics. Spectra from fully air and 2-propanol-filled states are used to calculate layer thickness and porosity through the orthogonal *Maxwell-Garnett* effective medium approximation.[63] An algorithm unwrapping the phase of interference fringes from FFT analyzes liquid dynamics. Consistent with previous studies on capillary imbibition exceptionally small apparent radii result from analysis with the *Lucas-Washburn* law. These small apparent radii can be explained by the *constriction model*. Additionally, the *inverse problem of capillary filling* unveils the long range pore shape along the primary pore axis. Samples etched from p^{++} wafers under constant current show increasing radii in etching direction, while the inverse is observed for p^{+} wafers under this condition. Although the inclinations of the pore pathways seem incredible small given a linear progression from 2.5 nm to 4.2 nm over a length of 50 μm for a p^{++} membrane, the total imbibition time varies about 40 % depending on the infiltration direction. Pulsed etching of p^{+} wafers results in an almost cylindrical pore shape. In general, lower doping relates to slower filling dynamics, suggesting stronger constriction effects. A post-synthesis treatment, involving chemical surface oxidation and oxide dissolution by an aqueous hydrofluoric acid-ethanol dip, successfully removes these constrictions. Scanning electron microscopy and imbibition measurements confirm that a higher ethanol ratio more effectively eliminates dendric structures on pore walls, implying these cause constrictions. The pore walls remain largely preserved, revealing slightly meandering traces, which contradicts previous high tortuosity assumptions, supporting the constriction theory. Overall, the *inverse problem of capillary filling* is effective for resolving mesopore pathways non-destructively, surpassing previously required elaborate techniques. This approach facilitates swift synthesis condition evaluations and introduces new fluid transport design options. This leads to the conclusion that structures for tailored fluid flow, as demonstrated in simulations[83, 84] can soon be realized at the nanoscale.

This thesis investigates a material design cycle encompassing fluid dynamics, structural and optical aspects of mesoporous silicon. Fig. 6.1 highlights key structural scales for physical processes. Combining *Fabry-Perót* layers with an optical microcavity enhances fluid dynamics resolution spatially and temporally. A rescaling approach uncovers sub-nanometer precursor films. Additionally, pore size gradients resulting from varied synthesis conditions in mesoporous silicon membranes are assessed using thin film interference measurements. Exceptionally slow capillary imbibition in liquids is explained by a *constriction model*, attributed to dendritic silicon facets perpendicular to pore walls, removable via post-synthesis treatment. Optical water sorption and drying experiments reveal a collective process, indicating pore interconnectivity.

Bibliography

[1] R. Feynman, "There's plenty of room at the bottom," in Feynman and computation (CRC Press, 2018), pp. 63–76.

[2] T. Damhus, R. Hartshorn, and A. Hutton, "Nomenclature of inorganic chemistry: iupac recommendations 2005," Chemistry International (2005).

[3] S. Arshavsky-Graham, N. Massad-Ivanir, E. Segal, and S. Weiss, "Porous silicon-based photonic biosensors: current status and emerging applications," Analytical chemistry **91**, 441–467 (2018).

[4] M. K. Sahoo and P. Kale, "Restructured porous silicon for solar photovoltaic: a review," Microporous and Mesoporous Materials **289**, 109619 (2019).

[5] G. Dittrich, Electroactuation and electrochemical characterization of polypyrrole in porous scaffold materials, Master's thesis, Hamburg University of Technology, Sept. 2018.

[6] M. Brinker and P. Huber, "Wafer-scale electroactive nanoporous silicon: large and fully reversible electrochemo-mechanical actuation in aqueous electrolytes," Advanced materials **34**, 2105923 (2022).

[7] M. Brinker, G. Dittrich, C. Richert, P. Lakner, T. Krekeler, T. F. Keller, N. Huber, and P. Huber, "Giant electrochemical actuation in a nanoporous silicon-polypyrrole hybrid material," Science advances **6**, eaba1483 (2020).

[8] V. Lehmann and U. Gösele, "Porous silicon formation: a quantum wire effect," Applied Physics Letters **58**, 856–858 (1991).

[9] X. Zhang, Electrochemistry of silicon and its oxide (Kluwer, 2001).

[10] V. Lehmann, Electrochemistry of silicon: instrumentation, science, materials and applications (2002).

[11] M. J. Sailor, Porous silicon in practice (John Wiley & Sons, 2012).

[12] W. Sparreboom, A. van den Berg, and J. C. Eijkel, "Principles and applications of nanofluidic transport," Nature nanotechnology **4**, 713–720 (2009).

[13] J. Salonen, A. M. Kaukonen, J. Hirvonen, and V.-P. Lehto, "Mesoporous silicon in drug delivery applications," Journal of pharmaceutical sciences **97**, 632–653 (2008).

[14] M. Steinhart, J. H. Wendorff, A. Greiner, R. B. Wehrspohn, K. Nielsch, J. Schilling, J. Choi, and U. Gosele, "Polymer nanotubes by wetting of ordered porous templates," Science **296**, 1997–1997 (2002).

[15] F. Vazquez Luna, M. Gerstenberger, G. Dittrich, J. Martins de Souza e Silva, P. Huber, R. Wehrspohn, and M. Steinhart, "Statistical analysis of submicron x-ray tomography data on polymer imbibition into arrays of cylindrical nanopores," The Journal of Physical Chemistry C **125**, 26731–26743 (2021).

[16] F. Vazquez Luna, A. K. Maurya, J. Martins de Souza e Silva, G. Dittrich, T. Paul, D. Enke, P. Huber, R. Wehrspohn, and M. Steinhart, "Straight versus spongy: effect of tortuosity on polymer imbibition into nanoporous matrices assessed by segmentation-free analysis of 3d sample reconstructions," The Journal of Physical Chemistry C **126**, 12765–12779 (2022).

[17] L. W. Lake, "Enhanced oil recovery," (1989).

[18] J. Schoelkopf, P. A. Gane, C. J. Ridgway, and G. P. Matthews, "Practical observation of deviation from lucas–washburn scaling in porous media," Colloids and Surfaces A: Physicochemical and Engineering Aspects **206**, 445–454 (2002).

[19] M. Engel and B. Stühn, "In situ small angle x-ray scattering measurements of the filling process of polyisobutylene and poly-caprolactone in ion track etched polycarbonate nanopores," The Journal of chemical physics **132** (2010).

[20] S. Gruener, H. E. Hermes, B. Schillinger, S. U. Egelhaaf, and P. Huber, "Capillary rise dynamics of liquid hydrocarbons in mesoporous silica as explored by gravimetry, optical and neutron imaging: nano-rheology and determination of pore size distributions from the shape of imbibition fronts," Colloids and Surfaces A: Physicochemical and Engineering Aspects **496**, 13–27 (2016).

[21] J. Sanchez, L. Dammann, L. Gallardo, Z. Li, M. Fröba, R. H. Meißner, H. A. Stone, and P. Huber, "Deformation dynamics of nanopores upon water imbibition," Proceedings of the National Academy of Sciences **121**, e2318386121 (2024).

[22] S. Gruener, Z. Sadjadi, H. E. Hermes, A. V. Kityk, K. Knorr, S. U. Egelhaaf, H. Rieger, and P. Huber, "Anomalous front broadening during spontaneous imbibition in a matrix with elongated pores," Proceedings of the National Academy of Sciences **109**, 10245–10250 (2012).

[23] A. Janshoff, K.-P. S. Dancil, C. Steinem, D. P. Greiner, V. S.-Y. Lin, C. Gurtner, K. Motesharei, M. J. Sailor, and M. R. Ghadiri, "Macroporous p-type silicon fabry- perot layers. fabrication, characterization, and applications in biosensing," Journal of the American Chemical Society **120**, 12108–12116 (1998).

[24] E. J. Anglin, M. P. Schwartz, V. P. Ng, L. A. Perelman, and M. J. Sailor, "Engineering the chemistry and nanostructure of porous silicon fabry-pérot films for loading and release of a steroid," Langmuir **20**, 11264–11269 (2004).

[25] K. M. van Delft, J. C. Eijkel, D. Mijatovic, T. S. Druzhinina, H. Rathgen, N. R. Tas, A. van den Berg, and F. Mugele, "Micromachined fabry- pérot interferometer with embedded nanochannels for nanoscale fluid dynamics," Nano letters **7**, 345–350 (2007).

[26] F. Casanova, C. E. Chiang, A. M. Ruminski, M. J. Sailor, and I. K. Schuller, "Controlling the role of nanopore morphology in capillary condensation," Langmuir **28**, 6832–6838 (2012).

[27] M. Bossert, A. Grosman, I. Trimaille, F. Souris, V. Doebele, A. Benoit-Gonin, L. Cagnon, P. Spathis, P.-E. Wolf, and E. Rolley, "Evaporation process in porous silicon: cavitation vs pore blocking," Langmuir **37**, 14419–14428 (2021).

[28] L. G. Cencha, R. Urteaga, and C. L. Berli, "Interferometric technique to determine the dynamics of polymeric fluids under strong confinement," Macromolecules **51**, 8721–8728 (2018).

[29] F. Liu, B. Dong, X. Liu, Y. Zheng, and J. Zi, "Structural color change in longhorn beetles tmesisternus isabellae," Optics express **17**, 16183–16191 (2009).

[30] H.-b. Seo and S.-Y. Lee, "Bio-inspired colorimetric film based on hygroscopic coloration of longhorn beetles (tmesisternus isabellae)," Scientific reports **7**, 44927 (2017).

[31] L. G. Cencha, G. Dittrich, P. Huber, C. L. Berli, and R. Urteaga, "Precursor film spreading during liquid imbibition in nanoporous photonic crystals," Physical review letters **125**, 234502 (2020).

[32] S. Chibbaro, L. Biferale, F. Diotallevi, S. Succi, K. Binder, D. Dimitrov, A. Milchev, S. Girardo, and D. Pisignano, "Evidence of thin-film precursors formation in hydrokinetic and atomistic simulations of nano-channel capillary filling," Europhysics Letters **84**, 44003 (2008).

[33] G. Dittrich, L. G. Cencha, M. Steinhart, R. B. Wehrspohn, C. L. Berli, R. Urteaga, and P. Huber, "Polymeric liquids in mesoporous photonic structures: from precursor film spreading to imbibition dynamics at the nanoscale," The Journal of Chemical Physics **160** (2024).

[34] J. Zhang, J. Lei, W. Tian, G. Zhang, G. Floudas, and J. Zhou, "Capillary filling of polymer chains in nanopores," Macromolecules **56**, 2258–2267 (2023).

[35] E. W. Washburn, "The dynamics of capillary flow," Physical review **17**, 273 (1921).

[36] H. Darcy, Les fontaines publiques de la ville de dijon: exposition et application des principes à suivre et des formules à employer dans les questions de distribution d'eau, Vol. 1 (Victor dalmont, 1856).

[37] Y. Yao, H.-J. Butt, G. Floudas, J. Zhou, and M. Doi, "Theory on capillary filling of polymer melts in nanopores," Macromolecular rapid communications **39**, 1800087 (2018).

[38] M. Reyssat, L. Courbin, E. Reyssat, and H. A. Stone, "Imbibition in geometries with axial variations," Journal of Fluid Mechanics **615**, 335–344 (2008).

[39] E. Elizalde, R. Urteaga, R. R. Koropecki, and C. L. Berli, "Inverse problem of capillary filling," Physical review letters **112**, 134502 (2014).

[40] S. Khatoon, J. Phirani, and S. S. Bahga, "An analytical solution of the inverse problem of capillary imbibition," Physics of Fluids **32** (2020).

[41] V. Lehmann, R. Stengl, and A. Luigart, "On the morphology and the electrochemical formation mechanism of mesoporous silicon," Materials Science and Engineering: B **69**, 11–22 (2000).

[42] C. Romanitan, P. Varasteanu, D. C. Culita, A. Bujor, and O. Tutunaru, "X-ray scattering profiles: revealing the porosity gradient in porous silicon," Journal of Applied Crystallography **54**, 847–855 (2021).

[43] M. Thelen, N. Bochud, M. Brinker, C. Prada, and P. Huber, "Laser-excited elastic guided waves reveal the complex mechanics of nanoporous silicon," Nature communications **12**, 3597 (2021).

[44] M. Grundmann, Physics of semiconductors, Vol. 11 (Springer, 2010).

[45] M. A. Hopcroft, W. D. Nix, and T. W. Kenny, "What is the young's modulus of silicon?" Journal of microelectromechanical systems **19**, 229–238 (2010).

[46] S. Hunklinger and C. Enss, Solid state physics (Walter de Gruyter GmbH & Co KG, 2022).

[47] R. Gross and A. Marx, Festkörperphysik (Oldenbourg Wissenschaftsverlag Verlag, 2012).

[48] M. Fox, Optical properties of solids, Vol. 3 (Oxford university press, 2010).

[49] N. W. Ashcroft and N. Mermin, Solid state physics 4th edition (Oldenbourg Verlag, 1976).

[50] G. Dittrich, Electropolymerisation of pyrrole in nanoporous silicon, Bachelor's thesis, Hamburg University, Mar. 2016.

[51] P. Allongue, V. Costa-Kieling, and H. Gerischer, "Etching of silicon in naoh solutions: ii. electrochemical studies of n-si (111) and (100) and mechanism of the dissolution," Journal of the Electrochemical Society **140**, 1018 (1993).

[52] J. O. Bockris, R. E. White, C. Vayenas, and M. Gamboa-Aldeco, Modern aspects of electrochemistry: volume 39, Vol. 39 (Springer Science & Business Media, 2006).

[53] R. P. Feynman, Feynman lectures on physics (Basic Books, 2010).

[54] L. N. Acquaroli, R. Urteaga, C. L. Berli, and R. R. Koropecki, "Capillary filling in nanostructured porous silicon," Langmuir **27**, 2067–2072 (2011).

[55] R. Urteaga, L. N. Acquaroli, R. R. Koropecki, A. Santos, M. Alba, J. Pallarès, L. F. Marsal, and C. L. Berli, "Optofluidic characterization of nanoporous membranes," Langmuir **29**, 2784–2789 (2013).

[56] L. G. Cencha, P. Huber, M. Kappl, G. Floudas, M. Steinhart, C. L. A. Berli, and R. Urteaga, "Nondestructive high-throughput screening of nanopore geometry in porous membranes by imbibition SUPPLEMTENT," Applied Physics Letters **115**, 113701 (2019).

[57] M. Quinten, A practical guide to optical metrology for thin films (John Wiley & Sons, 2012).

[58] M. Quinten, "On the use of fast fourier transform for optical layer thickness determination," SN Applied Sciences **1**, 823 (2019).

[59] T. Galy, M. Marszewski, S. King, Y. Yan, S. H. Tolbert, and L. Pilon, "Comparing methods for measuring thickness, refractive index, and porosity of mesoporous thin films," Microporous and Mesoporous Materials **291**, 109677 (2020).

[60] W. Theiβ, S. Henkel, and M. Arntzen, "Connecting microscopic and macroscopic properties of porous media: choosing appropriate effective medium concepts," Thin Solid Films **255**, 177–180 (1995).

[61] W. Theiß, "Optical properties of porous silicon," Surface Science Reports **29**, 91–192 (1997).

[62] A. H. Sihvola, Electromagnetic mixing formulas and applications, 47 (Iet, 1999).

[63] J. Brandt, G. Dittrich, M. Thelen, H. Renner, P. Huber, M. Eich, and A. Petrov, "On the applicability of the maxwell garnett effective medium model to media with a high density of cylindrical pores," Optical Materials Express **14**, 871–879 (2024).

[64] V. A. Markel, "Introduction to the maxwell garnett approximation: tutorial," JOSA A **33**, 1244–1256 (2016).

[65] D. Jalas, R. Canchi, A. Y. Petrov, S. Lang, L. Shao, J. Weissmüller, and M. Eich, "Effective medium model for the spectral properties of nanoporous gold in the visible," Applied Physics Letters **105** (2014).

[66] L. D. Landau, J. S. Bell, M. Kearsley, L. Pitaevskii, E. Lifshitz, and J. Sykes, Electrodynamics of continuous media, Vol. 8 (elsevier, 2013).

[67] H. Karimian-Sarakhs and M. H. Neshati, "Comparative analysis of the effective permittivity of aligned cylindrical perforated substrate," in 2020 28th iranian conference on electrical engineering (icee) (IEEE, 2020), pp. 1–4.

[68] M. A. Green, "Self-consistent optical parameters of intrinsic silicon at 300 k including temperature coefficients," Solar Energy Materials and Solar Cells **92**, 1305–1310 (2008).

[69] P. E. Ciddor, "Refractive index of air: new equations for the visible and near infrared," Applied optics **35**, 1566–1573 (1996).

[70] B. E. Saleh and M. C. Teich, Optik und photonik (John Wiley & Sons, 2020).

[71] V. Torres-Costa and R. Martín-Palma, "Application of nanostructured porous silicon in the field of optics. a review," Journal of materials science **45**, 2823–2838 (2010).

[72] C. Pacholski, "Photonic crystal sensors based on porous silicon," Sensors **13**, 4694–4713 (2013).

[73] G. Lu, X.-D. Wang, and Y.-Y. Duan, "A critical review of dynamic wetting by complex fluids: from newtonian fluids to non-newtonian fluids and nanofluids," Advances in colloid and interface science **236**, 43–62 (2016).

[74] P.-G. De Gennes, "Wetting: statics and dynamics," Reviews of modern physics **57**, 827 (1985).

[75] P. De Laplace, "Mechanique celeste, supplement to book 10," Durat, Paris (1806).

[76] J. Kunes, Dimensionless physical quantities in science and engineering (Elsevier, 2012).

[77] S. VOGEL, "Life in moving fluid," Th Physical Biology of Flow (1994).

[78] R. Lucas, "Ueber das zeitgesetz des kapillaren aufstiegs von flüssigkeiten," Kolloid-Zeitschrift **23**, 15–22 (1918).

[79] K. Wu, Z. Chen, J. Li, X. Li, J. Xu, and X. Dong, "Wettability effect on nanoconfined water flow," Proceedings of the National Academy of Sciences **114**, 3358–3363 (2017).

[80] S. Gruener, D. Wallacher, S. Greulich, M. Busch, and P. Huber, "Hydraulic transport across hydrophilic and hydrophobic nanopores: flow experiments with water and n -hexane," Physical Review E **93**, 013102 (2016).

[81] S. Gruener and P. Huber, "Capillarity-driven oil flow in nanopores: darcy scale analysis of lucas–washburn imbibition dynamics," Transport in porous media **126**, 599–614 (2019).

[82] J. Cai, E. Perfect, C.-L. Cheng, and X. Hu, "Generalized modeling of spontaneous imbibition based on hagen–poiseuille flow in tortuous capillaries with variably shaped apertures," Langmuir **30**, 5142–5151 (2014).

[83] M. Iwamatsu, "Thermodynamics and hydrodynamics of spontaneous and forced imbibition in conical capillaries: a theoretical study of conical liquid diode," Physics of Fluids **34** (2022).

[84] M. Liu, S. Suo, J. Wu, Y. Gan, D. A. Hanaor, and C. Chen, "Tailoring porous media for controllable capillary flow," Journal of colloid and interface science **539**, 379–387 (2019).

[85] Z. Zhang, L. Wen, and L. Jiang, "Nanofluidics for osmotic energy conversion," Nature Reviews Materials **6**, 622–639 (2021).

[86] F. Dullien, M. El-Sayed, and V. Batra, "Rate of capillary rise in porous media with nonuniform pores," Journal of Colloid and Interface Science **60**, 497–506 (1977).

[87] R. Sharma and D. S. Ross, "Kinetics of liquid penetration into periodically constricted capillaries," Journal of the Chemical Society, Faraday Transactions **87**, 619 (1991).

[88] T. L. Staples and D. G. Shaffer, "Wicking flow in irregular capillaries," Colloids and Surfaces A: Physicochemical and Engineering Aspects **204**, 239–250 (2002).

[89] W.-B. Young, "Analysis of capillary flows in non-uniform cross-sectional capillaries," Colloids and Surfaces A: Physicochemical and Engineering Aspects **234**, 123–128 (2004).

[90] N. Franck, C. L. A. Berli, P. A. Kler, and R. Urteaga, "Multiphysics approach for fluid and charge transport in paper-based microfluidics," Microfluidics and Nanofluidics **26**, 10.1007/s10404-022-02590-8 (2022).

[91] C. L. A. Berli, M. Mercuri, and M. G. Bellino, "Modeling the abnormally slow infiltration rate in mesoporous films," Physical Chemistry Chemical Physics **19**, 1731–1734 (2017).

[92] D. Patro, S. Bhattacharyya, and V. Jayaram, "Flow kinetics in porous ceramics: understanding with non-uniform capillary models," Journal of the American Ceramic Society **90**, 3040–3046 (2007).

[93] S. Gruener, T. Hofmann, D. Wallacher, A. V. Kityk, and P. Huber, "Capillary rise of water in hydrophilic nanopores," Physical Review E—Statistical, Nonlinear, and Soft Matter Physics **79**, 067301 (2009).

[94] O. Vincent, A. Szenicer, and A. D. Stroock, "Capillarity-driven flows at the continuum limit," Soft Matter **12**, 6656–6661 (2016).

[95] P. W. Atkins and J. De Paula, Atkins' physical chemistry (Oxford university press, 2006).

[96] S. Gruener and P. Huber, "Knudsen diffusion in silicon nanochannels," Physical review letters **100**, 064502 (2008).

[97] S. Gregg and K. Sing, Adsorption, surface area and porosity (Academic Press, 1982).

[98] Z. Dobkowski, "Determination of critical molecular weight for entangled macromolecules using the tensile strength data," Rheologica acta **34**, 578–585 (1995).

[99] S. Wu, "Surface and interfacial tensions of polymer melts. ii. poly (methyl methacrylate), poly (n-butyl methacrylate), and polystyrene," The Journal of Physical Chemistry **74**, 632–638 (1970).

[100] W. Xu, K. Mihhels, N. Kotov, S. Lepikko, R. H. Ras, C. M. Johnson, T. Pettersson, and E. Kontturi, "Solid-state polymer adsorption for surface modification: the role of molecular weight," Journal of Colloid and Interface Science **605**, 441–450 (2022).

[101] E. R. Peck and K. Reeder, "Dispersion of air," JOSA **62**, 958–962 (1972).

[102] X. Zhang, J. Qiu, X. Li, J. Zhao, and L. Liu, "Complex refractive indices measurements of polymers in visible and near-infrared bands," Applied optics **59**, 2337–2344 (2020).

[103] J. H. Jensen and J. C. Kromann, The molecule calculator: a web application for fast quantum mechanics-based estimation of molecular properties, 2013.

[104] C.-H. Tu, J. Zhou, M. Doi, H.-J. Butt, and G. Floudas, "Interfacial interactions during in situ polymer imbibition in nanopores," Physical Review Letters **125**, 127802 (2020).

[105] S. A. Sukhishvili, Y. Chen, J. D. Müller, E. Gratton, K. S. Schweizer, and S. Granick, "Surface diffusion of poly (ethylene glycol)," Macromolecules **35**, 1776–1784 (2002).

[106] S. Huber, Optofluidic characterization of mesoporous silicon: a comparative study of nmr/white light spectroscopy and laser interferometry, Master's thesis, Hamburg University of Technology, Nov. 2022.

[107] I. Henins, "Precision density measurement of silicon," Journal of research of the National Bureau of Standards. Section A, Physics and chemistry **68**, 529 (1964).

[108] S. J. Ward and S. M. Weiss, "Reducing detection limits of porous silicon thin film optical sensors using signal processing," in Frontiers in biological detection: from nanosensors to systems xiii, Vol. 11662 (SPIE, 2021), pp. 37–45.

[109] M. Brinker, M. Thelen, M. May, D. Rings, T. Krekeler, P. Lakner, T. F. Keller, F. Bertram, N. Huber, and P. Huber, "How nanoporous silicon-polypyrrole hybrids flex their muscles in aqueous electrolytes: in operando high-resolution x-ray diffraction and electron tomography-based micromechanical computer simulations," Physical Review Materials **6**, 116002 (2022).

[110] T. M. Aminabhavi, M. I. Aralaguppi, S. B. Harogoppad, and R. H. Balundgi, "Densities, viscosities, refractive indices, and speeds of sound for methyl acetoacetate+ aliphatic alcohols (c1-c8)," Journal of Chemical and Engineering Data **38**, 31–39 (1993).

[111] B. C. Hoke Jr and J. C. Chen, "Binary aqueous-organic surface tension temperature dependence," Journal of Chemical and Engineering Data **36**, 322–326 (1991).

[112] S. Naumov, A. Khokhlov, R. Valiullin, J. Kärger, and P. A. Monson, "Understanding capillary condensation and hysteresis in porous silicon: network effects within independent pores," Physical Review E—Statistical, Nonlinear, and Soft Matter Physics **78**, 060601 (2008).

[113] P. Kumar, T. Hofmann, K. Knorr, P. Huber, P. Scheib, and P. Lemmens, "Tuning the pore wall morphology of mesoporous silicon from branchy to smooth, tubular by chemical treatment," Journal of Applied Physics **103** (2008).

[114] X.-y. Hou, H.-l. Fan, L. Xu, F.-l. Zhang, M.-q. Li, M.-r. Yu, and X. Wang, "Pulsed anodic etching: an effective method of preparing light-emitting porous silicon," Applied physics letters **68**, 2323–2325 (1996).

[115] R. Grover, K. Narasimhan, and D. Sharma, "Pulsed anodic anodisation of porous silicon films," Journal of Porous Materials **7**, 377–379 (2000).

[116] W. Hu, W. Zhao, J. Fan, S. Wu, and J. Zhang, "Emission properties of porous silicon electron emitters formed by pulsed anodic etching," Journal of Electronic Materials **46**, 895–902 (2017).

[117] G. X. Zhang, Porous silicon: morphology and formation mechanisms (Springer, 2006), pp. 65–133.

[118] E. Kikkinides, P. Monson, and R. Valiullin, "Sorption isotherm reconstruction and extraction of pore size distributions for serially connected pore model (scpm) structures employing algorithmic and statistical models," The Journal of Physical Chemistry C **124**, 21591–21607 (2020).

[119] M. Hayek, "On the inverse problem of capillary imbibition through nonuniform axial geometry," Physics of Fluids **36** (2024).

[120] M. Thommes, K. Kaneko, A. V. Neimark, J. P. Olivier, F. Rodriguez-Reinoso, J. Rouquerol, and K. S. Sing, "Physisorption of gases, with special reference to the evaluation of surface area and pore size distribution (iupac technical report)," Pure and applied chemistry **87**, 1051–1069 (2015).

[121] P. Education, "The columbia electronic encyclopedia 6th ed," Retrived August **2**, 2006 (2006).

[122] D. R. Lide, Crc handbook of chemistry and physics, Vol. 85 (CRC press, 2004).

[123] W. Saam and M. W. Cole, "Excitations and thermodynamics for liquid-helium films," Physical Review B **11**, 1086 (1975).

[124] W. Wagner and H.-J. Kretzschmar, "Iapws industrial formulation 1997 for the thermodynamic properties of water and steam," International steam tables: properties of water and steam based on the industrial formulation IAPWS-IF97, 7–150 (2008).

[125] D. R. Ceratti, M. Faustini, C. Sinturel, M. Vayer, V. Dahirel, M. Jardat, and D. Grosso, "Critical effect of pore characteristics on capillary infiltration in mesoporous films," Nanoscale **7**, 5371–5382 (2015).

[126] A. Alvarez-Herrero, H. Guerrero, E. Bernabeu, and D. Levy, "Analysis of nanostructured porous films by measurement of adsorption isotherms with optical fiber and ellipsometry," Applied Optics **41**, 6692–6701 (2002).

[127] B. Maillet, G. Dittrich, P. Huber, and P. Coussot, "Diffusionlike drying of a nanoporous solid as revealed by magnetic resonance imaging," Physical review applied **18**, 054027 (2022).

[128] Y. Le Bray and M. Prat, "Three-dimensional pore network simulation of drying in capillary porous media," International journal of heat and mass transfer **42**, 4207–4224 (1999).

[129] A. G. Yiotis, I. N. Tsimpanogiannis, A. K. Stubos, and Y. C. Yortsos, "Pore-network study of the characteristic periods in the drying of porous materials," Journal of colloid and interface science **297**, 738–748 (2006).

[130] J. Phattaranawik, R. Jiraratananon, and A. G. Fane, "Heat transport and membrane distillation coefficients in direct contact membrane distillation," Journal of membrane science **212**, 177–193 (2003).

[131] J. Crank, The mathematics of diffusion (Oxford university press, 1979).

[132] X. Ma, B. Maillet, L. Brochard, O. Pitois, R. Sidi-Boulenouar, and P. Coussot, "Vapor-sorption coupled diffusion in cellulose fiber pile revealed by magnetic resonance imaging," Physical Review Applied **17**, 024048 (2022).

[133] O. Maalal, M. Prat, and D. Lasseux, "Pore network model of drying with kelvin effect," Physics of Fluids **33** (2021).

[134] R. Valiullin, S. Naumov, P. Galvosas, J. Kärger, H.-J. Woo, F. Porcheron, and P. A. Monson, "Exploration of molecular dynamics during transient sorption of fluids in mesoporous materials," Nature **443**, 965–968 (2006).

[135] E. Haska, Water-based transparent display, Bachelor's thesis, Hamburg University of Technology, Oct. 2024.

[136] J. Novak, Benetzung und elektrobenetzung auf siliziumsubstraten unter kontrollierter atmosphäre mit wässrigen elektrolytlösungen, Bachelor's thesis, Hamburg University of Technology, Oct. 2018.

[137] P. T. Tchatchou, Wetting and electrowetting on porous silanized silicon, Master's thesis, Hamburg University of Technology, Oct. 2019.

[138] E. Nativ-Roth, K. Rechav, and Z. Porat, "Deposition of gold and silver on porous silicon and inside the pores," Thin Solid Films **603**, 88–96 (2016).

[139] J. Schultze and K. Jung, "Regular nanostructured systems formed electrochemically: deposition of electroactive polybithiophene into porous silicon," Electrochimica acta **40**, 1369–1383 (1995).

[140] S. Naser, Temperaturabhängige imbibitionsversuche mit komplexen flüssigkeiten an kontrolliert porösen gläsern, Bachelor's thesis, Hamburg University of Technology, May 2019.

[141] H. Kim, A. Rühm, L. Lurio, J. Basu, J. Lal, D. Lumma, S. Mochrie, and S. Sinha, "Surface dynamics of polymer films," Physical review letters **90**, 068302 (2003).

[142] G. C. Berry and T. G. Fox, "The viscosity of polymers and their concentrated solutions," in Fortschritte der hochpolymeren-forschung (Springer, 2006), pp. 261–357.

[143] M. L. Williams, R. F. Landel, and J. D. Ferry, "The temperature dependence of relaxation mechanisms in amorphous polymers and other glass-forming liquids," Journal of the American Chemical society **77**, 3701–3707 (1955).

[144] J. Brandrup, E. H. Immergut, E. A. Grulke, A. Abe, and D. R. Bloch, Polymer handbook, Vol. 89 (Wiley New York, 1999).

[145] Y. Yao, S. Alexandris, F. Henrich, G. Auernhammer, M. Steinhart, H.-J. Butt, and G. Floudas, "Complex dynamics of capillary imbibition of poly (ethylene oxide) melts in nanoporous alumina," The Journal of Chemical Physics **146** (2017).

[146] I. Hassan, Opto-fluidische experimente zur kapillarbefüllung von nanoporösen aluminiumoxidmembranen mit polystyrol, Master's thesis, Hamburg University of Technology, Nov. 2019.

[147] P. Stastny, Z. Chlup, P. Roupcova, and M. Trunec, "Thin high-strength zirconia tapes with extreme flexibility," Journal of Asian Ceramic Societies **9**, 964–974 (2021).

[148] A. De Greef, P. Lambert, and A. Delchambre, "Towards flexible medical instruments: review of flexible fluidic actuators," Precision engineering **33**, 311–321 (2009).

[149] M. Lazeroms, A. La Haye, W. Sjoerdsma, W. Schreurs, W. Jongkind, G. Honderd, and C. Grimbergen, "A hydraulic forceps with force-feedback for use in minimally invasive surgery," Mechatronics **6**, 437–446 (1996).

[150] S. Torquato, "Hyperuniform states of matter," Physics Reports **745**, 1–95 (2018).

A Addition: Inverse Problem of Capillary Filling

Fig. A.1 shows the top part of a p^{++}-membrane with the etching direction from left to right. The inverse problem solution is aligned with an SEM image. Its first outstanding peaks coincide with a change of regions that can be identified as structurally different in SEM. The brighter region on the left of the SEM image probably corresponds to a microporous layer, due to a higher doping density of the raw material at the surface.[11]

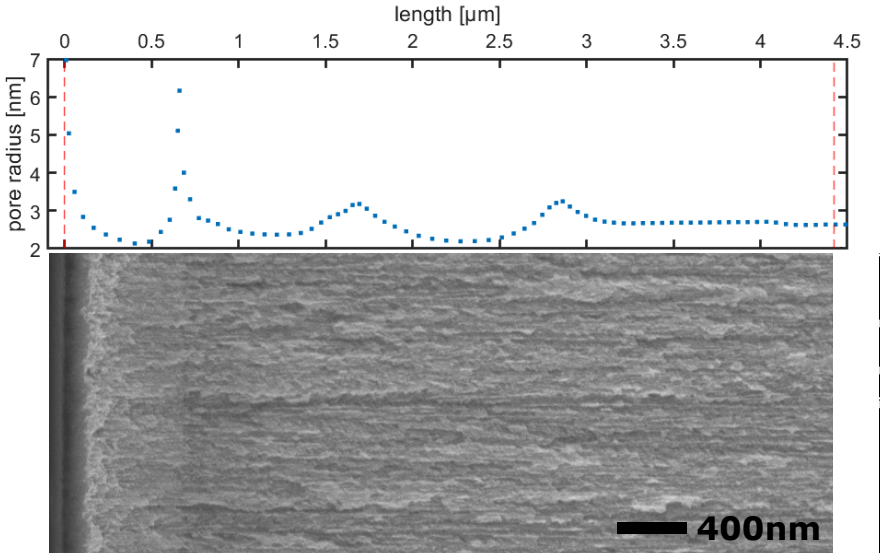

Figure A.1: Radius profile by the inverse problem and SEM image by a Zeiss Supra 55 VP (WD 2.1 mm, EHT 2 kV, aperture 20 µm) of a cross-section from a p^{++}-membrane. The dashed lines in red show the alignment of the SEM excerpt with the sample.

B Mesoporous Silicon Modification

B.1 Thermal Oxidation

Partial or complete oxidation of mesoporous silicon is often desired to render the material hydrophilic, enable secondary reactions like silanization, reduce the refractive index, or obtain a transparent material. The latter has caught interest for the application of smart windows. Its exploration is started in the *I^3-program* funded by the *Hamburg University of Technology*. When an entirely oxidized PSi membrane is saturated with water, it is transparent because of the closely matching refractive indices. During desorption of water by lowering the environmental humidity, the membrane dries inhomogeneously forming wet and dry clusters. Since these clusters are on the wavelength scale of visible light, the material shows strong scattering that appears opaque (Fig. B.1). Thick membranes ($\sim 200\,\mu m$) stay in the opaque state for several hours even under elevated dry air flows. Currently, the material is under investigation for application as transparent display by local laser heating.[135]

Figure B.1: Mesoporous glass that is transparent where saturated with water or opaque in a region partially dry blown.

PSi can be thermally oxidized under environmental air conditions. The degree of oxidation depends on the temperature and the application time. To cover the surface of PSi with a few oxide layers 673 K for 2 hours are sufficient. Because

of the mismatch of the crystal lattices of silicon dioxide and pure silicon, these first oxide layers apply a strong tension to the material. Freestanding membranes therefore often bend during the thermal oxidation. This bending can be especially pronounced if a heat, pore size, or thickness gradient is apparent. Thin membranes with a thickness of a few micrometers have the least resistance to such deformations. For complete oxidation temperatures above 928 K have to be applied, to finish the process within a few days. At lower temperatures, the oxidation slows down rapidly as a result of the slow diffusion of oxygen.
Here, a procedure to fully oxidize a PSi membrane is documented, with a low degree of mechanical deformation. It is noticed in several attempts that deviations from this procedure, like a different membrane thickness, etching procedure, heating rate, or absolute temperature, often alter the result significantly. PSi is prepared from a p^+ boron-doped silicon wafer (SIMAT, $0.01 - 0.02\,\mathrm{m\Omega/cm^2}$). It is etched by an aqueous HF(40 %)/EtOH solution (2/3 by volume) applying a constant current density of $12.5\,\mathrm{mA/cm^2}$. After an etching time of 266 min, a 200 µm thick mesoporous silicon layer attached to the bulk material is formed. The layer is lifted off by applying a current density of $225\,\mathrm{mA/cm^2}$ until a drop in the measured potential is observed, with the addition of 10 s. After rinsing and drying, the sample is oxidized at 1123 K for 40 h. During thermal oxidation with a rate of 10 K/min, crystalline silicon domains are preserved.[11] The cooling rate is limited to the same rate but actually carried out much slower, since cooling is passive. Fig. B.2 shows the result of the synthesis.

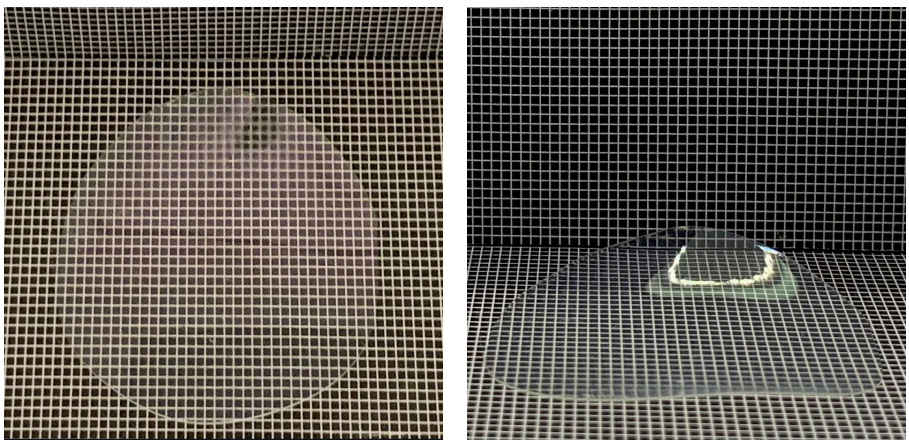

Figure B.2: Fully oxidized mesoporous silicon membrane in top and side view on millimeter paper.

B.2 Silanization

Silanization is the surface termination of silicon by hydrocarbon groups. The following outlines the procedure to modify mesoporous silicon with methyl groups.

For this modification a silicon oxide layer is required at the surface. In contrast to bulk silicon, as prepared PSi is hydrogen terminated at the surface of the pore walls. Therefore, it is oxidized first in a 30 % aqueous hydrogen-peroxide solution for $\approx$ 20 h. Other oxidation procedures are similarly suitable. Directly before the reaction the membrane is rinsed three time with trichlormethan, mostly displacing adsorbed water and dissolving organic residues. The reaction solution consists of a 1/9 volumetric ratio of dichlorodimethylsilane and trichloromethane. It is advisable to use a plastic beaker that is resistant to the chemicals, since laboratory glass ware would also get silanized. The sample is left for two hours in a covered beaker with the reaction solution. Afterwards the sample is rinsed by trichlormethan, followed by methanol until all residuals of the reaction solution are removed. Prolonged exposure with environmental humidity in combination with the reaction solution may induce reverse reactions. Therefore, the samples are dry blown by a nitrogen gun. Studies on wetting and electrowetting on as-prepared and silanized PSi can be found in [136] and [137], respectively.

C Direct Gold Deposition in Mesoporous Silicon

The interface of gold and n-doped silicon is known to have an electric *Schottky*-contact. Planar interfaces of this kind provide a junction capacitance because of bending of the electronic bands. This is often undesired, as it effectively is a high resistance junction. Scientists of the *Beuth University of Applied Sciences* came up with the idea to increase the interface of this junction to produce a high capacitance material. This is attempted by producing mesoporous, n-doped silicon and infiltrating the pore space with gold. Previous attempts of gold deposition in n-doped PSi, were unsuccessful due to pore clogging, limiting the penetration of gold to few hundreds of nanometers with high variance in the penetration depth.[138] Precipitation, sputtering, and reactions that occur solely through direct contact are often ineffective for achieving homogeneous infiltration of nanopores. Reactions that enable nucleation at the bottom of the pores are much more favorable. This is frequently illustrated by the electropolymerization of electroactive polymers within PSi. In this process, the increased electric field strength at the pore tips, combined with the lower conductivity of the pore walls, is leveraged to initiate nucleation at the pore bottom.[7, 139] Since the direct contact of silicon and gold is required no anchor materials are desired to link the materials. Instead cyanides have to be used for a stable gold solution usable during electrodeposition.

In the following the electrochemical deposition of gold in n-doped PSi is presented, filling porous layers on the micrometer scale (Fig. C.1). A commercial n-type silicon wafer doped with a doping density of $7 \cdot 10^{17} - 4 \cdot 10^{18}$ antimony/cm^3 is electrochmically etched. The etching procedure is conducted with a 8 % aqueous HF solution with 8 mmol potassium permanganate as additional oxidant. After a constant current application of 70 mA for an area of 7.84 cm^2 for 300 s an approximately 2 µm mesoporous layer is etched. For the gold deposition an aqueous 0.1 mol/l potassium dicyanoaurat is mixed with a 0.5 mol/l potassium carbonate solution, the latter is required to ensure that no hydrogen cyanide is released. For the deposition process a PTFE cell with an O-ring is clamped onto the porous silicon epilayer, leaving an area of 7 mm^2 exposed to the solution. PSi is the working electrode and a platinum mesh serves as the counter electrode. When the reaction solution is added to the cell, the open circuit potential (OCP) is recorded. It is waited until the OCP stabilized at -0.65 V. Subsequently, potentiostatic Au

deposition is initiated by applying −1 V for 1800 s. The deposition potential is determined by a prior linear sweep from the OCP to −1.5 V at a 10 mV/s scan rate on a separate part of the same sample, selecting the half-maximum of the current response.

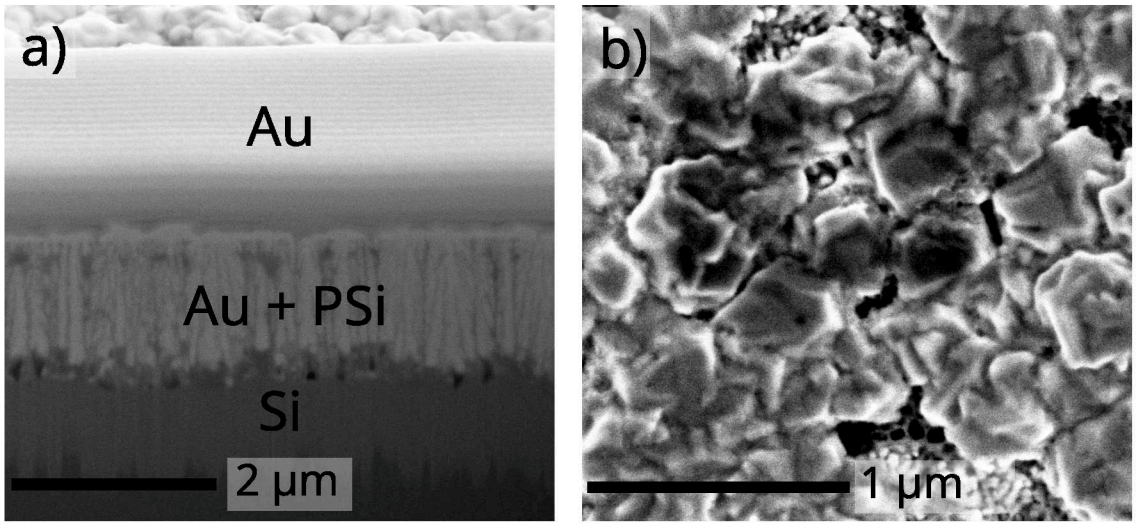

Figure C.1: Scanning electron microscopy n-doped PSi (dark) with gold (bright). a) crosssection of an Au filled PSi epilayer cut by focused ion beam (supported by Manuel Brinker). To protect the region of interest from milling a solid gold bar is deposited on the surface (Au). b) top view, showing gold crystals grown on the surface, but also some unfilled or incomplete filled pores.

D Polystyrene in Oxidic Scaffold Materials

D.1 Melt Infiltration

Melt infiltration of polymers in nanopores is subject of great interest for novel composite materials, molding of nanostructures and enhanced bonding. An example of the special properties of polymers is their tendency to have a faster spreading molecular layer at the pore walls, i.e. a precursor film, than the main liquid meniscus. This can be used for the formation of nanotubes.[14] Monitoring melt infiltration in nanoporous scaffold materials remains delicate, which was demonstrated for example by gravimetric measurements [140]. Direct observation of the imbibition length of polymer melts in individual nanopores is even more challenging. A strategy to solve this problem consists in freezing the melt after different imbibition times. Then, ex situ measuring methods with a resolution on the nanoscale can be applied to investigate the polymer penetration in the scaffold material. This technique is applied in a comparative study of scanning electron microscopy (SEM) and x-ray computed tomography (XCT) that inspired the investigation of polymeric liquids of this thesis and was supported by calculations that are described in the following.[15, 16]
In the study melt infiltration of polystyrene ($M_\mathrm{w} = 239\,\mathrm{kg/mol}$; $M_\mathrm{n} = 233\,\mathrm{kg/mol}$; PDI = 1.03) into self-ordered *anodized aluminium oxide* (AAO) and *controlled porous glass* (CPG) is investigated. AAO serves as a model material with cylindrical pores in a hexagonal arrangement, whereas CPG has a sponge-like pore structure. Both scaffold materials have an approximate mean pore diameter of 380 nm. Polystyrene (PS) is solid at room temperature with the given degree of polymerization. The viscosity of the melt is approximated from a reference PS ($M_\mathrm{w} = 123\,\mathrm{kg/mol}$) with a bulk viscosity $\mu_0 = 3.5 \cdot 10^4\,\mathrm{Pa\,s}$ at 443 K.[141] The value is corrected for the molecular weight by the power law $\mu_0 \propto \mathrm{M}^{3.4}$ suggested by *Berry* and *Fox* (Eq. D.1).[142] Subsequently, the viscosity is corrected by the *Williams-Landel-Ferry* (WLF) equation (Eq. D.2), with $\mathrm{C_1} = 17.44$ and $\mathrm{C_2} = 51.6\,\mathrm{K}$ for the applied temperature of 473 K.[143] For the glass temperature T_g a literature value of 373 K is assumed.[144] From an experimental point of view,

it is to note that the logarithmic dependence of the viscosity on the temperature requires a precise control of the applied heat.

$$\left(\frac{M_1}{M_2}\right)^{3.4} = \frac{\mu_{0,1}}{\mu_{0,2}} \tag{D.1}$$

$$\log\left(\frac{\mu_0}{\mu_{0,\mathrm{g}}}\right)^{3.4} = -\frac{\mathrm{C}_1\,(T - T_\mathrm{g})}{\mathrm{C}_2 + T - T_\mathrm{g}} \tag{D.2}$$

For melt infiltration the polymer is heated to 473 K under argon atmosphere for 10 min and then brought into contact with the porous scaffold material. The imbibition state is frozen by a bath in ice cold bidistilled water after different infiltration times. Fluid mensici front positions are investigated ex situ by SEM and XCT.

The strength of these ex situ techniques lies in their capability to determine the liquid front position of individual pores. For AAO the pore sizes are determined this way as well, in case of CPG mercury intrusion porosimetry is applied. The pores of an AAO membrane are not interconnected and of largely cylindrical shape. Therefore, the imbibition length, which is the average distance of menisci from the surface in contact with the bulk polymer melt, is modeled by a *Lucas-Washburn* like equation (Eq. D.3). As described in the theory subsection 2.3.1 a slip length b is introduced ($r_\mathrm{h} = r_0 + b$), fitting to the theory of *Yao* et al., to correct the relation of hydraulic radius r_h and the geometrical one r_0.[145] Fitting the average XCT imbibition length with Eq. D.3, given a surface tension of 29 mJ/m^2 [144] and a $\cos\theta \approx 1$ [144], a slip length of 40 nm is calculated.[15] Given the pore radius distribution from SEM and the slip length, Eq. D.3 can be applied to calculate the imbibition length of individual pore sizes with the frequency of occurrence in the pore size distribution. The substitutions necessary are $\langle L \rangle = L(t)_n$ and $r_0 = r_{0,n}$, where n is the number frequency of the pore radius distribution. Taking the standard deviation of the imbibition front distribution calculated this way in dependence of time is in excellent agreement with the ones measured (Fig. D.1).
Similarly, the average imbibition front position of PS can be calculated from the pore size distribution of CPG. Since for CPG the relative frequency of pore segments within a certain pore size range is obtained from mercury porosimetry and the pores follow a meandering path with a tortuosity τ_D of 3.6 [20], Eq. D.3 is modified accordingly (Eq. D.4). Fig. D.2 displays great agreement of the measured calculated mean imbibition front position. The Standard deviation as a measure of the imbibition front broadening is overestimated by the calculations though. This indicates that menisci in CPG do not move independently, as it is the case for AAO.[16]

$$\langle L(t)\rangle = \sqrt{\frac{r_{\mathrm{h}}^4 \sigma_{\mathrm{YL}} \cos\theta}{2\mu r_0^3}}\sqrt{t} \tag{D.3}$$

$$\langle L(t)\rangle = \sum_{\mathrm{g}=1}^{\mathrm{z}} (f_{\mathrm{g}} L_{\mathrm{g}}) = \sum_{\mathrm{g}=1}^{\mathrm{z}} \left(f_{\mathrm{g}} \sqrt{\frac{r_{\mathrm{h}}^4 \sigma_{\mathrm{YL}} \cos\theta}{2\mu r_0^3 \tau_{\mathrm{D}}}}\sqrt{t} \right) \tag{D.4}$$

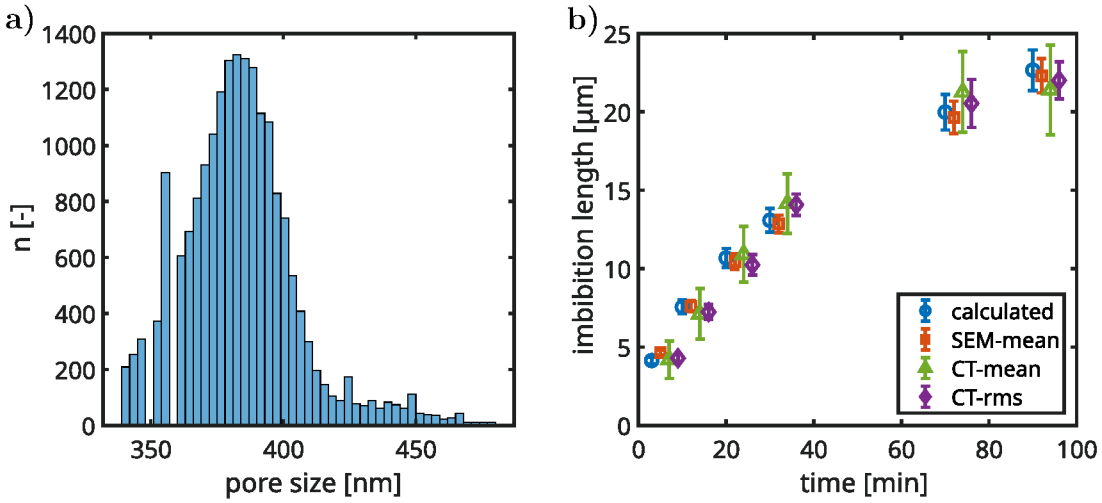

Figure D.1: a) Pore size distribution of AAO by SEM. b) Imbibition measurements and calculations. CT-mean and CT-rms are different methods for the evaluation of the XCT data set. The markers are shifted by 2 min in time to improve readability. (Reprinted with permission from [15]. Copyright 2021 American Chemical Society.)

D.2 Shaping AAO Membranes with Polystyrene

In the previous section melt infiltration in AAO is investigated ex situ. There, the porous layer is attached to the bulk material. For in situ measurements of the dynamics, freestanding AAO membranes are prepared to conduct thin film interference measurements. The thicknesses of these membranes are in the order of 20 µm. A smaller pore size and pitch distance to have the material act as an effective medium for electromagnetic waves has to be selected for this kind of measurement as well.

During this investigation it is noticed, that AAO membranes that are picked up by tweezers, when still at 473 K, deform during cooling. The membrane covered and infiltrated by the polymer stays in its final frozen shape at room temperature. This interesting behavior is further investigated for differently prepared AAO samples. The interference measurements are not pursued further, since interference fringes

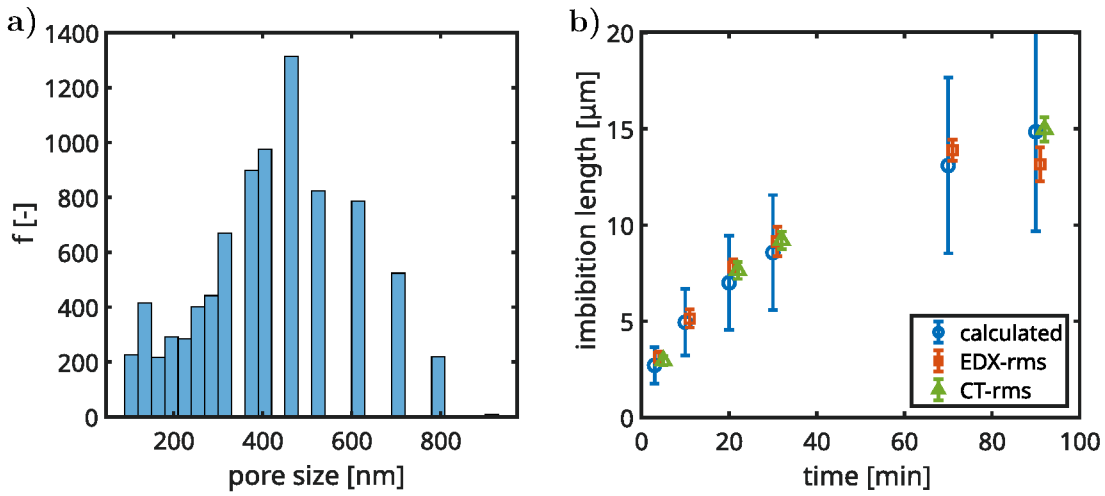

Figure D.2: a) Pore size distribution of CPG by mercury intrusion. b) imbibition measurements and calculations. CT-rms is a method for the evaluation of the XCT data set. The markers are shifted by 1 min in time to improve readability.(Reprinted with permission from [16]. Copyright 2022 American Chemical Society.)

are often lost during measurements. It is possible, that deformations during the wetting are the reason for these problems. Notably, imbibition experiments with oligostyrenes liquid at room temperature, were successfully investigated by laser interferometry.[146]

The deformation of AAO-PS bilayers is investigated using PS (from Polymer Standard Services) with a molecular mass of 21 kg/mol with a polydispersity index close to one. Strong folding is observed for membranes with a high entrance radius and a thin layer of lower pore size at the bottom with regard to the anodization process. An example is shown in Fig. D.3. Samples are provided by *A. Kityk* from the Czestochowa Institute of Technology. The AAO membrane is cut into a rectangular shape by a laser cutter. PS is dried by heating to 353 K over 2 h under argon atmosphere. The melt infiltration is conducted at 523 K likewise under argon atmosphere. Once the bilayer is lifted of by tweezers, deformation is initiated by environmental cooling.
The shaping of the bilayers is discovered to be reversible, by heating on a substrate again. Figure D.4 displays a sequence, where the AAO is covered from both sides with polymer. After infiltration it is detached from the polymer covered aluminum substrate and starts to bend. The sample is then turned over by 180° and placed on the hot plate again. In few seconds the flat shape is recovered. Picking the bilayer up again results in bending in the opposite direction. The shaping process is repeatable several times without failure, if the sample is manipulated carefully on the substrate. The liquid meniscus between substrate and bilayer is strong enough to break the sample, therefore sliding over the edge is a successful strategy to lift of the bilayer. In contact with the polymer in the melted state, the

bilayer can be deformed manually similar to a *Bézier* curve. Complete recovery of the AAO's initial flat state is also achieved by dissolution of the polymer by toluene.

It can be concluded that the deformations of the bilayers during cooling are elastic, even given the extreme curvatures. Thereby the polymer melt seems to distribute applied forces, when in the melted state and applies a tension when it shrinks with decreasing temperature. Strong bending without failure is known for ceramic thin sheets [147], but the combination with nanoporosity opens up several new material design possibilities. It is also known that the bonding of polymer and ceramic is enhanced because of the large contact area and the bending stiffness can be controlled by the porosity. Other parameters like the influence of pore radius gradients, which could induce directional bending by a pore load gradient from the deforming PS, are still to be investigated. Similar self folding designs are already used in macroscopic components of medical soft robotic devices.[148, 149] Another aspect is going to be investigated in the DFG-project *Hyperuniform anodic aluminium oxide (hAAO): a 2D metamaterial with improved mechanical properties for hard-soft bilayer composite actuators.* There, the pore assembly of AAO is manipulated to achieve hyperuniformity, a state between ordered and disordered structure. *Torquato* et al. proposed improved mechanical behaviour for such assemblies.[150]

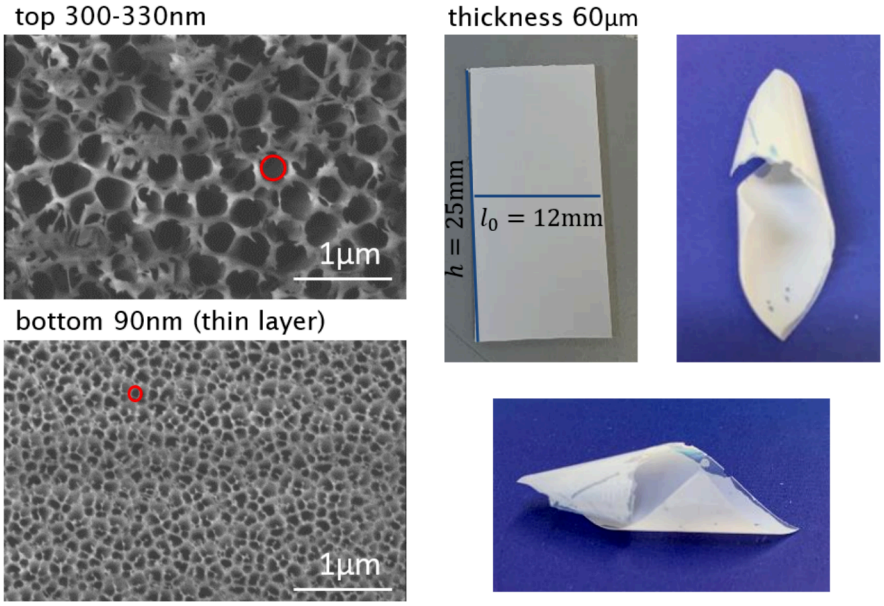

Figure D.3: SEM of an AAO membrane anodized in two steps with phosphoric acid for 120 min (provided by A. Kityk). The flat sheet in the center is the macroscopic sample before polymer infiltration. After melt infiltration and subsequent cooling, the bilayer stayed in a rolled up state.

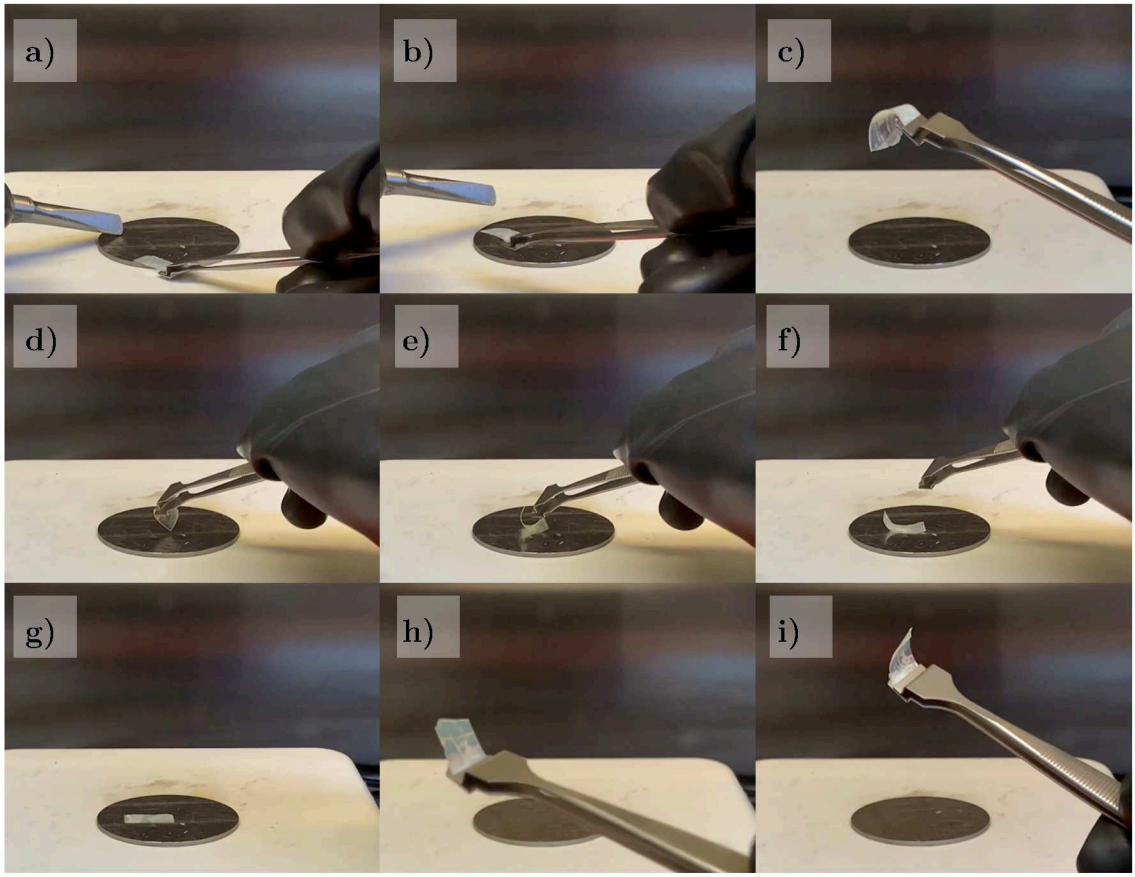

Figure D.4: Reversible shaping of AAO-PS bilayers: a) lift of by sliding over the edge, b) start of cooling, c) cooled state, d) sample is turned upsite down, e-f) reshaping by placing on hot substrate again, g) recovered flat state, h) sample is lifted of again, i) bend state after cooling down.